Doctoral theses at NTNU, 2016:326

Nils Håvard Giskeødegård

Barrier Oxide Growth and Dissolution on Aluminium in Aqueous Media

NTNU
Norwegian University of
Science and Technology

Doctoral thesis

Nils Håvard Giskeødegård

ISBN 978-82-326-1990-0 (printed ver.)
ISBN 978-82-326-1991-7 (electronic ver.)
ISSN 1503-8181

Doctoral theses at NTNU, 2016:326

NTNU
Norwegian University of
Science and Technology

NTNU
Norges teknisk-naturvitenskapelige universitet
Thesis for the Degree of
Philosophiae Doctor
Faculty of Natural Sciences and Technology
Department of Materials Science and
Engineering

NTNU

Nils Håvard Giskeødegård

Barrier Oxide Growth and Dissolution on Aluminium in Aqueous Media

Thesis for the Degree of Philosophiae Doctor

Trondheim, November 2016

Norwegian University of Science and Technology
Faculty of Natural Sciences and Technology
Department of Materials Science and Engineering

NTNU
Norwegian University of
Science and Technology

NTNU
Norwegian University of Science and Technology

Thesis for the Degree of Philosophiae Doctor

Faculty of Natural Sciences and Technology
Department of Materials Science and Engineering

ISBN 978-82-326-1990-0 (printed ver.)
ISBN 978-82-326-1991-7 (electronic ver.)
ISSN 1503-8181

Doctoral theses at NTNU, 2016:326

Printed by NTNU Grafisk senter

Preface

The work presented in this thesis was carried out at the Department of Material Science and Engineering, Norwegian University of Science and Technology. This work was fully financed by the Norwegian Research Council.

I am very thankful for the support, assistance, advice and excellent supervising provided by my supervisor Professor Kemal Nisancioglu, during the extended period of this work. I will also thank my co-supervisor Professor Ola Hunderi, who left this world all too early in 2016, for many fruitful discussions and good advices. May he rest in peace.

I am grateful for all discussions and talks with my office companions Magnus Hurlen Larsen and Koksal Kurt.

Special thanks to Yingda Yu for his support in the TEM laboratory. Furthermore, I thank all my colleagues and friends at the department, during my Phd period. Especially Kjell Røkke and Martha Bjerknes are acknowledged for great support.

I will also like to thank my current employer, Norsk Hydro, for employing me before I received my Phd and thereby allowing me to finalize this very interesting work.

I thank my wife, Tessie and my two children, Nissa Marie and Natalia Sofia for being there for me.

Finally, I will thank God, for providing us with this wonderful nature that we can investigate, and for always being there for me.

Summary

The oxide formed during anodization of aluminium has been a subject of attention since the beginning of the 20th century, due to its protective properties. The oxide consists of two layers, a dense layer adjacent to the metal (barrier oxide) and a hydrated and porous outer layer. Most of the available studies deal with oxide growth in oxygen containing gaseous environment and high voltage anodizing in aqueous solutions. The subjects of interest in the present study are the growth kinetics, and the physical and electrochemical properties at macroscopic scale of the barrier oxide formed at low temperature and potential in aqueous environment. The motivation for the present work is to obtain comprehensive information about barrier oxide growth and dissolution rates, as well as barrier oxide properties, on aluminium by using three experimental approaches, *viz.*, chronoamperometry, electrochemical impedance spectroscopy (EIS) and visual spectroscopic ellipsometry (VISSE), simultaneously and investigate to what extent the results from each can be evaluated in a complementary manner. In addition, VISSE should be able to provide useful information about the growth and dissolution of the hydrated layer and its properties. Another incentive for the work is to develop a quantitative method to investigate the effect of trace elements in aluminium, especially the low melting point elements such as Pb, on the electrochemical and corrosion properties (passivity) of the oxide.

The materials investigated were pure Al and Al containing 20 ppm of Pb, the latter representing an impure example. The test solution consisted of mixtures of glacial acetic acid and sodium acetate in the pH range 5.6-6.3. It was exposed to an air conditioned laboratory, maintained at 22°C. The experimental method involved stepwise change of the applied potential and monitoring the ensuing time-dependent change by current measurement and VISSE at each step. EIS was used to calibrate the steady-state barrier-film thickness at the end of each step. The dependence of steady state barrier-oxide thickness on the applied potential, as obtained by EIS, was 1.1 nm/V, in agreement with the well-accepted data for the experimental conditions specified above. In addition, EIS was used to evaluate the steady-state resistance of the barrier oxide.

For barrier-film growth, VISSE and chronoamperometry gave the same growth rates under identical experimental conditions, as expected. Thus, the use of the two methods simultaneously provided an effective control of the reliability of the measured data. In this manner, the drawbacks of the methodology were identified, such as the slowness of the multi-wavelength ellipsometric technique relative to the fast rate of barrier-layer growth, which was not a problem to detect with fast current measurement.

For tracking barrier-film dissolution, ellipsometry proved to be effective and reliable method in this case because the mass transfer controlled dissolution occurred at a significantly slower rate than growth, verifying earlier work that it is a chemical process. However, chronoamperometry was not applicable because of the chemical nature of the process, discussed further below. In this respect, the two methods were quite supplementary in producing the desired data.

Long period (days) of potentiostatic polarisation was necessary to obtain a steady state hydrated oxide thickness. Here the obtained barrier oxide thickness by EIS was used as a constant input into the VISSE multilayer model. The actual thickness of the hydrated oxide, dependent on the morphology and hydration of the hydrated oxide, was not reversible or reproducible because of continuous hydration as a function of the immersion time. However, the steady state effective mass thickness of hydrated oxide was shown to be reversibly determined by the applied potential.

Ex situ methods for determination of the thickness of the barrier layer, such as TEM analysis of film cross sections, appeared to give erroneous results during growth of thin films, for which an

in situ approach is necessary because exposure of samples to ambient air by further preparation and transfer, *e.g.*, to a microscope, affects film thickness. *Ex situ* methods may be applicable for determining the thickness of thick anodized films, which are more stable in transfer.

The results verified unambiguously that the growth of barrier oxide on aluminium in aqueous solution is consistent with Cabrera-Mott law of growth kinetics. This result thus verifies the earlier literature that, the law originally developed for oxide growth on metals in oxygen containing gaseous environments, is also applicable to barrier oxide growth in aqueous solution. The present work shows the applicability of the growth law also for small applied potentials giving growth of oxide films as thin as a few monolayers. The required high field for maintaining films of such thickness is expected to exist at such low potentials due to the small thickness of the film. The steady-state thickness can accurately be controlled by the applied potential at 1.2 nm/V, a value which was established earlier in anodization studies, relying mostly on *ex situ* thickness measurements. The Cabrera-Mott parameters δ_1, u and W, could readily be obtained and the variation of these parameters, especially the activation energy W, appeared to be of the correct order of magnitude and vary in an intuitively acceptable manner by variation of an experimental parameter, such as the applied potential.

Analysis of dissolution rate by ellipsometry verified mass-transfer controlled barrier oxide dissolution on pure Al according to Fick's second law, suggesting that the rate of barrier film dissolution is largely a chemical process. Applied potential determines the oxide solubility. Thus, the measured film-dissolution data allows the measurement of the film solubility if the diffusion coefficient of Al^{3+} in the test solution is known. This may be a useful parameter in investigating the passivity of the oxide as a function of environmental factors under irreversible conditions.

Segregation of trace element Pb to the oxide-metal interface and into the oxide film by heat treatment reduces the passive properties of the barrier layer, quantified in terms of increased capacitance, reduced film thickness, reduced polarisation resistance and increased leakage (passive) current. The relative thickness change, with respect to the applied potential, remains at the same value (1.2 nm/V) as that for pure Al. This may indicate that the oxide formed is still pure Al oxide with the same composition and structure as on pure Al at molecular scale, while the apparent conductivity of the contaminated oxide is reduced. The transient results indicate a significant decrease in the Cabrera-Mott parameters δ_1 and W for the AlPb alloy relative to pure aluminium. These parameters further change more moderately, but in the same direction with increasing annealing temperature and time. W is about 50% smaller for the AlPb alloys, decreasing slightly with increasing heat treatment temperature and time. These results can be regarded as additional evidence to earlier studies that the passivity of the barrier film decreases as a result of increasing contamination with Pb with increasing heat-treatment temperature and time. The behaviour of the 600°C-annealed AlPb sample, characterized by excessive Pb segregation to the surface, was anomalous in relation to the other alloys. An improved impedance model that, takes into account dispersed Pb particles may be necessary. A more direct method for thickness monitoring could also be beneficial. Unfortunately, reduced specularity of AlPb sample surfaces prevented the use of ellipsometry.

Contents

1 Introduction

1.1 Background

The oxide formed during anodization of aluminium has been a subject of attention since the beginning of the 20th century, due to its protective properties [1]. The oxide consists of two layers, a dense layer adjacent to the metal (barrier oxide) and a hydrated and porous outer layer [2]. It is formed by the reaction between Al^{3+} and O^{2-} ions either at the metal-oxide interface or at the oxide-solution interface. This model is known as the high field model, which is based on the work by Güntherschulze and Betz [3], Verwey [4] and Mott and Cabrera [5]. The high field across barrier oxide is formed by charge separation between the solution-barrier oxide interface and barrier oxide-metal interface, resulting from adsorption of O^{2-} ions at the solution-oxide interface [3]. The field is responsible for the transport of charged species through the oxide by ion hopping, tunnelling or transport of vacancies during growth and maintenance at steady state.

Several *in situ* methods, based on electrochemical polarization [3], electrochemical impedance spectroscopy (EIS) [6,7] and visual spectroscopic ellipsometry (VISSE) [8,9] have been used for studying the properties of thin aluminium oxide films in solution. The applicability of EIS requires steady state conditions. The electrochemical methods are limited to study of the barrier oxide layer alone since this layer determines the electrochemical properties. These methods also depend on successful separation of the current used for film growth from a measured net current, which may include a leakage (passive) current and partial currents due to reduction processes simultaneously occurring on the surface. Ideally, VISSE can provide steady state and transient data simultaneously for oxide thickness and refractive index. It can be used to track the growth and dissolution of both the hydrated and barrier oxide layers, with certain limitations in distinguishing between these two for very thin films [9]. The data acquisition time may become a limitation for monitoring very fast oxide growth [10]. Specularity of the analysed surface is another possible limitation. EIS and VISSE require physical and mathematical models by which the experimental results can be analysed.

In view of the foregoing limitations of the analytical methods available, the motivation for the present work is to use the three experimental approaches (chronoamperometry, EIS and VISSE) simultaneously and investigate to what extent the results from each can be evaluated in a complementary manner to obtain comprehensive information about barrier oxide growth and dissolution rates, as well as barrier oxide properties, on aluminium. In addition, VISSE should be able to provide useful information about the growth and dissolution of the hydrated layer and its properties.

Another incentive for the work is to develop an analytical method to investigate the effect of trace elements in aluminium, especially the low melting point elements such as Pb and Ga, on the electrochemical and corrosion properties of the commercial alloys. Pb and Ga are present in nearly all commercial alloys because they are commonly present in the bauxite ore. Pb has been shown to segregate in the form of nano-size particles in the oxide and as a continuous nanofilm along the aluminium-oxide interface by heat treatment, even though its concentration in the bulk metal may be as low as a few wt ppm [11,12]. The segregated Pb film causes significant anodic activation of the surface in the presence of chloride in an aqueous environment [13]. It is of interest to supplement the *ex situ* microscopic and spectroscopic techniques in use today, to study the effect of trace elements in aluminium alloys in general, with *in situ* optical and advanced electro-analytical

methods to be able to distinguish between the oxide properties *per se*, interfacial segregation effects, adsorption on the oxide surface and the role of aggressive ions (Cl^-) in the environment for a better understanding of the governing mechanisms of surface modification.

1.2 Objectives

This work will investigate the use of simultaneous chronoamperometry, EIS and VISSE in acetate-buffered, chloride-free aqueous solution, to obtain an improved understanding of

- barrier oxide growth and dissolution kinetics,
- growth laws governing these, in particular the applicability of Cabrera-Mott inverse square logarithmic growth law
- barrier oxide properties, such as steady state thickness, leakage current and barrier resistance as a function of applied potential and potential step size,
- the formation of the hydrated oxide layer (density and thickness) and its dependence of applied potential and time,
- the difference between *in situ* and *ex situ* measurement of barrier oxide and hydrated oxide steady state thicknesses by comparing the *in situ* results to TEM measurements, on pure aluminium. Applicability of the developed methodology to impure aluminium will further be investigated by studying
- the effect of the trace element Pb on the properties of the oxide and oxide-metal interface, as a function of heat treatment time and temperature.

1.3 Structure of the thesis

The next chapter (Chapter 2) is a literature review on oxide growth and dissolution on pure aluminium in aqueous solutions. The review includes certain issues on the growth kinetics in air with significance to growth in aqueous solution. Since the study on the effect of trace elements is limited to Pb, the past work on Pb segregation and the corresponding anodic activation are summarized. Chapter 3 treats the proposed methodology involving simultaneous use of chronoamperometry, EIS and VISSE to investigate growth and dissolution of the barrier and hydrated oxide layers. Chapter 4 describes the application and validation of the method for barrier layer growth and dissolution on pure Al in slightly acidic acetic acid-sodium acetate buffer solution. Chapter 5 investigates to what extent the methodology is applicable to aluminium containing 20 wt ppm Pb, where Pb was segregated to the surface in a controlled manner by heat treatment at different temperatures and durations.

1.4 References

[1] Bengough, G. and Stuart, J. *Brit. Patent* **223994** (1923).

[2] Thompson, G. E. *Thin Solid Films* **297**, 192 (1997).

[3] Guntherschulze, A. and Betz, H. *Z. Phys.* **92**, 367 (1934).

[4] Verwey, E. J. W. *Physica(A)* **2**, 1059 (1935).

[5] Cabrera, N. and Mott, N. F. *Rep. Prog. Phys.* **12**, 163 (1948-1949).

[6] Gudic, S., Radosevic, J., Krpan-Lisica, D., and Kliskic, M. *Electrochim. Acta* **46**(16), 2515-2526 (2001).

[7] Hasenay, D. and Seruga, M. *J. Appl. Electrochem.* **37**(9), 1001-1008 (2007).

[8] Greef, B. and Norman, C. *J. Electrochem. Soc.* **132**, 2362 (1985).

[9] Gils, S. V., Melendres, C., Terryn, H., and Stijns, E. *Thin Solid Films* **455-456**, 742-746 (2004).

[10] Greef, R. *Thin Solid Films* **233**, 32-39 (1993).

[11] Sævik, Ø., Yu, Y., Nordlien, J., and Nisancioglu, K. *J. Electrochem. Soc.* **152**, B334-B341 (2005).

[12] Sævik, Ø., Yu, Y., Nordlien, J., and Nisancioglu, K. *J. Electrochem. Soc.* **152**, B327-B333 (2005).

[13] Walmsley, J. C., Sævik, Ø., Graver, B., Mathiesen, R. H., and Nisancioglu, K. *J. Electrochem. Soc.* **154**, C28-C35 (2007).

2 Literature review

The objective of this chapter is to review the literature on growth and dissolution kinetics of oxide on aluminium in aqueous solution at low temperatures and low applied potentials. Most of the available studies deal with oxide growth in oxygen containing gaseous environment [1,2] and high voltage anodizing in aqueous solutions [3,4]. The subjects of interest in the present study are the growth kinetics, and the physical and electrochemical properties at macroscopic scale of the barrier oxide formed at low temperature and potential in aqueous environment. However, earlier investigations of oxide growth in air still provide the basis for understanding oxide growth in aqueous solutions [5,6]. Similarly, the high voltage anodizing may become useful in understanding low voltage anodization, especially the initial stage of barrier layer growth. The chapter includes a short review of the known effect of common activating type of trace elements present in most Al alloys, in particular ppm levels of Pb, which become incorporated in the oxide during growth. The available information is critically analysed for justifying the objectives of the present thesis.

2.1 Oxidation and ionic transport

In an aqueous environment, aluminium is oxidised at the metal-oxide interface according to reaction

$$Al \rightarrow Al^{3+} + 3e^{-} \quad \textbf{(2-1)}$$

Adsorbed oxygen ions are formed by dissociation of water at the barrier layer surface [7],

$$H_2O + 2e^{-} \rightarrow 2H + O^{2-}_{ads} \quad \textbf{(2-2)}$$

The electrons are considered to be transferred by quantum-mechanical tunnelling through the thin oxide, as shown in Fig. 2.1. The adsorbed oxide ions are incorporated into the barrier layer according to

$$O^{2-}_{ads} \rightarrow O^{2-} \quad \textbf{(2-3)}$$

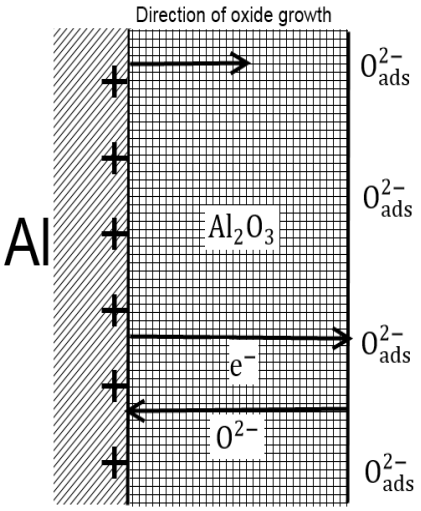

Figure 2.1 Transport of charged species during barrier oxide growth.

Charge separation resulting between the positively charged metal-oxide interface and negatively charged oxide surface gives rise to an electric field, which becomes the driving force for migration of Al^{3+} and O^{2-} in opposite directions, for natural oxide growth in air or in aqueous solution. This is further assisted by the applied potential during anodisation in aqueous solutions [4,5,7,8]. The ions are transported without reacting with each other in the bulk of the oxide film [4]. The oxide is formed by the reaction between aluminium and the oxide ions at the metal-oxide and/or oxide-solution interfaces according to

$$2Al^{3+} + 3O^{2-} \rightarrow Al_2O_3 \qquad \textbf{(2-4)}$$

Transport numbers of the mobile species were measured by use of marker and tracer techniques, as reviewed in [9]. For barrier oxide growth on aluminium, the mobility of both aluminium and oxygen ions were shown by XPS (X-ray Photoelectron Spectroscopy) and XAS (X-ray Absorption Spectroscopy) measurements of marker position in the oxide during anodization in borate and phosphate solutions [4]. The cation transport number was reported to increase from 0.4 to 0.49 by an increase in applied current density from 6 to 50 mA/cm^2 [10]. These results pertain to high voltage anodization, but they are assumed to apply also to low voltage oxidation in aqueous solution.

It appears from the foregoing review that about 50% of the oxide is formed from aluminium ion egress and 50% from oxygen ion ingress in near neutral solutions [10]. In acid solutions, the growth of the barrier oxide occurs mainly at the metal/oxide interface [8]. A certain fraction of the Al^{3+} ions formed may not take part in the formation of the barrier oxide and migrate through the oxide into the solution [4]. However, the transport of the Al^{3+} ions through the oxide, which determines the measured passive current, contributes to the formation of the outer porous oxide [11].

Several mechanisms for ion transport have been suggested such as the ion-hopping model [5,7]. Investigation of the atomistic nature of charge transport in the bulk oxide is outside the scope of this thesis. The macroscopic growth and dissolution kinetics are of prime interest for direct experimental measurement and data correlation. In fact, a common macroscopic growth law appears to be applicable to the atomistic theories briefly mentioned above, as will be shown in the next

section. The dissolution kinetics of the barrier oxide on aluminium has been suggested to be based on field assisted dissolution without conclusive evidence [12,13].

2.2 Macroscopic theory of barrier oxide growth

The available experimental data for barrier oxide growth on aluminium under an applied current or potential in neutral aqueous solution suggest that the growth rate can be expressed by the phenomenological growth law [2,7,14], which can be written in the form

$$i = \alpha \exp\left(\beta \frac{U}{\delta}\right) \tag{2-5}$$

where i is the current density, U is the potential across the barrier oxide, α is the mobility of the transported ion at zero field strength, $\beta = \frac{\varsigma zFa}{RT}$, z is the valence, F is Faraday's constant, ς is a parameter between 0 and 1 related to the location of the activation barrier for migration of the transported ion from one oxide position x to another at $x + a$ (the "jump distance"), T is the temperature in °K, and R is the ideal gas constant. Eq. (2-5) can be derived by first considering two adjacent planes placed at an infinitesimal spacing a in the oxide parallel to the metal surface at x and $x+a$, containing the number of mobile species n_x and n_{x+a}, respectively [9]. The rate of charge transport between the two surfaces can be expressed as

$$\frac{dn}{dt} = n_x p_f - n_{x+a} p_b \tag{2-6}$$

where p_f and p_b are the probabilities of charge transfer in the positive and negative x-direction, respectively. In the absence of an electric field, the movement of species is purely statistical, and the probability, p, of ion transport in both directions is given by [9]

$$\rho = \nu \exp(-W / RT) \tag{2-7}$$

where ν is the attempt frequency, W is the activation energy for transfer, T is the temperature and R is the gas constant. However, in the presence of an electric field, the activation energy in the direction of the field is decreased, which causes the transport of positive aluminium ions from the metal to the oxide-solution interface and negative oxygen ions in the opposite direction to be preferred [9]. The effective activation energy is lowered by $-\alpha azFE$ when the field is in the direction that supports charge transfer, while it is increased by $(1-\alpha)azFE$ in the opposite direction. Again assuming a constant concentration gradient between the metal surface at x and $x+a$, the number of mobile species at $x+a$ is given by

$$n_{x+a} = n_x + \frac{\mathrm{d}n}{\mathrm{d}t} \tag{2-8}$$

Substitution of Eq. (2-7) and Eq. (2-8) into Eq. (2-6) gives

$$\frac{dn}{dt} = a\ \exp\left(-\frac{W}{RT}\right)\left[n_x \exp\left(\frac{\alpha azFE}{RT}\right)-\left(n_x+\frac{dn}{dx}\ a\right)\ \exp\left(-\frac{(1-\alpha)azFE}{RT}\right)\right] \quad \textbf{(2-9)}$$

By combining with Faraday's law and by assuming that the transfer of charge opposed to the electric field is negligible (the second term on the right), it is seen that this equation becomes of the same form as Eq. (2-12) [9].

Assuming that oxide growth is the only current consuming process and that the dissolution rate is much smaller than the growth rate, a combination of Faraday's law and Eq. (2-5) gives [15]

$$i=\frac{\mathrm{d}\delta}{\mathrm{d}t}\frac{zF\rho}{M}=\alpha\exp\left(\frac{U}{\delta}\right) \quad \textbf{(2-10)}$$

where z is the valence, F is Faraday's constant, and ρ is the oxide density. Defining $\alpha^* = \alpha\frac{M}{zF\rho}$ gives

$$\frac{\mathrm{d}\delta}{\mathrm{d}t}=\alpha^*\exp\left(\beta\frac{U}{\delta}\right) \quad \textbf{(2-11)}$$

The growth law for thin films, derived by Cabrera and Mott [5], is expressed as

$$\frac{\mathrm{d}\delta}{\mathrm{d}t}=2N\Omega\nu\exp\left(-\frac{W}{kT}\right)\sinh\left(\beta\frac{qaE}{2kT}\right) \quad \textbf{(2-12)}$$

where k is the Boltzmann's constant, W is the activation energy for transfer, N is the surface density of surface sites, Ω is the volume of surface sites, υ is the jump frequency, $E=\frac{U}{\delta}$ is the electric field due to the potential difference U across the barrier oxide and q is the ion charge density. By substituting $\delta_1=\frac{qaU}{2kT}$ and $u=N\Omega\upsilon\exp\left(-\frac{W}{kT}\right)$ this relation becomes, for thin oxides, of the same form as Eq. (2-11) [5]

$$\frac{\mathrm{d}\delta}{\mathrm{d}t}=2u\sinh\left(\frac{\delta_1}{\delta}\right)\approx u\exp\left(\frac{\delta_1}{\delta}\right) \quad \textbf{(2-13)}$$

Cabrera and Mott assumed that oxide growth in gas atmosphere occurs by cation migration alone, and that the voltage drop across the oxide film is independent of the oxide thickness. The voltage drop between the metal and oxide surface is considered to be rate determining [5]. An initial transfer occurs due to thermionic emission or tunnelling of electrons from the metal to the lower energy electron levels at the oxide surface. The electrons reduce the oxygen in air to produce the adsorbed oxygen ions discussed above, creating separation of charge between the oxide and metal surfaces, which gives rise to the high electric field responsible for Al^{3+} migration through the thin aluminium oxide. Cabrera and Mott calculated the magnitude to be about 10^7 V/cm for 50 Å thick oxide on a metal [5]. For potentiostatic polarisation, the potential difference is instead given by the applied potential [5].The electrons will continue to flow until the energy level of the trapped electrons reaches the Fermi level of the metal as illustrated in Fig. 2.2. The reaction between the Al^{3+} and oxygen ions at the film-gas interface results in oxide growth [16]. The growth rate, which

is high at the outset, will decrease with increase in film thickness, which reduces the electric field across the film.

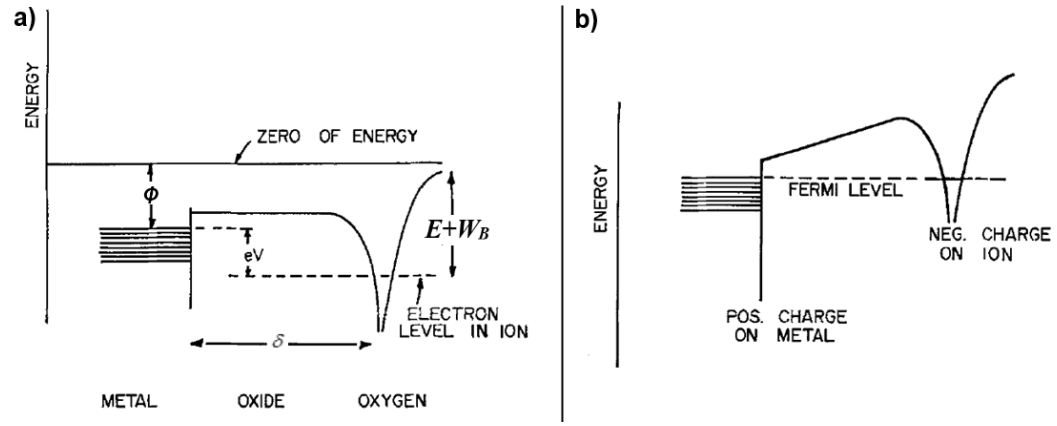

Figure 2.2 Electronic energy levels in the metal, oxide and adsorbed oxygen. In a: before electrons have passed. In b: after equilibrium is reached [17] (With permission of Springer). Φ is the work function of the metal, E is the electron affinity, $E+W_B$ is the energy due to the image force of an electron distant r from an oxide, and δ is the thickness of the oxide

Due to later evidence of anion migration [18], in addition to cation migration, the constant voltage drop concept was abandoned in favour of a constant electric field assumption. This gave a thickness dependent activation energy, resulting in a direct logarithmic growth rate [17,19]. However, for the special case of constant potential drop the Cabrera-Mott kinetics is still valid [17].

For oxide growth in aqueous solutions, the potential drop across the oxide is the driving force for ion migration [5]. Oxide growth was shown to occur at both metal-oxide interface and oxide-solution interface, attributed to anion and cation migration respectively [4]. For the special case of constant potential drop, as in potentiostatic anodization, Fromhold's extensive theoretical examination of oxide growth results in a growth rate equation of the same form as Eq. (2-13).

Eq. (2-11) can be integrated and rewritten in the form [15]

$$t = \frac{1}{\alpha^*}\int_0^{\delta} \exp\left(\beta\frac{-U}{\delta}\right)d\delta \qquad \textbf{(2-14)}$$

and solved for δ by performing the integration. For thin enough oxide films, this integration is also valid for Eq. (2-13). Depending on the assumptions made for the integration, various relationships for growth kinetics results can be obtained.

By integration of Eq. (2-14) by parts, neglecting higher order terms of $\frac{\delta_1}{\delta}$ and by assuming a limiting thickness, δ_L, defined as the thickness at which the growth rate is less than one layer of atoms per 10^5 seconds, one obtains the result [5]

$$\left(\frac{\delta_1}{\delta}\right) = \ln\left(\frac{\delta_1 u t}{\delta_L^2}\right) \qquad \textbf{(2-15)}$$

where $\delta_1 = \beta U$ and $u = \alpha^*$.

A more rigorous integration of Eq. (2-14) for thin oxides, without assuming $\sinh\left(\frac{\delta_l}{\delta}\right) = \frac{1}{2}\exp\left(\frac{\delta_l}{\delta}\right)$, results in the following relation between thickness and time [21]

$$\left(\frac{\delta_l}{\delta}\right) = \ln\left(\frac{t+\tau}{\delta^2}\right) - \ln(\delta_l u) \qquad \textbf{(2-16)}$$

where τ is a constant that can be neglected if it is small compared to *t*. A simple test to check if τ is negligible is to first fit the results to Eq. (2-14) assuming $\tau = 0$ and then calculate the maximum of τ by the following inequality

$$\tau \le \left(\frac{\delta_0^2}{u\delta_l}\right)\exp\left(\frac{-\delta_l}{\delta_0}\right) \qquad \textbf{(2-17)}$$

where δ_0 is the initial oxide thickness at t = 0 [21]. If τ is much smaller than the experimental time-step, then it can be neglected. The derivation for Eq. (2-14) is valid only when δ is considerably smaller than δ_l, that is for small thicknesses. Eq. (2-16) is known as the Cabrera-Mott inverse square logarithmic growth law. If the measured film growth with respect to time yields a straight-line plot of $\frac{1}{\delta}$ vs. $\ln\left[\frac{t}{\delta^2}\right]$, then the growth kinetics is consistent with the Cabrera-Mott law (Eq. (2-12)). For thick oxides Eq. (2-16) yields a parabolic growth law [5], which is not relevant for this work, as only thin oxides are under consideration.

For anodic oxidation in aqueous solutions, the growth law represented by Eq. (2-16) is suggested to be still applicable [5]. The electric fields obtained during anodization [2,22] are similar to the field strengths calculated by Cabrera-Mott for oxide growth in air [5].

In aqueous solution, a two-layered oxide is formed on aluminium. Closest to the aluminium substrate is the dense barrier layer, which forms by oxidation of aluminium. The porous outer layer is formed at low applied voltage by dissolution and hydration of the barrier layer and precipitation of aluminium ions, which migrate through the barrier layer [4]. This review focuses on the growth and properties of the barrier layer, which controls the electrochemical and corrosion properties of aluminium, especially passivity.

2.3 Experimental studies of film growth in aqueous solution

Early experimental studies of film-growth kinetics on metals in aqueous solutions were based on indirect electrochemical measurements, mainly chrono-potentiometry or -amperometry, leading to the experimental observation of Eq. (2-5) by Güntherschulze and Betz [2], which was later supported by other workers [7,14,22,23]. Güntherschulze and Betz anodised Al and Ta up to 100 V at constant current in borax solutions. The anodization was interrupted at a pre-determined voltage and the oxide thickness was estimated by capacitance measurements. The measured electric field was in the range from 10^6 to 10^7 V/cm. The high electric field strength was considered the reason for oxide growth by charge transport through the oxide. In subsequent studies by use of cyclic voltammetry, chronopotentiometry and electrochemical impedance spectroscopy (EIS) techniques, the validity of Eq. (2-5) for oxide growth on pure Al and Al-Sn alloys in buffered borate solution (pH 7.8) was confirmed [22]. The parameters α and β in Eq. (2-5) were further estimated to be 4.88 x10^6 A/cm^2 and 1.44x10^6 cm/V respectively. Again, a high field strength of the order of 10^6 V/cm was obtained. The current efficiency for pure Al increased from 73% to 76% by increase

of the applied current from 20 to 100 μA/cm^2 [22]. Alloying Al with 0.4% Sn increased the current efficiency for film formation from 73% to 87%.

By EIS measurements in 0.05 m citric acid at pH 6, and subsequent fitting of the data to a simple equivalent circuit, consisting of oxide resistance in parallel with capacitance [23], formation of 1-2 nm thick oxide films with high resistivity was reported. The thickness to voltage ratio was reported to be 0.65 nm/V, somewhat lower than the well-established 1.2 nm/V, discussed in Section 2.5.

More recently, ellipsometry has been used as a more direct approach for *in situ* measurement of the barrier oxide thickness. However, due to a rather fast growth rate, ellipsometry is either limited to fast tracking of a single oxide layer [24] or slower spectroscopic tracking of two adjacent layers with reduced measurement frequency [25]. Gils et al. [25] tracked both the barrier oxide and hydrated oxide formed on pure Al in 0.1 M HCl at pH 1.2 at a measurement frequency of about 4 minutes. Growth kinetics could not be measured due to lack of either accuracy [24] or time resolution [25]. Oxide growth of iron, in response to a potentiodynamic scan rate of 20 mV/min, was possible to track with sufficient accuracy and time resolution in 0.15 N H_3BO_3 and 0.15 N $Na_2B_4O_7$ solution, due to a considerable lower growth rate compared to oxide growth rate on Al [26]. The results showed that the growth kinetics was equally well described by logarithmic and inverse logarithmic growth rate kinetics.

Other possible experimental techniques for kinetics evaluation include growing thick enough oxide film that does not change considerably after being exposed to air and then measure the obtained thickness by microscopy after the samples are removed from the solution. Sullivan and Wood used this method to follow barrier thickness growth, by anodizing samples for different periods [12]. The quartz microbalance method was used to measure oxide growth on high purity sputtered aluminium samples in acetate buffer solutions at pH 5.9 [27]. The oxide thickness, δ, was calculated from continuous mass change in response to positive potential steps. The results indicated direct proportionality between δ and log(t) in accordance with the direct logarithmic growth law. Due to the nature of these measurements, no distinction of barrier oxide growth and hydrated oxide growth could be made.

2.4 Dissolution kinetics

The barrier oxide dissolution in acid solution is described by the over-all reaction [28]:

$$Al_2O_3 + 6H^+ \Leftrightarrow 2Al^{3+} + 3H_2O \qquad \textbf{(2-18)}$$

Oxide thinning is accompanied by an equally fast oxide growth to maintain a steady-state thickness corresponding to the existing electric field across the film.

In contrast to the film growth results, the available data on the dissolution kinetics of the barrier oxide in aqueous solution are scarce. Oxide growth and dissolution on pure (99.999%) aluminium samples in sodium hydroxide of concentration range 0.1-4 M was investigated by combining single wavelength ellipsometry and potentiostatic measurements [24]. Based on analysis of ellipsometry data it was concluded that formation and dissolution of barrier oxides on aluminium are not the reversible processes. As observed by *in situ* ellipsometry in another study [29], the thickness of barrier oxide at open-circuit conditions in 2 M phosphoric acid and 0.1 M hydrochloric acid decreased in direct proportion to the immersion time during a 2-hour period. The observed variation of open-circuit potential (OCP) in the cathodic direction during dissolution was explained in terms of reduction in oxide thickness. The mechanism of dissolution was proposed to be chemical without much explanation.

Ex situ transmission electron microscope (TEM) analysis [12] was used for evaluation of dissolution rates of barrier oxides on aluminium after negative potential steps. The samples were first anodised at constant voltage for 30 minutes in 0.4 M phosphoric acid. The voltage was then stepped from 115 V to predetermined lower potentials (95, 85 and 75 V) for each sample. By measuring the film thickness on samples removed after various dissolution times, the dissolution rate was evaluated. Due to strong correlations between resulting potential and dissolution rate, it was suggested that the dissolution of barrier oxide is assisted by the applied electric field. These *ex situ* results thus disagree with the dissolution mechanism of barrier aluminium oxide suggested by the *in situ* measurements reviewed further above.

Dissolution rates of barrier oxide formed by anodization of pure aluminium samples in sulphuric acid (15 wt%) were obtained during slow reduction of applied potential by tracking the electrochemical impedance *in situ*, by use of a Wheatstone bridge [13]. The dissolution rate depended on the size of the potential step, higher with larger step. These results were interpreted to indicate field assisted dissolution. A weakness with the used methodology is the lack of steady state conditions that are necessary to ensure good capacitance measurement by use of a Wheatstone bridge or impedance spectroscopy.

A chemically governed dissolution was suggested, in contradiction to the suggested field assisted dissolution above, by work on corrosion of Al alloys in flowing seawater [30]. The study showed that dissolution rates were mass-transfer controlled and unaffected by application of cathodic potentials.

2.5 Steady-state measurements of barrier oxide thickness in aqueous solution

Barrier oxide thicknesses were measured by *in situ* methods such as electrochemical impedance spectroscopy (EIS) [31,32]. The barrier thickness δ is obtained from the EIS capacitance data from the equation

$$\delta = \varepsilon_0 \varepsilon_b A/C \qquad \textbf{(2-19)}$$

where ε_0 is the dielectric constant in vacuum, ε_b is the dielectric constant of the barrier oxide layer, A is the surface area, and C is the capacitance of the oxide layer. ε_b is 9.8±0.5 [33]. These results [31,32,34,35] showed direct proportionality between the steady-state barrier oxide thickness and applied potential. The reported proportionality constant varies. For thicknesses in the range from 0.9 nm to 2.1 nm it is 0.75 nm/V [34]. For thicknesses in the range from 0.5 to 2.5 nm it is 0.85 nm/V [31].

Methods such as *ex situ* ellipsometry [36-38], TEM [11,39] and SEM [12,40] have been used to obtain the barrier oxide thickness after the samples were removed from the solution. The resulting oxide thicknesses were then shown to vary in direct proportion to the anodising voltage. Several authors report a growth rate of 1.2 nm/V when growing thick oxides through anodising [4,41,42], which suggest that thick anodised oxides are relatively stable in air and any changes in thickness are negligible compared to the oxide thickness. However, thin oxide layers, with a thickness in the same range as air formed oxides, may change considerably after removal from the solution, due to the interaction with ambient air. It is of interest to evaluate the apparent differences in proportionality constant between *in situ* and *ex situ* measurements.

2.6 Depassivation of oxide film by trace element Pb

Most of the work reviewed above on oxide growth on Al is related to the pure metal. One of the objectives of the thesis is to investigate to what extent the Cabrera-Mott theory, if applicable to pure Al in aqueous media, could also be applicable to film growth on impure Al. The effect of various trace elements, impurities and alloying elements on the electrochemical and corrosion properties of Al has extensively been investigated in this laboratory during the past several decades, as reviewed in [43,44]. Most of the work has been related to the effect of the surface metallurgy of the aluminium alloys on these properties. Investigation of the effect of trace and alloying elements on modification of oxide properties has received less emphasis. A direct *in situ* study of these elements on oxide growth does not exist. In this thesis (Chapter 5), we have therefore attempted to investigate the effect of a much-investigated trace element, Pb, by use of the *in situ* methodology to be proposed and validated for pure Al in the following two chapters.

Pb is a common trace element in Al alloys because of its presence in the bauxite ore. Its presence in amounts as small as a few ppm has been shown to reduce the passivity of Al oxide by segregation at or near the oxide-metal interface in the form of a nearly continuous nanofilm or discrete nanoparticles. The segregation occurs as a result of heat treatment, especially at temperatures around 600°C, with significance to joining processes, such as brazing and welding. In the presence of chloride ions in the aqueous environment, to which the alloy is subjected, the oxide film with Pb segregation breaks down at potentials significantly more negative than the expected pitting potential of pure Al.

Segregation of Pb by heat treatment at 600°C has extensively been investigated by advanced field emission gun scanning transmission electron microscopy (FE-STEM), and its effect to electrochemical and corrosion properties in chloride media by conventional electrochemical measurements. The effect of heat treatment on surface activation of Pb has been observed by electrochemical characterization on samples heat-treated at temperatures as low as 300°C, with limited success in surface-analytical characterization [45,46]. Depassivation and breakdown of the oxide by segregated Pb were attributed to nearly zero solubility of Pb in Al, resulting in segregation to the surface at a rate increasing with increasing heat-treatment temperature.

The characterization work on model and selected commercial alloys, heat treated at 600°C in air, showed that segregation of Pb in the form of an interfacial nanofilm results from transport of Pb toward the metal surface and its trapping at the metal-oxide interface by the inward growth of γ-Al_2O_3 crystals, readily formed in the presence of oxygen at this temperature. Ample segregation of particulate Pb also occurs first to the grain boundaries in the metal, to the metal surface along the grain boundaries, and finally to the oxide surface through the pores between the γ-Al_2O_3 crystals, as sketched in Fig. 2.3a. The fact that these phenomena occur in alloys with only a few ppm Pb in the bulk, which is much lower than the reported 0.2% solubility of Pb in Al at 600°C, suggested that the solubility must be much lower than the literature value, apparently much closer to zero. Heat treatment at nearly O_2-free environment significantly restricts the growth of γ-Al_2O_3 crystals and, therefore, the formation of the interfacial Pb nanofilm. However, significant segregation of particulate Pb still occurs, as sketched in Fig. 2.3b.

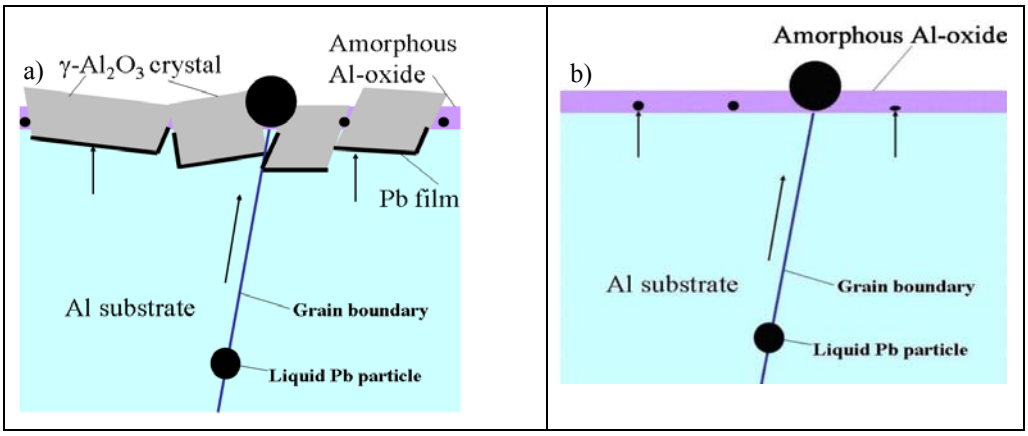

Figure 2.3 Lead segregation to aluminium surface following heat treatment with (a) and without (b) oxygen [44].

2.7 Discussion

The Cabrera-Mott law was originally proposed for oxide growth on metals in dry air or in the presence of oxygen gas. In aqueous media, the law is suggested to be still valid by replacing the potential built up due to electron tunnelling from metal to oxide surface with the potential drop between metal and oxide surface. For anodisation, this is the applied potential as discussed above. However, most reported data, majority under high applied voltage (anodic oxide growth), appear to be related to the high-field growth law, represented by Eq. (2-5). There is a general agreement in the literature, as reviewed above, that the Cabrera-Mott law must also be applicable for high-field barrier oxide growth on aluminium. In particular, the inverse square logarithmic expression, Eq. (2-16), derived for the growth of very thin films, is expected to be applicable for barrier layer growth on aluminium in aqueous media. Such a relationship would be attractive for calculating specific parameters, such as the activation energy W and the limiting film thickness δ_L, which may become useful in quantitative characterization of the growth kinetics. However, there is no data available in the literature validating the Ghez approximation (Eq. 2-16) for the growth of barrier oxide on aluminium immersed in aqueous solution, with special interest in low voltage applications, such as classical electrochemical processes for metal production, batteries and fuel cells.

Such validation of Eq. (2-16) would be useful for justifying its use in investigating the growth kinetics also in the case of aluminium alloys, with the purpose of understanding the effect of alloying and trace elements on the electrochemical properties of the passive surface and depassivation. Practical applications can be envisaged through such an approach in improving the passivity (corrosion resistance) or modifying it (electrodes for electrochemical applications) by various approaches, such as doping the oxide by use of specific alloying elements or solution additives. Similar motivating factors also apply to the study of the film dissolution kinetics, which is still not understood, in view of contradictory claims of rate control by an applied electric field or a chemical dissolution process limited by transport of the dissolved species into the aqueous solution.

The review above indicates, moreover, that the methods commonly used for studying oxide growth are largely indirect, although their power and utility in application cannot be questioned, such as the transient electrochemical techniques. Use of more direct *in situ* methods for monitoring oxide growth and dissolution is very limited. For example, experimental verification of Cabrera-Mott kinetics for growth of thin aluminium oxide films in aqueous solution by accurate and fast thickness monitoring is desirable. Such an approach is also necessary to validate and possibly to

calibrate the transient electroanalytical techniques. Although *ex situ* microscopic measurement of film thickness appears to be applicable to thick anodic films, the same approach is not amenable for the detection of nanometer magnitude changes in film thickness.

Measurement of capacitance to determine film thickness requires steady-state conditions. It is not applicable during transient conditions existing during rate measurement. However, such steady-state measurements can be useful for calibration purposes of direct thickness monitoring, such as by ellipsometry. Such calibration at the beginning and end of a transient measurement, e.g., obtained by a step in the applied potential, would be expected to greatly simplify the measurement and analysis of data obtained simultaneously by ellipsometry and chronoamperometry. Analysis based on single wavelength ellipsometry alone is difficult, as a change in thickness and an equivalent change in refractive index is hard to distinguish, especially for analysing a two-layered oxide structure.

The foregoing literature review indicated that the film thickness-voltage correlation for steady-state barrier layer, which is quite useful for oxide growth studies and applications, is well established as 1.2 nm/V for high voltage anodization of aluminium, the values reported for low voltage thin films vary significantly from one laboratory to another. One reason for this was identified as *ex situ* determination of the oxide thickness, which brings the sample surface in contact with ambient atmosphere, likely to affect the film thickness relative to the *in situ* conditions under which it was formed. Further investigation of the low-voltage barrier thickness vs applied potential is therefore justified by use of more accurate *in situ* experiments.

The experimental techniques under consideration above and the related theoretical framework assume growth and dissolution of a single component, single phase oxide film. It is of interest to explore to what extent the intended methodology can be used for a slightly modified model aluminium alloy containing Pb as the only alloying element in trace amounts, with obvious interest and significance for future improvement of the general approach for application to study film growth and dissolution on less ideal alloy systems. This is intended as a preliminary investigation of the possible challenges in applicability, and consideration of possible improvements. It is expected to obtain ideas for further development of the experimental approach and improvement of the underlying mathematical models for data analysis, while the implementation of the ideas themselves are outside the present scope.

2.8 References

[1] Verwey, E. J. W. *Z. Kristallogr.(A)* **91**, 315 (1935).

[2] Guntherschulze, A. and Betz, H. *Z. Phys.* **92**, 367 (1934).

[3] Hurlen, T. and Guldbransen, E. *Electrochim. Acta.* **39**, 2169-2172 (1994).

[4] Thompson, G. E. *Thin Solid Films* **297**, 192 (1997).

[5] Cabrera, N. and Mott, N. F. *Rep. Prog. Phys.* **12**, 163 (1948-1949).

[6] Atkinson, A. *Rev. Mod. Phys.* **57**, 437-470 (1985).

[7] Vetter, K. J. *Electrochim. Acta* **16**, 1923 (1971).

[8] Khalil, N. and Leach, J. S. L. *Electrochim. Acta* **31**, 1279-1285 (1986).

[9] Lohrengel, M. M. *Mater. Sci. Eng.* **R 11**, 243 (1993).

[10] Diggle, J. W., Downie, T. C., and Goulding, C. W. *Chem. Rev.* **69**, 365 (1969).

[11] Xu, Y. PhD thesis, University of Manchester, Manchester, UK (1983).

[12] O'Sullivan, J. P. and Wood, G. C. *Proc. R. Soc. London, Ser. A* **317**, 511-543 (1970).

[13] Diggle, J. W., Downie, T. C., and Goulding, C. W. *J. Electrochem. Soc.* **116**, 737 (1969).

[14] Verwey, E. J. W. *Physica(A)* **2**, 1059 (1935).

[15] Burstein, G. T. and Davenport, A. J. *J. Electrochem. Soc.* **136**(4), 936-941 (1989).

[16] Kirk Jr., C. and Huber Jr., E. *Surf. Sci.* **9**(2), 217-245 (1968).

[17] Fehlner, F. P. and Mott, N. *Oxid. Met.* **2**, 59 (1970).

[18] Davies, J. A., Domeij, B., Pringle, J. P. S., and Brown, F. *J. Electrochem. Soc.* **112**, 675-680 (1965).

[19] Eley, D. D. and Wilkinson, P. R. *Proc R Soc London, Ser. A* **254**(1278), 327-342 (1960).

[20] Fromhold, A. T. *Theory of Metal Oxidation Volume 1 - Fundamentals*. North Holland Publising Company, Amsterdam, Netherlands (1976).

[21] Ghez, R. *J. Chem. Phys.* **58**, 1838-1843 (1973).

[22] Gudic, S., Radosevic, J., Krpan-Lisica, D., and Kliskic, M. *Electrochim. Acta* **46**(16), 2515-2526 (2001).

[23] Hasenay, D. and Seruga, M. *J. Appl. Electrochem.* **37**(9), 1001-1008 (2007).

[24] Greef, B. and Norman, C. *J. Electrochem. Soc.* **132**, 2362 (1985).

[25] Gils, S. V., Melendres, C., Terryn, H., and Stijns, E. *Thin Solid Films* **455-456**, 742-746 (2004).

[26] Lukac, C., Lumsden, J. B., Smialowska, S., and Staehle, R. W. *J. Electrochem. Soc.* **122**(12), 1571-1579 (1975).

[27] Gnoinski, J., Grundwell, F., and Orchard, S. *Mater. Sci. Forum* **185-188**, 667-676 (1995).

[28] Diggle, J. W., Downie, T. C., and Goulding, C. W. *Electrochim. Acta* **15**, 1079-1093 (1970).

[29] Stein, N., Rommelfangen, M., Hody, V., Johann, L., and Lecuire, J. *Electrochim. Acta* **47**, 1811-1817 (2002).

[30] Nisancioglu, K. *Corrosion behaviour and protection of copper and aluminium alloys in seawater, p.145, European Federation of Corrosion Publications No. 50*. Woodhead Publishing, Cambridge, UK, (2007).

[31] Gudic, S., Radosevic, S., and Kliskic, M. *J. Appl. electrochem.* **26**, 1027-1035 (1996).

[32] Bessone, J., Salinas, D., Mayer, C., Ebert, M., and Lorenz, W. *Electrochim. Acta* **37**, 2283-2290 (1992).

[33] Harkness, A. C. and Young, L. *Can. J. Chem.* **44**, 2409 (1966).

[34] Bessone, J., Mayer, C., Jüttner, K., and Lorenz, W. J. *Electrochim. Acta* **28**, 171-175 (1983).

[35] Hurlen, T., Lian, H., Ødegård, O., and Våland, T. *Electrochim. Acta.* **29**, 579-585 (1984).

[36] Gils, S. V., Melendres, C., and Terryn, H. *Surf. Interface. Anal.* **35**, 387-394 (2003).

[37] R. Kötz, Schnyder, B., and C.Barbero. *Thin Solid Films* , 63 (1993).

[38] Brevnov, D. A., Rao, G. V. R., Lopez, G., and Atanassov, P. B. *Electrochim. Acta* **49**, 2487 (2004).

[39] Takahashi, H. and Nagayama, M. *Electrochim. Acta* **23**, 279 (1978).

[40] Habazaki, H., Shimuzu, K., Skeldon, P., Thompson, G. E., and Wood, G. *Thin Solid Films* **300**, 131 (1997).

[41] Hass, G. *J. Opt. Soc. Amer.* **39**, 532 (1949).

[42] Deryagin, B. V. and Friedland, R. M. *Z. tech. Phys. U.S.S.R* **18**, 1443 (1948).

[43] Sukiman, N. L., Zhou, X., Birbilis, N., Hughes, A., Mol, J. M. C., Garcia, S. J., Zhou, X., and Thompson, G. E. *Durability and Corrosion of Aluminium and Its Alloys: Overview, Property Space, Techniques and Developments, Aluminium Alloys - New Trends in Fabrication and Applications, Chapter 2*. INTECH, Rijeka, Croatia, (2012).

[44] Anawati, Graver, B., Nordmark, H., Zhao, Z., Frankel, G., Walmsley, J., and Nisancioglu, K. *J. Electrochem. Soc.* **157**, C313-C320 (2010).

[45] Kurt, K., Diplas, S., Walmsley, J. C., and Nisancioglu, K. *J. Electrochem. Soc.* **160**, C542 (2013).

[46] Senel, E. *Anodic Activation of Aluminium by Trace Element Gallium*. PhD thesis, Norwegian University of Science and Technology, Trondheim, Norway (2013).

3 *In situ* ellipsometric and electrochemical characterisation of oxide formed on aluminium in acetate buffer

Abstract

Novel methodology was developed for characterisation of oxide properties on pure aluminium in aqueous solution by use of visual light ellipsometry (VISSE) and electrochemical impedance spectroscopy (EIS) under controlled environmental conditions. Control of the electrode potential and solution pH, chemistry and temperature gave well-defined and reproducible oxide properties. The change in the thickness of both thin barrier and hydrated layers of the oxide was monitored, *in situ* by multi-wavelength ellipsometry. Thicknesses of the layers were directly related to the applied potential in the range -0.7 to 0.3 V_{SCE}. For the barrier layer, the change in steady-state thickness in acetate buffer in the pH range 5.6-6.3 at 22ºC was 1.1 nm/V, in agreement with the well-accepted thickness-voltage relationship for the barrier layer, which thereby partly validated the developed methodology. Long period (days) of potentiostatic polarisation was necessary to obtain a steady state hydrated oxide thickness. Change in the refractive index during this period was attributed to increasing porosity or hydration. The steady state thickness and the refractive index of the hydrated layer varied with the applied potential by about 60 nm/V and -0.26/V, respectively.

3.1 Introduction

The properties of the oxide formed on aluminium in an aqueous environment have been investigated extensively by theoretical [1,2] and experimental studies applying electrochemical methods [3,4], x-ray photoelectron spectroscopy [5], electron microscopy [6,7] and ellipsometry [8,9]. The barrier thickness, for thick barrier films around 100 nm, is shown *ex situ* to grow fast after a positive potential step and to decrease slowly after a negative potential step, with the thickness of the barrier layer proportional to the applied potential [6]. The growth mechanism is explained by the oxidation of aluminium metal at the metal-oxide interface to form Al^{3+} ions and adsorption of O^{2-} ions at the oxide-solution interface, by dissociation of water. The layer grows either by Al^{3+} egress through the barrier oxide or ingress of O^{2-} into the aluminium-barrier oxide interface, driven by the high electric field developed across the barrier oxide [10]. Al_2O_3 is formed by the reaction between Al^{3+} and O^{2-} ions either at the metal-oxide interface or at the oxide-solution interface. This model is known as the high field model, which is based on the work by Güntherschulze, Betz, Verwey, Mott and Cabrera [11-13]. A porous hydrated oxide is further formed between the solution and the barrier oxide by hydration of aluminium ions that migrate through the barrier oxide and by dissolution of the barrier oxide and re-deposition in the form of a hydrated oxide [10].

Electrochemical impedance spectroscopy (EIS) and visual spectroscopic ellipsometry (VISSE) are *in situ* methods for studying the oxide properties of thin films in solution. Both methods require physical and mathematical models by which the experimental results can be analysed. The electrochemical interface for EIS is often represented in terms of an equivalent circuit based on a deterministic model of the kinetics of the electrochemical reaction at the electrode surface and transport of reactants and reaction products to and from the electrode surface. It can also be based on empirical, stochastic and intuitive considerations.

A frequently used deterministic impedance model of the passive oxide covered metal surface is expressed by the equivalent circuit shown in Fig 3.1 [3,14,15]. Derivation of the circuit and the definition of the parameters will be discussed in more detail in the next section. The inverse

of obtained capacitance is the reciprocal sum of the double-layer and barrier-layer capacitances, usually dominated by the latter. Thus, it is inversely proportional to the oxide thickness. The inductance is related to the relaxation of intermediately adsorbed species at the metal-barrier oxide interface and/or barrier-oxide-solution interface [16-18].

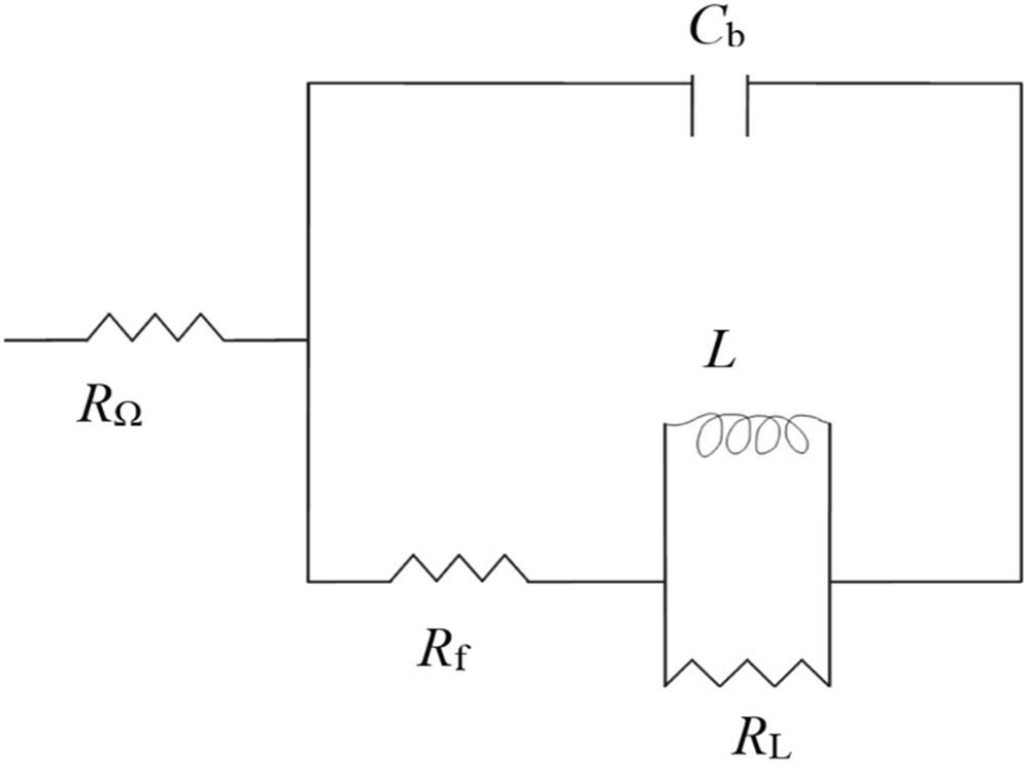

Figure 3.1 Impedance model describing the charge and mass transfer processes on oxide covered aluminium surface. The parameters are defined in the text.

Other frequently used models are based on intuitive and empirical considerations. The transfer function of a single layer is represented as a capacitance in parallel with a resistance. Each new layer is represented by adding a new single layer transfer function in series to the total transfer function. Additional transfer functions are added to describe the effect of additional factors, such as porosity and effect of pitting [19,20].

In situ ellipsometry has been used earlier to determine the thickness changes due to anodization and dissolution of both barrier and porous oxides on aluminium [21,22]. A major problem with this approach is the lack of capability to monitor fast thickness changes of the thin barrier layer, as the data acquisition time for spectroscopic measurements is larger than the time constant of the changes. An additional difficulty is the inability to distinguish between thin composite layers of similar refractive index, such as a duplex film consisting of a thin and dense Al_2O_3 barrier layer and a porous hydrated layer [22]. Determination of the absolute barrier thickness is not possible in this case. The capability of monitoring the kinetics of the barrier layer is restricted by the trade-off between acquisition speed and wavelength span [23]. This limits the measurements either to a few selected wavelengths to obtain fast thickness change of the sum of the two layers [9],

or full-length spectra with possibility to obtain the thickness of both layers at low time resolution [24]. The latter is further restricted to barrier layer thicknesses of at least 10 nm.

This paper presents *in situ* measurement methodology, combining EIS and VISSE, for studying the properties of thin oxide films (2-4 nm) on aluminium in aqueous solution. The EIS model for the oxide covered aluminium surface, based on the work by Armstrong and Edmondson [25], was used to determine the absolute steady-state thickness of the barrier layer. Since the EIS technique is not sensitive to the properties of the hydrated oxide layer, ellipsometry is needed to obtain the steady state thickness of the hydrated layer. Thickness changes in the oxide layers with respect to time were monitored by use of rapid acquisition multi-wavelength VISSE. Particular attention was given to the thickness and dissolution kinetics of the barrier layer.

3.2 Theoretical Background

3.2.1 Physicochemical Model

The barrier layer is formed by oxidation of aluminium to form Al^{3+} ions in the presence of a positive electric field and the reaction of these ions with oxygen ions at the metal-oxide interface. The oxygen ions, which are formed by dissociation of adsorbed water at the barrier oxide-solution interface, migrate to the metal-oxide interface, assisted by the electric field [1,10,17,26]. In acidic solutions, the barrier oxide has been shown to grow at the oxide-aluminium interface, by oxygen ion ingress through the film [10]. Barrier oxide growth at the barrier oxide-hydrated oxide interface, by Al^{3+} egress, is negligible. A certain fraction of Al^{3+} ions is, depending on interfacial conditions at the barrier oxide-hydrated oxide interface, shown to migrate directly into the solution without producing barrier oxide [10]. The rate of charge transfer reactions decreases as a steady-state barrier oxide thickness is attained as the rate of film formation at the metal-oxide interface becomes equal to the rate of film dissolution at the barrier oxide-hydrated oxide interface [2,10,27-30]. A steady-state electric field (the bias) is maintained by the continuing flux of O^{2-} and Al^{3+} ions through the film. Oxide formation is balanced by an equal rate of chemical film dissolution at the barrier layer-solution interface at steady state. The steady-state thickness of the barrier oxide is determined by the applied potential [2,12] and solution properties [31]. Aluminium ions, which migrate through the barrier layer, and those, which are formed by chemical dissolution of the barrier layer, are responsible for growth of the hydrated layer by hydration and precipitation on the barrier layer to form a porous structure [32]. The physical model of the oxide covered aluminium surface and the charge and mass transfer processes described are sketched in Fig. 3.2.

In view of the foregoing considerations, aluminium is oxidised at the metal-oxide interface according to reaction

$$Al \rightarrow Al^{3+} + 3e^{-} \qquad \textbf{(3-1)}$$

to form Al^{3+} ions. Adsorbed oxygen ions are formed by dissociation of water at the barrier layer surface,

$$H_2O + 2e^{-} \rightarrow 2H + O^{2-}_{ads} \qquad \textbf{(3-2)}$$

The adsorbed oxide ions are incorporated into the barrier layer,

$$O_{ads}^{2-} \rightarrow O^{2-} \quad \textbf{(3-3)}$$

and migrate toward the metal surface, assisted by the electric field [2,12]. The oxide is formed by the reaction between aluminium and the oxide ions at the metal-oxide interface according to

$$2Al^{3+} + 3O^{2-} \rightarrow Al_2O_3 \quad \textbf{(3-4)}$$

Oxide growth at low current density and in acidic solution occurs mainly by the reaction at the metal-oxide interface, as discussed above [10,17]. Aluminium ions, not consumed in oxide formation, are transported into the solution together with the ionic species formed by the dissolution of the barrier oxide.

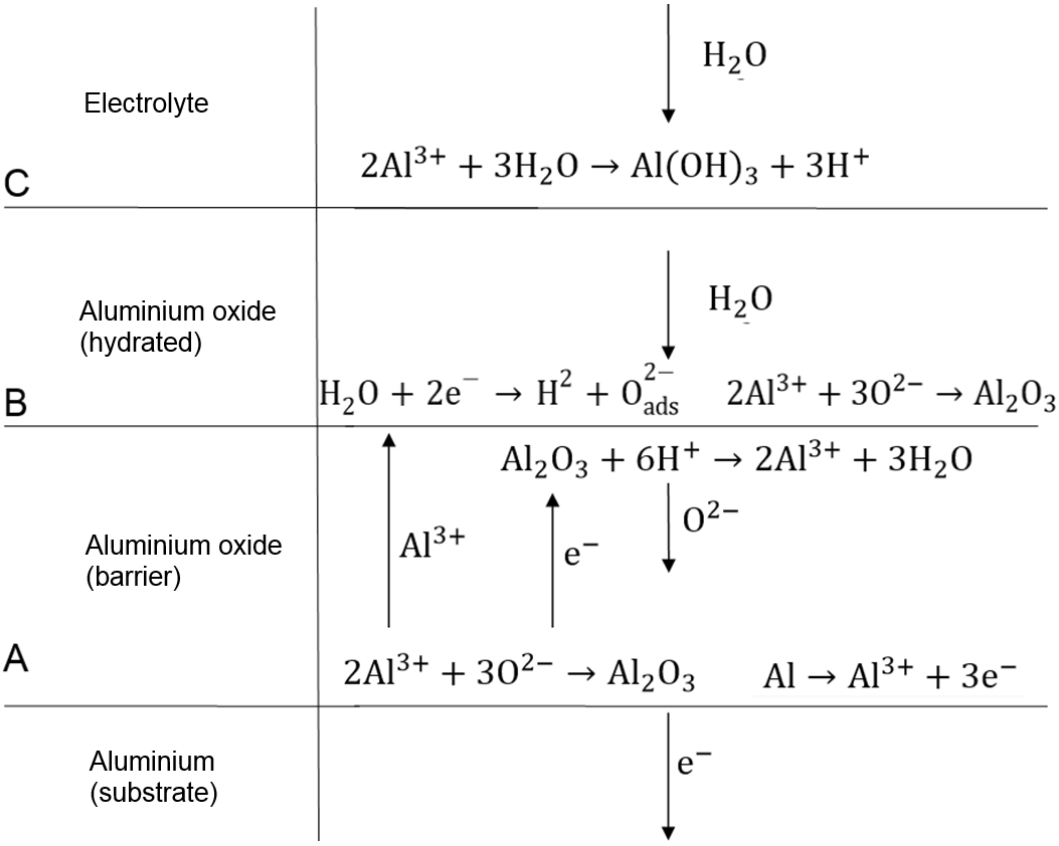

Figure 3.2 Interfacial reactions and transport of ions in the oxide. A, B and C are the metal/barrier, barrier/hydrated layer and hydrated layer/solution interfaces, respectively. The arrows show the direction of transport of various species in the oxide.

3.2.2 EIS Model

Based on the paper by Armstrong and Edmondson [25], the effect of a small periodic perturbation $\Delta E\exp(j\omega t)$ of the applied potential E on the fluxes of aluminium N_{Al} and oxygen ions N_{O} near the aluminium surface, as sketched in Fig. 3.2, can be written respectively as

$$N_{\mathrm{Al}} = N_{\mathrm{Al}_0} + \left(\frac{\partial N_{\mathrm{Al}}}{\partial E}\right)_{\Gamma} \Delta E\exp(j\omega t) + \left(\frac{\partial N_{\mathrm{Al}}}{\partial \Gamma}\right)_{E} \Delta\Gamma\exp(j\omega t) \qquad \textbf{(3-5)}$$

and

$$N_{\mathrm{O}} = N_{\mathrm{O}_0} + \left(\frac{\partial N_{\mathrm{O}}}{\partial E}\right)_{\Gamma} \Delta E\exp(j\omega t) + \left(\frac{\partial N_{\mathrm{O}}}{\partial \Gamma}\right)_{E} \Delta\Gamma\exp(j\omega t) \qquad \textbf{(3-6)}$$

where $\Delta\Gamma\exp j\omega t$, is the corresponding perturbation of the excess of aluminium ions over the oxygen ions, Γ, and it is related to the fluxes by

$$\frac{\partial \Gamma}{\partial t} = \frac{\partial}{\partial t}\left(\Gamma_0 + \Delta\Gamma\exp(j\omega t)\right) = j\omega\,\Delta\Gamma\exp(j\omega t) = aN_{\mathrm{Al}} - bN_{\mathrm{O}} = 3N_{\mathrm{Al}} - 2N_{\mathrm{O}} \qquad \textbf{(3-7)}$$

where the factors *a* and *b* are determined according to the requirement that $\frac{\partial \Gamma}{\partial t} = 0$ when the ratio of fluxes are given as $N_{\mathrm{O}} = \frac{3}{2}N_{\mathrm{Al}}$, according to $2\mathrm{Al}^{3+} + 3\mathrm{O}^{2-} \rightarrow \mathrm{Al_2O_3}$. Hence,

$$\Delta\Gamma = \frac{\left[3\left(\frac{\partial N_{\mathrm{Al}}}{\partial E}\right)_{\Gamma} - 2\left(\frac{\partial N_{\mathrm{O}}}{\partial E}\right)_{\Gamma}\right]\Delta E}{j\omega - 3\left(\frac{\partial N_{\mathrm{Al}}}{\partial \Gamma}\right)_{E} + 2\left(\frac{\partial N_{\mathrm{O}}}{\partial \Gamma}\right)_{E}} \qquad \textbf{(3-8)}$$

The faradaic admittance, related to passage of current due to migration of the charged species across the interface, is given as

$$Y_f = \frac{3\mathrm{F}\Delta N_{\mathrm{Al}}}{\Delta E\exp(j\omega t)}. \qquad \textbf{(3-9)}$$

where F is Faraday's constant. By inserting Eq. (3-5), (3-6), and (3-8) into (3-9) we obtain:

$$Y_f = 3\mathrm{F}\left(\left(\frac{\partial N_{\mathrm{Al}}}{\partial E}\right)_{\Gamma} + \left(\frac{\partial N_{\mathrm{Al}}}{\partial \Gamma}\right)_{E} \frac{\left[3\left(\frac{\partial N_{\mathrm{Al}}}{\partial E}\right)_{\Gamma} - 2\left(\frac{\partial N_{\mathrm{O}}}{\partial E}\right)_{\Gamma}\right]}{j\omega - 3\left(\frac{\partial N_{\mathrm{Al}}}{\partial \Gamma}\right)_{E} + 2\left(\frac{\partial N_{\mathrm{O}}}{\partial \Gamma}\right)_{E}}\right) \qquad \textbf{(3-10)}$$

By defining

$$\frac{1}{R_{\infty}} = 3\mathrm{F}\left(\frac{\partial N_{\mathrm{Al}}}{\partial E}\right)_{\Gamma} \qquad \textbf{(3-11)}$$

,

$$\frac{1}{R_0} = \frac{1}{k}\left[3\left(\frac{\partial N_{\mathrm{Al}}}{\partial E}\right)_{\Gamma} - 2\left(\frac{\partial N_{\mathrm{O}}}{\partial E}\right)_{\Gamma}\right] 3F\left(\frac{\partial N_{\mathrm{Al}}}{\partial \Gamma}\right)_{E} \tag{3-12}$$

and

$$k = 2\left(\frac{\partial N_{\mathrm{O}}}{\partial \Gamma}\right)_{E} - 3\left(\frac{\partial N_{\mathrm{Al}}}{\partial \Gamma}\right)_{E} \tag{3-13}$$

Y_f can be expressed as

$$Y_{\mathrm{f}} = \frac{1}{R_{\infty}} + \frac{k}{j\omega + k}\frac{1}{R_0} \tag{3-14}$$

By further defining the parameters

$$\frac{1}{R_{\mathrm{f}}} = \frac{1}{R_0} + \frac{1}{R_{\infty}} \tag{3-15}$$

,

$$R_{\mathrm{L}} = R_{\infty} - R_{\mathrm{f}} \tag{3-16}$$

and

$$L = \frac{\dfrac{1}{R_0 k}}{\left(1/R_{\infty} + 1/R_0\right)^2} \tag{3-17}$$

Eq. (3-14) becomes

$$Y_{\mathrm{f}} = \left[R_{\mathrm{f}} + \left(\frac{1}{R_{\mathrm{L}}} + \frac{1}{j\omega L_{\mathrm{p}}}\right)^{-1}\right]^{-1}. \tag{3-18}$$

The nonfaradic admittance is normally assumed to be separable from the faradaic impedance and expressed as $j\omega C$ [33]. The total admittance will then be given as the sum of the faradic and non-faradic admittances

$$Y = Y_{\mathrm{f}} + Y_{\mathrm{nf}} = \left[R_{\mathrm{f}} + \left(\frac{1}{R_{\mathrm{L}}} + \frac{1}{j\omega L} \right)^{-1} \right]^{-1} + j\omega C \qquad \textbf{(3-19)}$$

where C is given by a series combination of the capacitances due to charging of the electric double layer and the barrier oxide,

$$1/C = 1/C_{\mathrm{dl}} + 1/C_{\mathrm{b}}. \qquad \textbf{(3-20)}$$

The equivalent circuit corresponding to Eq. (3-19) is shown in Fig. 3.1 after adding the ohmic resistance in the solution R_{Ω}. The complex impedance of the equivalent circuit is sketched on a Nyquist plot in Fig. 3.3, showing the graphical representation of the circuit components. The same equivalent circuit was used by Bessone et al. [14] for study of barrier layer formed by anodising of aluminium in ammonium tartrate. The resistance $R_{\mathrm{p}} = \lim_{\omega \to 0} \mathrm{Re}\{Z_{\mathrm{f}}\} = R_{\mathrm{f}}$ is the polarisation resistance [14]. $R_{\mathrm{t}} = \lim_{\omega \to \infty} \mathrm{Re}\, Z_{\mathrm{f}} = R_{\mathrm{f}} + R_{\mathrm{L}}$ is the charge transfer resistance [14]. The inductance, L, represented by the negative semicircle in Fig. 3.3, is related to changes in the fluxes of charged species in the barrier layer as determined in a complex manner by their adsorption rates at various interfaces sketched in Fig. 3.2 and exchange rates at the metal-barrier oxide interface [16-18].

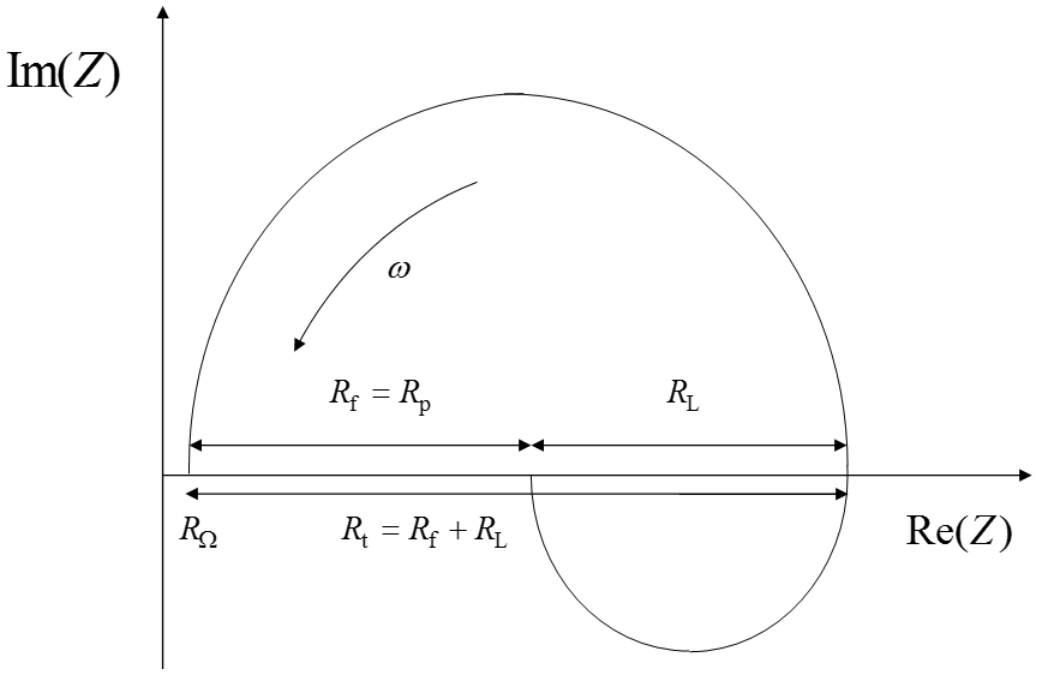

Figure 3.3 Schematic Nyquist plot of the impedance *Z* according to the model in the text and equivalent circuit in Fig. 3.1. The relation between the parameters defined in the text and the complex impedance is indicated in the figure.

The thickness of the oxide layer is given by [2,14]

$$d = \varepsilon_0 \varepsilon_b A / C_b , \tag{3-21}$$

where ε_0 is the dielectric constant in vacuum, ε_b is the dielectric constant of the barrier oxide layer, A is the surface area, and C_b is the capacitance of the oxide layer as defined in Eq. (3-20). The double layer capacitance, C_{dl}, is assumed to be much larger than the oxide capacitance [15,34]. The measured capacitance, C, is then nearly equal to C_b. For the barrier layer on aluminium, ε_b is about 10 [3,35,36].

The measured impedance data were fitted to the model above by a complex non-linear least squares algorithm, in which

$$\chi^2 = \sum_{i=1}^{n} \left[(y_i - f(x_i)) / w_i \right]^2 \tag{3-22}$$

was minimized over all the measured frequencies i. y_i is the measured complex impedance at frequency i, $f(x)$ is the impedance calculated from the model, and w_i, the weighting factor, is the modulus of the impedance data, $w_i = \mathrm{Re}(y_i) + j\,\mathrm{Im}(y_i) = \sqrt{\mathrm{Re}(y_i)^2 + \mathrm{Im}(y_i)^2}$. The average standard error of an obtained EIS parameter p with average $\bar{p}$ is calculated from

$$\sigma = \sqrt{\frac{1}{n} \sum_{i=1}^{n} [p_i - \bar{p}]^2} \tag{3-23}$$

This is a useful parameter for estimating the smoothed out scatter in the parameters calculated from the impedance data.

3.2.3 VISSE Modelling and Methodology

Spectroscopic ellipsometry (SE) is based on the measurement of elliptical polarisation of light reflected from the surface of a sample. The complex reflectance ratio of light polarised parallel, $\tilde{R}_p$, and perpendicular, $\tilde{R}_s$, to the plane of incidence is expressed as [37,38]

$$\rho = \frac{\tilde{R}_p}{\tilde{R}_s} = \frac{|R_p|}{|R_s|} \exp\left(i(\delta_p - \delta_s)\right) = \tan\Psi \exp(i\Delta) \tag{3-24}$$

where $|R_p|$ and $|R_s|$ are the reflection amplitudes of the p and s polarised light, respectively. δ_p and δ_S are their corresponding changes in phase between incident and reflected light. The parameters Ψ and Δ defined by Eq. (3-24) are measurable by the SE technique as a function of wavelength [39,40]. The film thickness ($\Delta\delta$) and refractive index (n) can be obtained by curve fitting the measured data for Ψ and Δ to an ellipsometric model of the surface [22,37]. In such a model, the surface is described as a stack of parallel layers of various thicknesses and refractive

indices, which appear as the undetermined parameters in the model. The parameters are determined by complex non-linear least square (CNLS) fitting of Ψ and Δ which vary as functions of layer thicknesses and refractive indices. Azzam and Bashara have developed a mathematical relationship between the ellipsometric parameters and the film properties (n and δ) of a multilayered surface [39].

Two asymptotic models were used in this work for obtaining the properties of the composite oxide from the response of the ellipsometric parameters to a step change in the applied potential between a reference electrode in the solution and the aluminium sample. In treating the short-time response (barrier oxide model), the barrier layer thickness was a variable, while the hydrated layer properties (thickness and refractive index) were assumed constant. This model was suitable for fitting the short-time data to determine rapid changes in the barrier-layer thickness. In modelling the long-time response, the hydrated oxide properties were variables, while the barrier layer thickness was assumed to be a constant (hydrated oxide model). The constant thickness was set equal to the steady-state thickness obtained by EIS. By curve fitting of the long-time data in this manner, the refractive index and thickness of the hydrated layer was obtained. The asymptotic approach is considered reasonable for the treatment of the ellipsometric data since the time constants for the relaxation of the barrier and hydrated oxide layers are of different orders of magnitude in view of the electrochemical reaction kinetics and transport properties discussed above.

3.2.3.1 Barrier oxide model

The two-layer model, shown in Fig. 3.4, consists of the dense barrier layer adjacent to the metal and the porous hydrated layer on top of the barrier layer. In addition, the aluminium layer is modelled as a semi-infinite substrate and the electrolyte as the ambient surrounding. It is applicable for modelling the short-time response of the oxide thickness to a step change in the applied potential. During this period, the thickness of the barrier layer changed at a fast rate, while the slow change in the properties of the hydrated layer thickness was a secondary effect. The refractive index of the hydrated layer, which was assumed constant during barrier layer growth, was obtained from the ellipsometry data after the barrier layer thickness reached steady state. By using this value and the data given in Fig. 3.4, the relaxation in the barrier layer thickness was then obtained by curve fitting the ellipsometric spectra calculated from the Azzam-Bashara model to the measured ellipsometry data. The steady state barrier oxide thickness was determined independently by EIS, and it was used to calibrate the ellipsometric relaxation data.

The refractive index n_{Al} and absorption coefficient, k, of aluminium were obtained from the work by Palik [40] as a function of wavelength, λ. The values specified in Fig. 3.4 are the indices at $\lambda = 400$ nm. Refractive index of the amorphous barrier layer was obtained from Gils et al. [24], which is on the average about 5 % lower than that for crystalline aluminium oxide [41].

This model does not take into account any roughness at the metal-barrier layer, barrier layer-hydrated layer and hydrated layer-solution interfaces. To investigate the effect of roughness at each interface, the roughness was modelled as an additional thin layer, with properties corresponding to the properties of the two interfaces averaged by use of the effective medium approximation (EMA) [42]. However, this approach did not significantly improve the curve fitting and the accuracy of the calculated properties, indicating that the scale of surface roughness was much smaller than the wavelength of incident light used in the measurements.

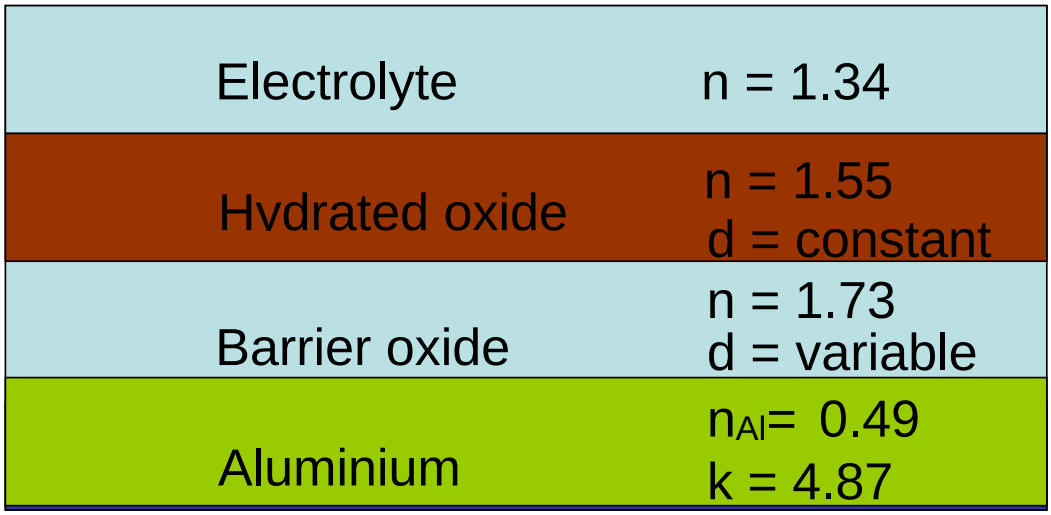

Figure 3.4 Two-layer ellipsometric model used for analyzing the measured VISSE data.

3.2.3.2 Hydrated oxide model

Since changes in the barrier layer thickness in response to a potential change occurred fast, the long-term response of the oxide, which was mainly due to changes in the thickness of the hydrated layer, was treated by a modified two-layer model. In this model, the barrier-layer thickness was assumed constant and equal to its steady-state thickness determined by EIS. Both the thickness and the refractive index of the hydrated layer were allowed to vary with significant numerical advantage in curve fitting, as will be discussed further in Section 3.5. A similar approach to ellipsometric data analysis has been presented in other applications [22,23].

The hydrated oxide layer is a fibrillar layer with pores filled with the solution, which is assumed to have the refractive index of water. The measured refractive index ε of the hydrated oxide layer is a composite value determined by the index of hydrated aluminium oxide and water in the pores.

An important property of the hydrated oxide layer is the effective mass thickness, which is related to the measured properties by the following relations. The measured refractive index is related to the dielectric constant as

$$\varepsilon = (n + ik)^2 \tag{3-25}$$

where $k = 0$ for a non-absorbing medium. The dielectric constant is related to the electric susceptibility χ_{sup} by the equation

$$\varepsilon - \varepsilon_{H_2O} = \chi_{sup} \propto N \tag{3-26}$$

where ε_{H_2O} is the dielectric constant of water and N is the density of polarised dipoles per unit volume within the medium. An effective mass thickness of the hydrated aluminium oxide, d_{eff},

which is the total number of polarisers per unit area, can be defined by the expression

$$d_{\text{eff}} = \chi d_{\text{hyd}} = \frac{\left(n_{\text{hyd}}^2 - n_{\text{H}_2\text{O}}^2\right)}{\left(n_{\text{Al}_2\text{O}_3}^2 - n_{\text{H}_2\text{O}}^2\right)} d_{\text{hyd}} \qquad \textbf{(3-27)}$$

where n_{hyd} and d_{hyd} are the refractive index and thickness of the hydrated oxide layer, respectively, and $n_{\text{H}_2\text{O}}$ is the refractive index of water.

3.3 Experimental

Pure aluminium (99.99%) samples were metallographically polished through 1 μm diamond paste. The specimens were mounted in a specimen holder exposing the polished surface to the solution and to the incident light beam of the ellipsometer. The holder also provided electronic contact to the external electrochemical equipment, consisting of a potentiostat and a frequency response analyser. The holder was placed in an electrochemical cell equipped with optical windows for the incident and reflected light, as shown in Fig. 3.5. The cell was sealed from ambient air by purging the upper part of the cell with an inert gas for some of the experiments. The cell was also equipped with a Pt counter electrode and a saturated Hg/Hg_2SO_4 reference electrode for the electrochemical measurements. The potentials are reported with respect to this reference electrode. The test electrolyte was a solution of acetic acid and sodium acetate (Na-acetate buffer) of varying concentration as summarised in Table 3.2. The buffer concentration is reported in terms of the acetic acid concentration in mM and pH in the remainder of this chapter. The temperature was maintained at ambient 22±1°C in an air-conditioned laboratory.

Table 3.1 Properties of test solutions.

pH[1]	[HAc] (mM)	[NaAc] (g/L)	[HAc] g/L
5.6	120	68.0	7.16
5.6	60	34.0	3.58
6.3	25	64.4	1.52
6.3	13	32.2	0.762

After placing the specimen in the test solution, the oxide was first stabilised by applying a constant applied potential (DC bias). After steady state was obtained, the applied potential was stepped to a new, predetermined value. Long-term changes in the oxide thickness in response to the potential change were monitored by VISSE in the wavelength range 295-826 nm. One such measurement was performed every half hour. EIS was measured after the oxide thickness became stable after several hours, by superimposing a frequency-modulated potential on the DC bias and

[1] The pH values are calculated by the buffer equation from acetic acid and sodium acetate concentration.

measuring the resulting impedance in the range 10^4 Hz to 1 mHz. The DC bias was stepped again to a new value and the above procedure was repeated.

Additional set of ellipsometric measurements were performed at 250 equally spaced wavelengths, in a smaller range from 431 nm to 849 nm. The potential was stepped as above. However, only the barrier thickness was given time to stabilise before the potential was stepped for the next measurement. All 250 wavelengths were measured simultaneously, and the acquisition time was 10 seconds per measurement. The purpose with this set of experiments was thus to investigate the short-time growth and dissolution of the oxide soon after the potential step.

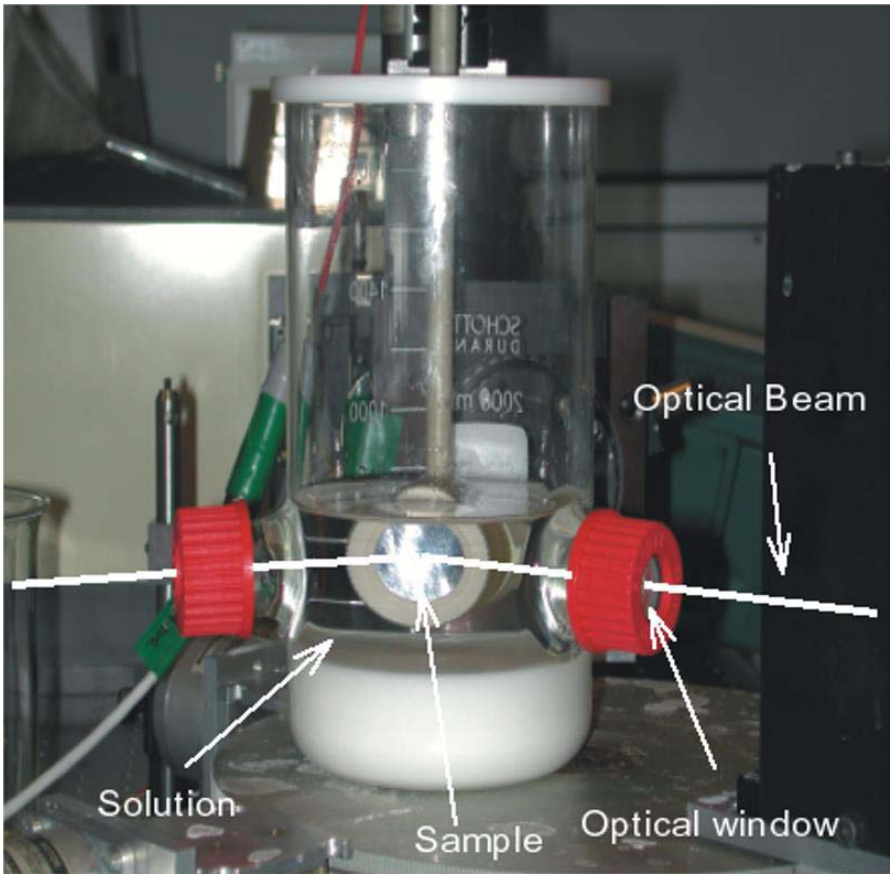

Figure 3.5 The cell for performing electrochemical and ellipsometric measurements. The sample and electrodes (not shown) are immersed into the solution. The cell is equipped with optical windows for transmission of light at normal incidence.

The oxide thickness was measured also *ex situ* by use of TEM. Cross sectional foils of the surface were prepared from the samples used in the foregoing *in situ* analysis. The procedures for sample preparation and TEM operation were described by Sævik *et al*. [43]. The aluminium, the barrier oxide and the hydrated layer phases can be distinguished by their differing grey scale levels in the TEM images, which was used for determining the boundaries between the phases and the oxide layer thicknesses.

3.4 Results

3.4.1 EIS

The EIS spectra obtained at various potentials were analysed according to the model described in Section 3.2.2. The measured and the calculated data obtained from curve fitting are shown in Fig. 3.6 for a selected applied potential, solution pH and solution concentration. Table 3.2 shows the calculated parameters for the equivalent circuit in Fig. 3.1 for different applied potentials. The resulting χ^2 values and the standard error of fitted parameters, as defined in Eq. (3-22) and (3-23), respectively, are included in the table. A good agreement between the measured and calculated data exists, as indicated by the low χ^2 values and estimated scatter in the calculated parameters presented in Table 3.2.

spyder

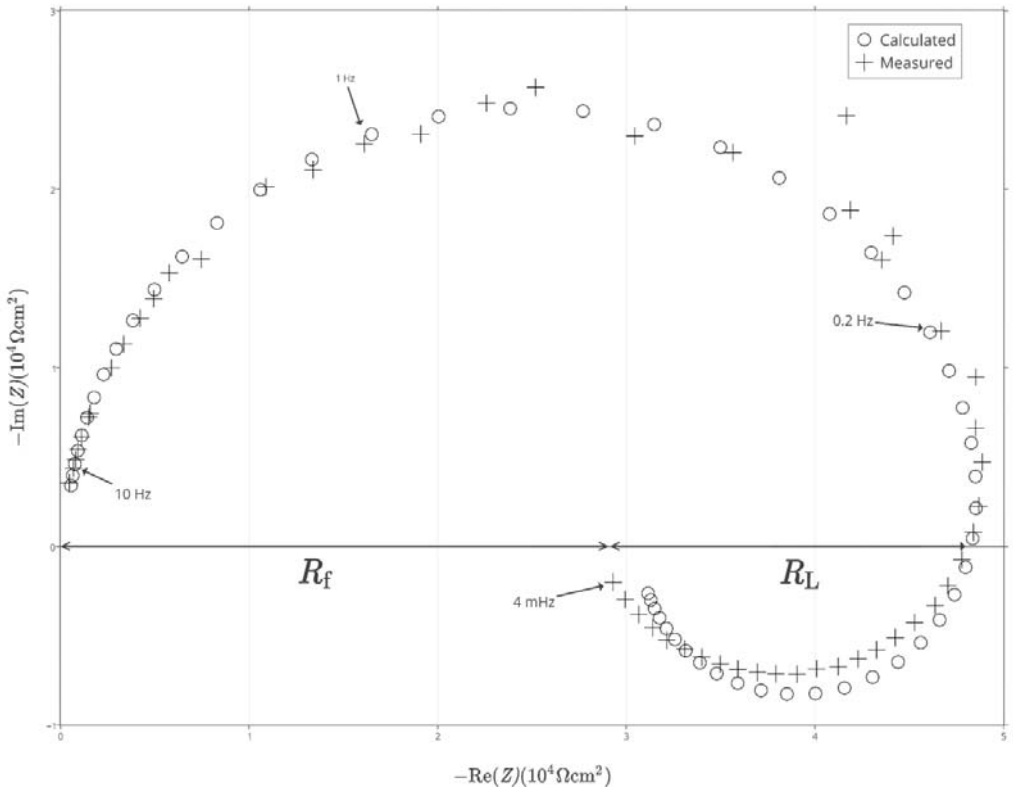

Figure 3.6 Comparison of measured and calculated impedance data for an aluminium sample at a bias potential of -700 mV vs. Hg/Hg_2SO_4 reference electrode in 120 mM acetic acid buffer at pH = 5.6.

Table 3.2 Values of the electronic components of the equivalent circuit (Fig. 3.3) and thickness of the barrier layer δ calculated by analysis of the EIS data obtained in 120 mM acetate buffer at pH=5.6.

Applied Potential	C_b	L	R_f	R_L	χ^2	δ
(mV)	**(10^{-6} F/cm^2)**	**(10^5 H)**	**(10^4 Ωcm^2)**	**(10^4 Ωcm^2)**	**(10^{-3})**	**(nm)**
-100	3.31± 0.04	1.21± 0.07	3.09± 0.05	2.47± 0.06	1.74	2.67±0.03
-400	3.94± 0.06	1.24± 0.09	2.94± 0.06	2.38± 0.08	3.14	2.24±0.02
-550	4.31± 0.05	1.10± 0.08	2.88± 0.05	1.98± 0.06	2.25	2.05±0.02
-700	4.67± 0.06	1.13± 0.09	3.03± 0.05	1.85± 0.07	2.08	1.90±0.02

Fig. 3.7 shows the barrier layer thickness calculated from the EIS data as a function of applied potential, solution pH and concentration. The thickness of the barrier layer was directly proportional to the applied potential. Buffer concentration and pH did not have a significant effect on this correlation within the limits where these parameters were investigated. The slope of the lines in Fig. 3.7 was about 1.2±0.1 nm/V, which corresponds to the well-accepted literature data for the potential dependence of the thickness of the barrier layer formed on aluminium in aqueous media [10,44,45].

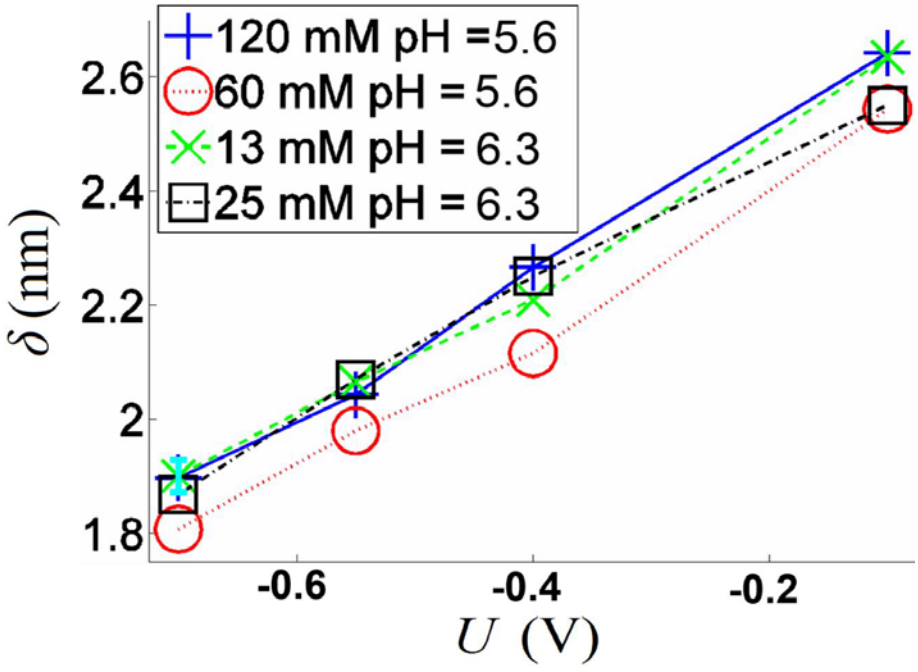

Figure 3.7 The thickness of the barrier layer obtained from EIS data vs. applied potential with the cyan vertical line representing the average standard deviation of all the data points.

3.4.2 VISSE

3.4.2.1 Short-time data

The short-time changes in the oxide thickness obtained by use of the barrier oxide model, after selected negative potential steps, are plotted in Fig. 3.8. A pseudo-steady state was obtained after each transient, at which a steady state barrier thickness was reached. The time needed to reach the pseudo-steady state increased with the size of the potential step. Fig. 3.8a and Fig. 3.8b show the changes in the thickness of the barrier layer after small voltage steps (-0.15 V). The thickness appears to reach steady state after less than 3 minutes. For the larger potential steps of -0.3 and -0.4 V, in Fig. 3.8c and Fig. 3.8d, respectively, the time elapsed to reach steady state becomes longer.

The barrier thickness reduction obtained from the negative potential steps corresponded to about 1.0 to 1.3 nm/V in agreement with the steady-state data obtained by EIS. The barrier thickness changes are presented as a function of time for two positive potential steps in Fig. 3.9. The dependence of the barrier layer thickness change on the applied potential steps obtained from these data is plotted in Fig. 3.10. Linear regression analysis of data for both positive and negative potentials steps revealed a barrier thickness-voltage ratio of 1.0 nm/V. For the negative steps only (Fig. 3.8), the result was 1.1 nm/V. Larger number of data points obtained for potential reduction steps gave statistically more reliable and accurate data for changes in the barrier layer thickness.

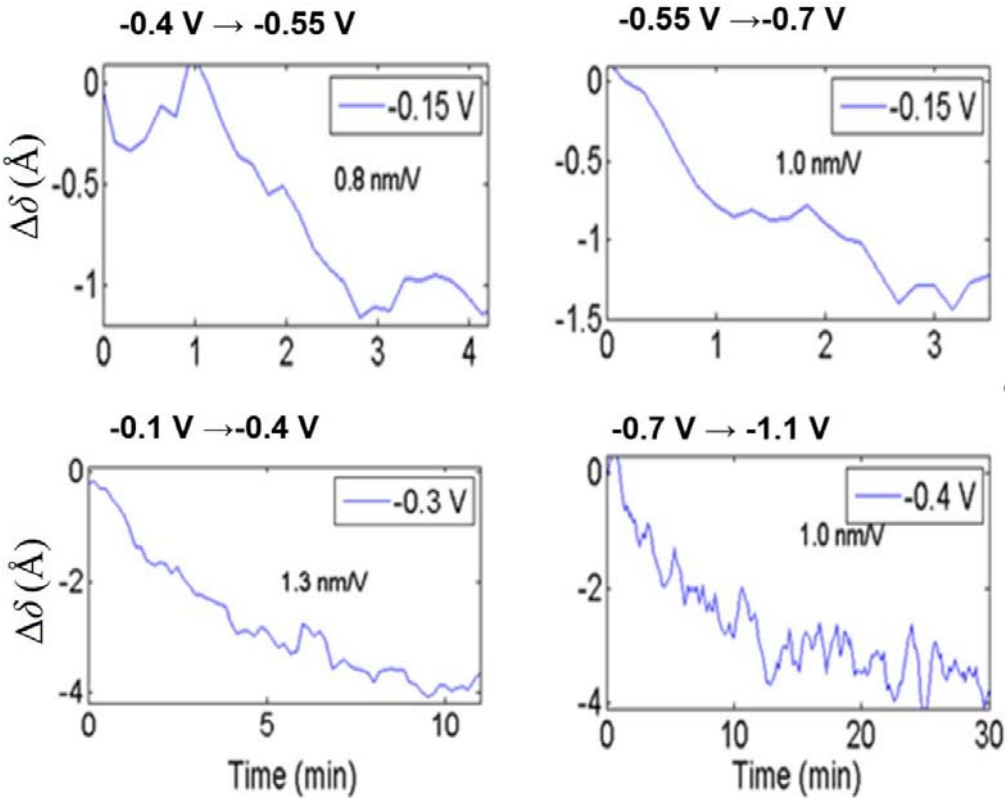

Figure 3.8 Change in barrier oxide thickness as a function of time just after negative potential step in 13 mM acetate buffer at pH = 6.3. Each potential step was applied at time normalised to zero. Thickness-voltage ratios averaged over the measurement interval are included in the figure. The size of the potential steps are shown in the boxes.

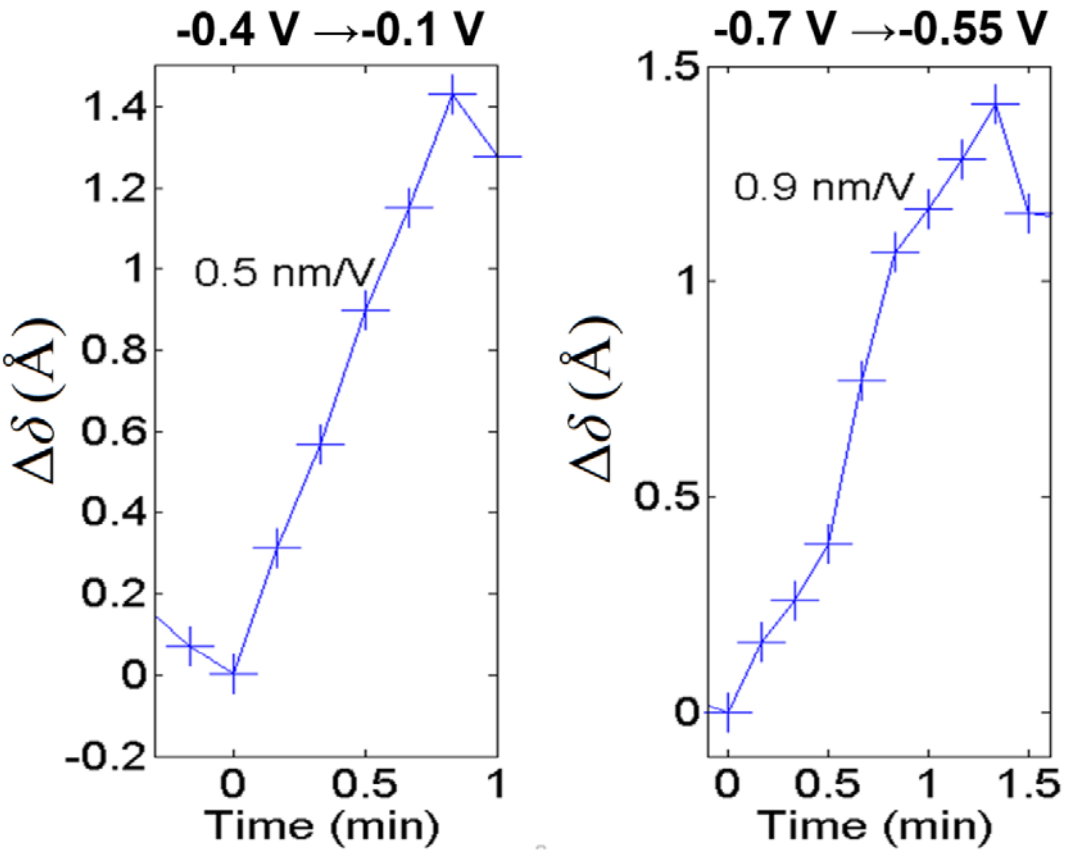

Figure 3.9 Change in the barrier and hydrated layer thicknesses as a function of time just after positive potential step in 13 mM acetate buffer at pH = 6.3. The potential was applied at time normalised to zero. Thickness-voltage ratios averaged over the measurement interval are included in the figure. The size of the potential steps are shown in the boxes.

Thickness changes caused by potential steps in the positive direction were considerably faster than the changes by negative steps. This resulted in fewer measured points and statistically insufficient data, resulting in a larger scatter in the calculated oxide thickness transients. The kinetics of barrier growth and dissolution based on the above results will be investigated further in Chapter 4.

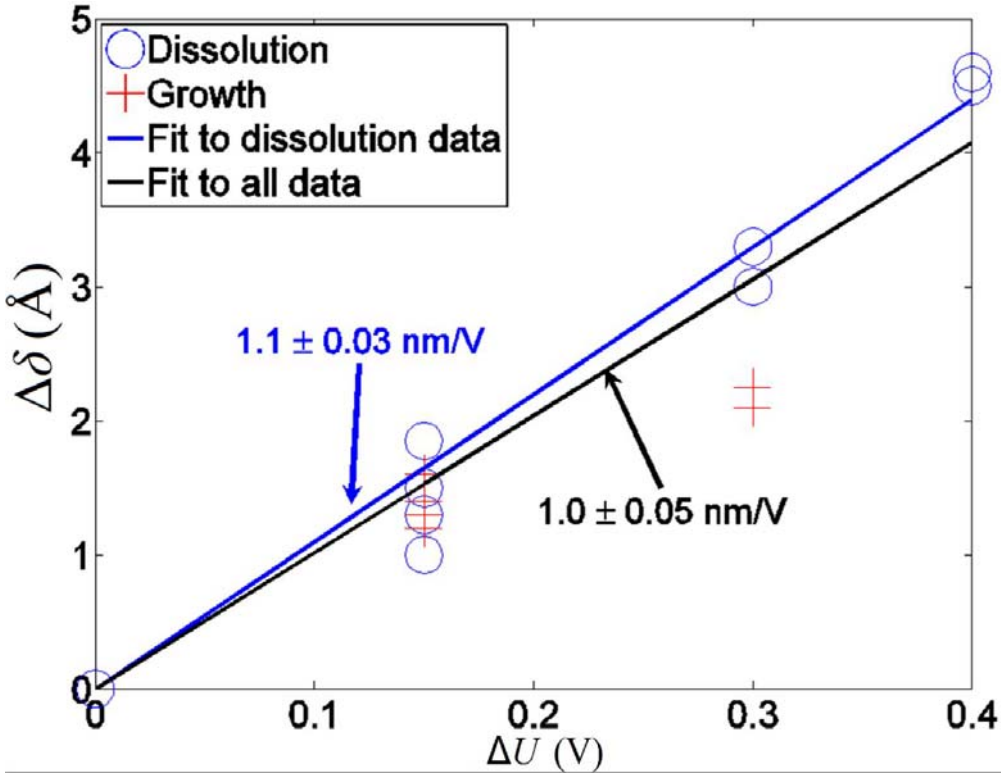

Figure 3.10 Change of barrier thickness as a function of applied potential steps, obtained by VISSE. Linear regression straight lines, fitted to all potential-step data and only to negative steps, are separately shown.

3.4.2.2 Long-time data

VISSE data measured over a longer period than the data discussed in the previous section, until steady state was obtained, are shown in Fig. 3.12, along with the applied potential sequence.

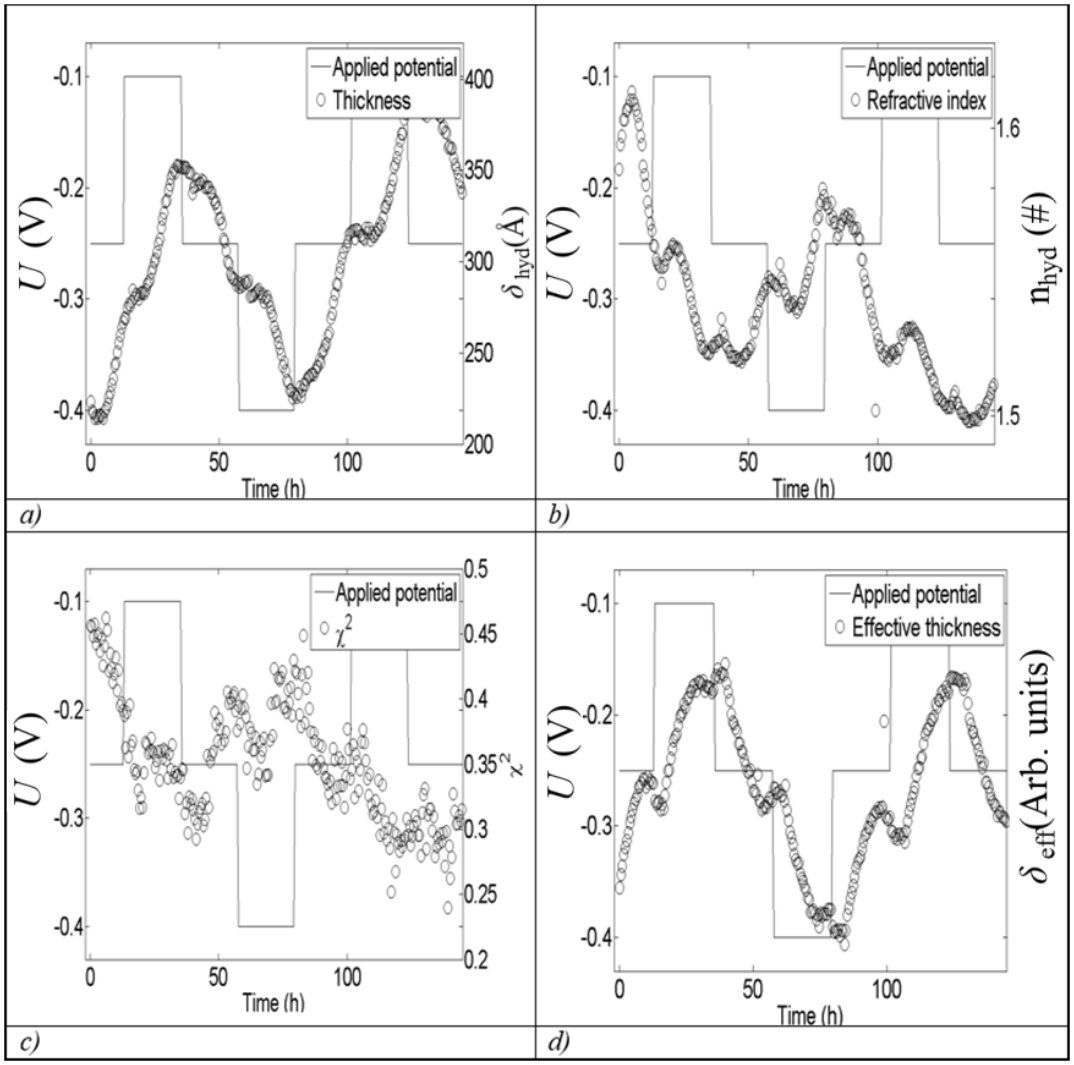

Figure 3.11 a) Actual thickness and b) refractive index of the hydrated oxide ,c) the curve-fitting parameter and d) the relative mass of aluminium oxide in the hydrated oxide layer (plotted as the effective mass thickness) plotted as a function of time as the potential was stepped through various values in 120 mM acetate buffer at pH = 5.6.

From these measurements, the thickness (Fig. 3.11a) and refractive index (Fig. 3.11b) of the hydrated layer was obtained as described in Section 3.2.3.2. The curve fitting parameter χ^2 is shown in Fig. 3.11c as a function of time and potential. The average χ^2 was 0.4±0.2. The average standard error for the fitted hydrated layer thickness was about 1%, while the error for the refractive index was even smaller. The amount of time needed to achieve the steady state hydrated layer thickness was about 12 hours. The thickness increased with increasing applied potential. The potential dependence of the steady-state thickness was not reversible. It appeared to increase with immersion time, as seen by comparing the steady-state thicknesses attained at a given potential in Fig. 3.11a. This is probably also related to the fact that a true steady state was not attained before the next potential step because of the long time needed for this, as explained above. The refractive

index, shown in Fig. 3.11b, decreased with increasing applied potential. In addition, the refractive index decreased slightly with immersion time at a given applied potential. The decrease in the refractive index occurred simultaneously with the increase in hydrated oxide thickness with immersion time at a given potential. The apparent irreversibility of the two parameters must be related to the same factors. However, the effective mass thickness δ_{eff} of the hydrated layer, plotted in Fig. 3.11d, depended reversibly on increasing potential, *i.e.*, no shift was observed with increasing submersion time. These results indicate that the applied potential controls the total mass per area of the aluminium oxide (in the form Al_2O_3 without the water) formed. However, hydration (and/or porosity) of the oxide increases as a function of immersion time independent of the potential. This causes an inversely proportional decrease in the refractive index, leaving δ_{eff} constant and reversible at a given applied potential.

3.4.3 TEM

As described in Section 3.3 the TEM samples were prepared after the samples were removed from the solution, rinsed and dried. Fig. 3.12 shows a typical cross-sectional image of the composite oxide consisting of the dense barrier and porous hydrated layers. The black area on the left side is the aluminium metal. The grey film adjacent to the metal and the protruding fibres with the same grey tone to the right are the barrier and fibrillar hydrated layers, respectively. The space between the fibres is filled with epoxy, which appears in a lighter grey tone than that of the oxide. Thicknesses corresponding to a few stabilisation potentials were determined by tracing the grey-scale level for the oxide, as explained in Section 3.3 and Fig. 3.12. The change in the averaged grey scale level for the typical cross section shown in Fig. 3.12 is plotted in Fig. 3.13. The thicknesses obtained from such analyses are plotted as a function of stabilization potential in Fig. 3.14. The thickness of the barrier layer varied in direct proportion to the applied potential. However, the slope of 3.4 nm/V was high compared to the expected value of about 1.2 nm/V. This may be a result of oxidation during the period the samples were exposed to ambient air. A similar difference between *in situ* and *ex situ* measurements was earlier observed by ellipsometry [8]. Similarly, the hydrated oxide layer was probably affected by exposure to ambient air and sample preparation. Still, the approximate thickness of the hydrated layer increased with applied potential.

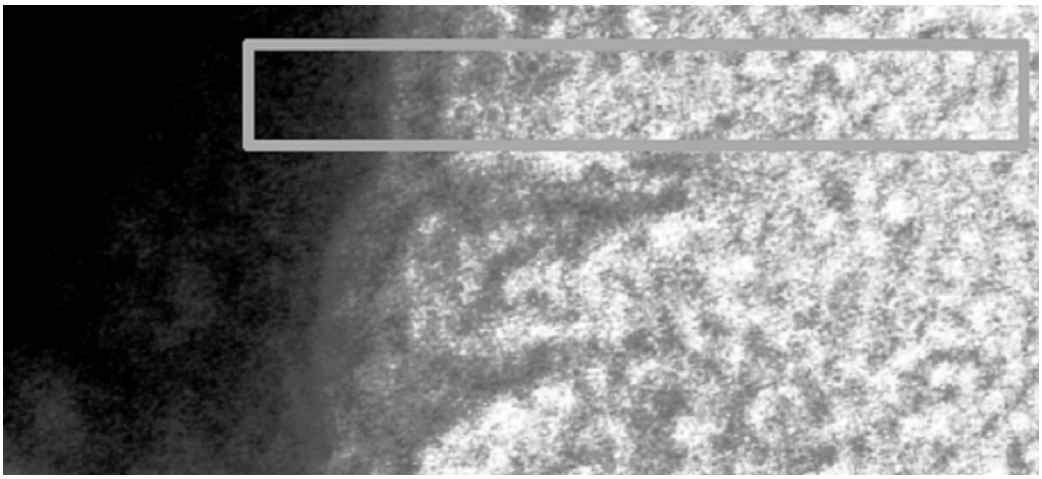

Figure 3.12 TEM cross-sectional image of oxide morphology on sample prepared at -0.7 V vs. Hg/Hg_2SO_4 in 48 mM acetate buffer at pH=5.6. The region of data analysis is marked by the frame. The grey scale for each horizontal position in the frame was averaged by integrating the grey-scale intensity in the vertical direction.

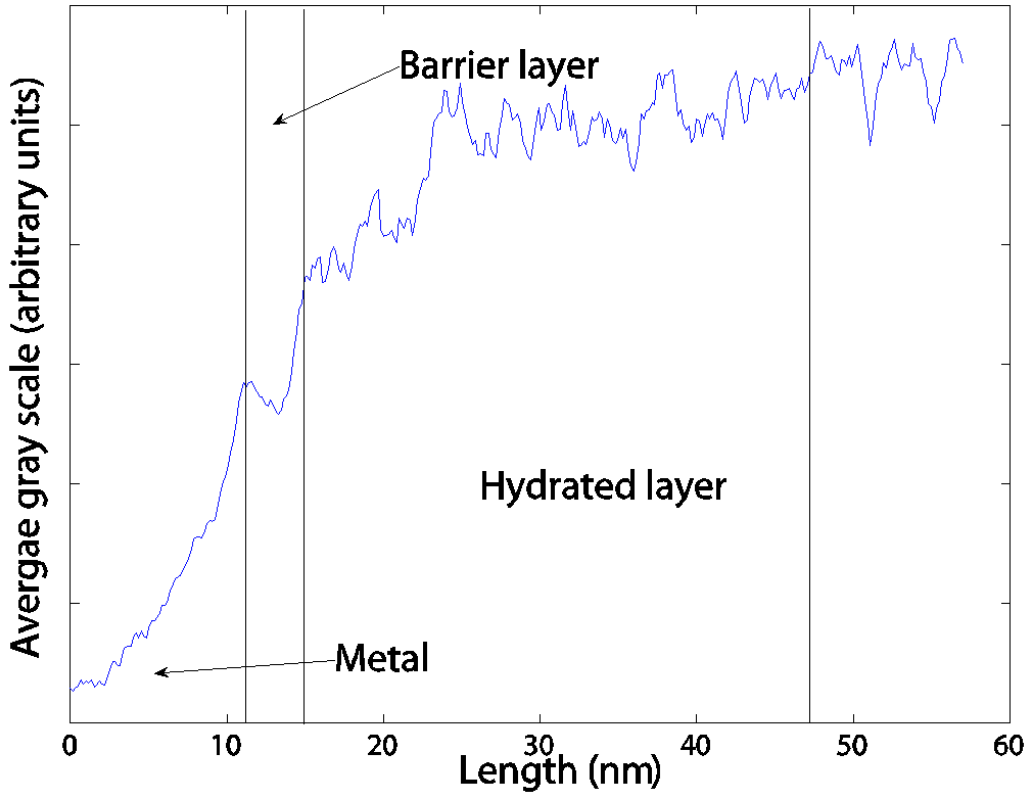

Figure 3.13 Variation of the averaged grey scale calculated from Fig. 3.12 as a function of distance from the metal surface.

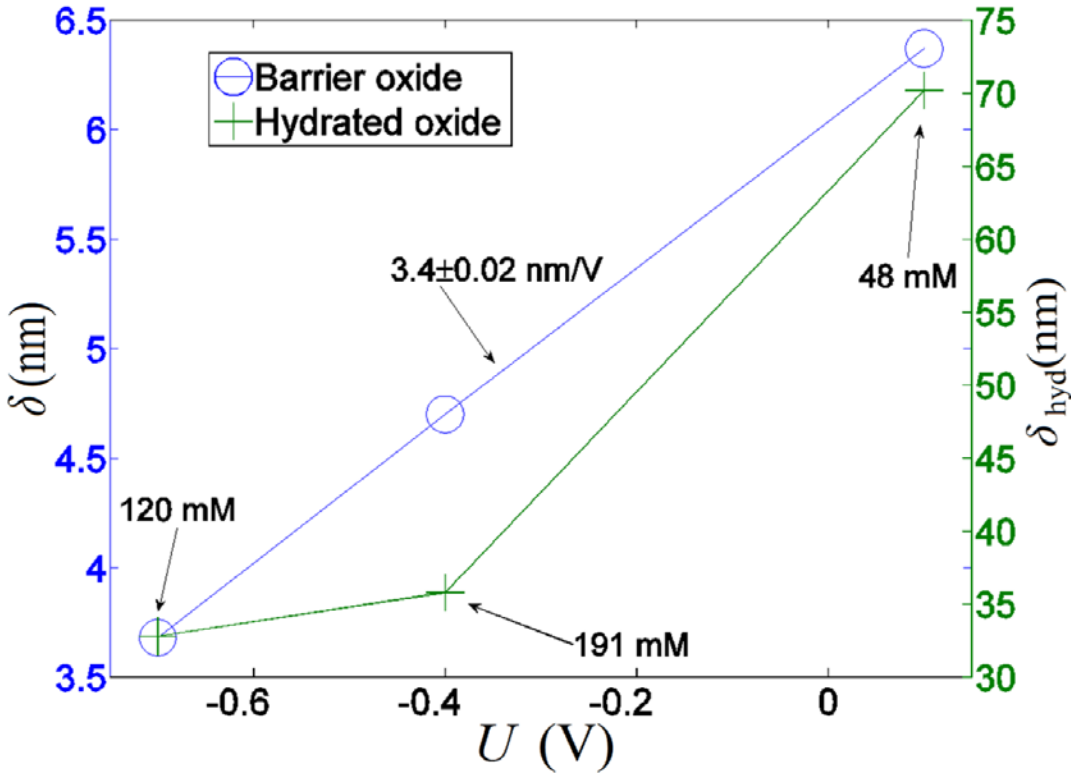

Figure 3.14 Thicknesses obtained from the TEM cross-sectional images based on the type of analysis shown in Fig. 3.13. The oxide was grown at various buffer concentrations indicated in the figure. The pH was constant at 5.6.

3.5 Discussion

The methodology developed, combining EIS and *in situ* VISSE, for characterising the oxide film properties under well-defined conditions, was validated by the steady-state and transient relaxation results from the respective techniques that both revealed the well-accepted thickness-voltage relationship for the barrier layer. The growth rates of the barrier and hydrated oxides were then made possible by simultaneous use of the two techniques.

An important aspect of the proposed methodology is the separation of the barrier and hydrated layer properties with certain limitations. This approach involved the assumption that the thickness change of the hydrated oxide layer is very small compared to the rapid change of the barrier layer thickness for a short time period soon after the potential step. This assumption allowed the determination of the thickness change of the barrier layer following a potential step by assuming a constant thickness of the hydrated oxide. The approach worked especially well for film thinning where the thickness followed the well-accepted thickness-voltage relationship. For film growth, the total thickness change occurred in less than a minute but with a thickness-voltage ratio lower than expected. However, the EIS measurements showed that the barrier thickness is directly proportional to the applied potential independent of the direction and magnitude of the potential step used in the experiment. Therefore, the film-growth data were probably affected by limitations in the measurement equipment, which allowed about one measurement every ten seconds. The lower

thickness-voltage ratio may be related also to any growth of the hydrated oxide layer, which was assumed constant. According to the high field model of metal oxidation, a high growth rate is expected when the applied potential is increased [2,46]. The present method can be improved by use of a faster data-logging approach, such as the use of current density transients (Chapter 4) or even faster single wavelength ellipsometric acquisition.

In the other extreme of long-time response, the barrier layer thickness was assumed to remain constant in determining the thickness of the hydrated layer. This assumption worked well since the barrier layer thickness stabilized rapidly after the potential step, and allowed the determination of the hydrated oxide thickness and refractive index following positive and negative potential steps. These parameters proved to be dependent also on the time of immersion in the test solution, attributed to increasing hydration with immersion time. As a result, it was not possible to use the time needed for the hydrated film thickness to reach steady state. However, the effective mass thickness of the hydrated layer reached a steady state, and its steady state was shown to be reversibly determined by the applied potential, independent of the immersion time. The hydrated layer is formed by a chemical process, related to the dissolution and redeposition of aluminium ions. However, the flux of Al^{3+}, which is determined by the oxidation rate of the aluminium metal and the dissolution rate of the barrier oxide film according to the present model, are potential dependent processes. Hence, the concentration of Al^{3+} ions available for the formation of the hydrated layer is potential dependent, and the steady state effective mass thickness is therefore expected to be dependent reversibly on the applied potential.

Foregoing discussion on the properties of the hydrated layer is based on data obtained under nearly stagnant conditions on the surface. An important parameter, not investigated presently, was the effect of stirring conditions, which appeared to be important for the properties of the hydrated layer.

3.6 Conclusions

Transient VISSE methodology is developed, in combination with steady-state EIS for calibration purposes, to monitor the thickness of very thin oxides *in situ*. The methodology provided new insight into the growth and dissolution of very thin barrier and hydrated oxide layers. The asymptotic approach of assuming constant hydrated film properties during the short-time response of the ellipsometric parameters to a potential step, in determining the barrier film properties, and the assumption of constant barrier film properties for the long-time response to determine the hydrated film properties gave satisfactory results. There is a need to improve the short-time acquisition of ellipsometric data.

The growth and dissolution rates of the barrier layer appeared to be governed by different kinetics, characterized by a faster growth rate and a slower dissolution rate, which deserves further investigation. Well-known thickness-voltage ratio of 1.2 nm/V was verified for steady-state thickness of the barrier oxide under the conditions investigated, which also validated the present methodology.

The actual thickness of the hydrated oxide, dependent on the morphology and hydration of the hydrated oxide, was not reversible or reproducible because of continuous hydration as a function of the immersion time. However, the steady state effective mass thickness of hydrated oxide was shown to be reversibly determined by the applied potential.

3.7 References

[1] Macdonald, D. and Urquidi-Macdonald, M. *J. Electrochem. Soc.* **137**, 2395 (1990).

[2] Vetter, K. J. *Electrochim. Acta* **16**, 1923 (1971).

[3] de Wit, J. and Lenderink, H. *Electrochim. Acta* **41**, 1111-1119 (1996).

[4] Hurlen, T., Lian, H., Ødegård, O., and Våland, T. *Electrochim. Acta.* **29**, 579-585 (1984).

[5] Alexander, M. R., Thompson, G. E., and Beamson, G. *In 'Aluminium Surface Science and Technology 2000', ATB Metallurgie, Brussels: Manchester, UK,* 133-138 (2001).

[6] O'Sullivan, J. P. and Wood, G. C. *Proc. R. Soc. London, Ser. A* **317**, 511-543 (1970).

[7] Habazaki, H., Shimuzu, K., Skeldon, P., Thompson, G. E., and Wood, G. *Thin Solid Films* **300**, 131 (1997).

[8] R. Kötz, Schnyder, B., and C.Barbero. *Thin Solid Films* , 63 (1993).

[9] Greef, B. and Norman, C. *J. Electrochem. Soc.* **132**, 2362 (1985).

[10] Thompson, G. E. *Thin Solid Films* **297**, 192 (1997).

[11] Verwey, E. J. W. *Z. Kristallogr.(A)* **91**, 315 (1935).

[12] Cabrera, N. and Mott, N. F. *Rep. Prog. Phys.* **12**, 163 (1948-1949).

[13] Guntherschulze, A. and Betz, H. *Z. Phys.* **92**, 367 (1934).

[14] Bessone, J., Mayer, C., Jüttner, K., and Lorenz, W. J. *Electrochim. Acta* **28**, 171-175 (1983).

[15] Gudic, S., Radosevic, S., and Kliskic, M. *J. Appl. electrochem.* **26**, 1027-1035 (1996).

[16] Bessone, J., Salinas, D., Mayer, C., Ebert, M., and Lorenz, W. *Electrochim. Acta* **37**, 2283-2290 (1992).

[17] Moon, S.-M. and Pyun, S.-I. *Electrochim. Acta* **43**, 3117-3126 (1998).

[18] Betova, I., Bojinov, M., Kinnunen, P., Laitinen, T., Pohjanne, P., and Saario, T. *Electrochim. Acta* **47**, 2093-2107 (2002).

[19] Jüttner, K., Lorenz, W. J., and Paatsch, W. *Corros. Sci.* **29**, 279-288 (1989).

[20] Darowicki, K., Krakowiak, S., and Slepski, P. *Electrochim. Acta* **49**, 2909-2918 (2004).

[21] Stein, N., Rommelfangen, M., Hody, V., Johann, L., and Lecuire, J. *Electrochim. Acta* **47**, 1811-1817 (2002).

[22] Gils, S. V., Melendres, C., Terryn, H., and Stijns, E. *Thin Solid Films* **455-456**, 742-746 (2004).

[23] Greef, R. *Thin Solid Films* **233**, 32-39 (1993).

[24] Gils, S. V., Melendres, C., and Terryn, H. *Surf. Interface. Anal.* **35**, 387-394 (2003).

[25] Armstrong, R. D. and Edmondson, K. *Electrochim. Acta* **18**, 937 (1973).

[26] Lohrengel, M. M. *Mater. Sci. Eng.* **R 11**, 243 (1993).

[27] Macdonald, D. D., Rifaie, M. A., and Engelhardt, G. R. *J. Electrochem. Soc.* **148**, B343-B347 (2001).

[28] Diggle, J. W., Downie, T. C., and Goulding, C. W. *J. Electrochem. Soc.* **116**, 737 (1969).

[29] Xu, Y. PhD thesis, University of Manchester, Manchester, UK(1983).

[30] Siejka, J. and Ortega, C. *J. Electrochem. Soc.* **124**, 883-891 (1977).

[31] Våland, T. *The behaviour of Al electrodes in aqueous solutions*. PhD thesis, Forsvarets Forskingsinstitutt, Kjeller, Norway (1981).

[32] Nordlien, J. H. *Naturally formed oxide film on magnesium and magnesium alloys*. PhD thesis, Norwegian Institute of technology, Trondheim, Norway (1995).

[33] Holub, K., Tessori, G., and Delahay, P. *J. Phys. Chem.* **71**, 2612 (1967).

[34] Frers, S. E., Stefenel, M. M., Mayer, C., Chierchie, T., and Radosevic, S. *J. Appl. Electrochem.* **20**, 996-999 (1990).

[35] Vermilyea, D. A. *J. Electrochem. Soc.* **104**, 427 (1957).

[36] Young, L. *Anodic Oxide Films*. Academic Press, New York, USA (1961).

[37] Franquet, A., Terryn, H., and Vereecken, J. *Appl. Surf. Sci.* **211**, 259-269 (2003).

[38] Tompkins, H. G. and McGahan, W. A. *Spectroscopic Ellipsometry and Reflectometry*. Wiley, Ontario, Canada (1999).

[39] Azzam, R. and Bashara, N. 529. North Holland, Amsterdam (1989).

[40] Palik, E. *Handbook of Optical Constants of Solids*, 397-399. Academic Press, Boston, USA (1998).

[41] Palik, E. *Handbook of Optical Constants of Solids II*, 769-770. Academic Press, Boston, USA (1998).

[42] Bruggemann, D. *Anal. Phys.* **5**, 638 (1935).

[43] Sævik, Ø. *Effect of Trace Element Lead on the Electrochemistry and Corrosion of Aluminium Alloys*. PhD thesis, Norwegian University of Science and Technology, Trondheim, Norway (2005).

[44] Hass, G. *J. Opt. Soc. Amer.* **39**, 532 (1949).

[45] Deryagin, B. V. and Friedland, R. M. *Z. tech. Phys. U.S.S.R* **18**, 1443 (1948).

[46] Verwey, E. J. W. *Physica(A)* **2**, 1059 (1935).

4 Simultaneous ellipsometric and potentiostatic study of aluminium oxide growth and dissolution in acetate buffer.

Abstract

In situ ellipsometric and chronoamperometric measurements were applied simultaneously to monitor barrier oxide growth and dissolution on aluminium. The steady-state thickness prior to each potential-step was determined by electrochemical impedance spectroscopy (EIS) for calibration of the transient data. The growth of the barrier-oxide, following a positive potential step, was consistent with the Cabrera-Mott inverse square logarithmic growth. About 20% of the measured current resulted in barrier oxide growth. The oxide dissolution rate, following a negative potential step, was controlled by diffusion of aluminium ions into the test solution. The obtained dissolution rate was thus much smaller than the corresponding oxide growth rates. Oxide solubilities calculated from Fick's second law, by using literature data for the diffusion coefficient of Al^{3+}, were about an order of magnitude larger than that obtainable from thermodynamic considerations. The methodology developed in Chapter 3 was successfully applied in improving the existing know-how about the growth and dissolution of the barrier oxide layer in aqueous solution.

4.1 Introduction

In the previous chapter, we combined EIS and VISSE to investigate *in situ* the properties of the composite oxide, consisting of a thin barrier layer and a fibrillar-hydrated layer, which was formed on aluminium under potentiostatic conditions in a slightly acidic acetate buffer solution. That chapter focused on developing and validating the VISSE methodology to estimate thickness of the barrier and hydrated layers of the composite oxide during its growth and dissolution in response to applied potentiostatic steps. EIS was used to measure the steady-state thickness of the barrier layer with the purpose of calibrating the transient thickness measurements obtained by VISSE. The purpose of this chapter is to analyse the VISSE measurements further, together with current transients obtained in response to each potential step, to investigate the kinetics of oxide growth and dissolution.

4.2 Literature survey

Based on early electrochemical investigations of oxide growth kinetics [1-3], high field growth mechanism of oxide on aluminium in aqueous solution has been well established. More recently, potentiostatic measurements (chronoamperometry) of oxide growth on pure Al, studied in borate [4] and citric acid [5] solutions were successfully fitted to Eq. (2-5). However, experimental verification of Cabrera-Mott kinetics for growth of thin aluminium oxide films in aqueous solution by a more direct thickness monitoring method is not available. One of the main reasons for this seems to be the lack of methodology that can provide accurate measurement of duplex oxide layers in aqueous solution. Verification of the growth kinetics and validation of the indirect chronoamperometry by accurate thickness monitoring with good time resolution is desirable. Available ellipsometry data to track oxide thickness in situ lack either adequate time resolution [6] (10 min between every time step) or adequate spectral resolution to ensure observation of a duplex oxide structure [7]. In quartz microbalance experiments, growth of barrier and hydrated oxides could not be distinguished from one another [8].

The available data on the dissolution kinetics of the barrier oxide in aqueous solution are scarce and contradictory about the mechanism. A chemically governed dissolution was suggested also by work on corrosion of Al alloys in flowing seawater [9]. The study showed that dissolution rates were mass-transfer controlled and unaffected by application of cathodic potentials. Other studies pertain to high voltage anodizing in strongly acidic media in studies of porous oxide growth. As observed by *in situ* ellipsometry, the thickness of barrier oxide at open-circuit conditions in 2 M phosphoric acid [10] and 0.1 M hydrochloric acid decreased in direct proportion to the immersion time during an extended period of 2 hours. The mechanism of dissolution was proposed to be chemical without much explanation. The observed variation of open-circuit potential (OCP) in the cathodic direction during dissolution was explained in terms of reduction in oxide thickness. In another study [11], samples were first anodized at constant potential (115 V) in 0.4 M H_3PO_4 solution. The applied potential was subsequently reduced in steps in the anodising solution, starting from the initial value of 115 V and followed by successive steps to 95 V, 85 V and 75 V. The samples were removed from the cell at predetermined times during the dissolution process at each step. The oxide was investigated subsequently by *ex situ* transmission electron microscope (TEM) analysis. The average dissolution rate at each step was estimated from the initial and final thickness of the barrier layer at each step. The dissolution rate was reported to decrease with the potential at each step. Another study [12] based on H_2SO_4-anodised samples reported barrier-layer dissolution rates based on impedance measurements following decreasing potential stepping as above. The barrier-layer dissolution rate decreased with increased potential step size. These results were interpreted to indicate field assisted dissolution. In addition to the type of errors, which can be introduced by *ex situ* measurement, as discussed in Chapter 3, the highly acidic solutions used and the high potentials applied may have specific effects on the reported barrier-layer properties, in relation to the low potential, higher pH solutions used in the present work. Moreover, the reported potential step dependence can be explained by other mechanisms, as will be shown later in this chapter.

It can be concluded from this literature study that the growth and dissolution kinetics of barrier layer oxide on aluminium in aqueous solution is not clarified. An *in situ* investigation of these processes by multi-wavelength ellipsometry combined with simultaneous chronoamperometric measurements to clarify the mechanisms is therefore justified.

4.3 Experimental

The ellipsometric and electrochemical data used in this chapter were presented in Chapter 3, and the experimental details are reported in Section 3.3. The short-time transient parts of these data are analysed further in this chapter. The potential was stepped not long after the rapid barrier thickness growth stopped, to avoid formation of thick hydrated oxide layers that would make the analysis of ellipsometry data difficult. For large negative potential steps, it took up to half an hour to reach steady state. Although the ellipsometry data attained steady state within this period, this was not the case for all current-density transients. Solution descriptions are presented in Table 4.1.

Table 4.1 Properties of the solutions used in the experimental measurements. The pH values were calculated from the solution compositions.

pH	[HAc] (mM)	[NaAc] (g/L)	[HAc] g/L
5.6	119	68.0	7.16
5.6	60	34.0	3.58
6.2	25	64.4	1.52
6.2	13	32.2	0.762

The potentials reported in this chapter refer to a saturated Hg/Hg_2SO_4 reference electrode. Initially, the surface was stabilised at -700 mV. The potential was then stepped in the order -700, -550, -400, -100, -400, -550, -700, -1100, -700, -550, -400, -100, -400, -550, -700 and -1100 mV.

4.4 Results

4.4.1 Transient behaviour during oxide growth

Fig 4.1a and Fig. 4.1b show the changes in the barrier oxide thickness, measured by ellipsometry, and the corresponding current density, respectively, as a function of time following the specified positive potential steps in the potential range -1.1 to -0.1 V, in 13 mM acetate buffer solution. Fig. 4.2a and Fig. 4.2b show the corresponding data in 25 mM acetate buffer. For both buffer concentrations the ellipsometry results indicate that a steady-state barrier thickness was attained within 70 s. Oxide growth occurred at thickness-voltage ratios in the range 1.0-0.7 nm/V, lower than the well-accepted value 1.2 nm/V [13-15], with the lowest ratios obtained for the largest potential steps. The film-growth data were probably affected by limitations in the measurement method, which allowed about one measurement every ten seconds, with the barrier thicknesses obtained as an average thickness for this period. The lower thickness-voltage ratio may also be related to any growth of the hydrated oxide layer (assumed constant thickness) occurring during the measurement period. Possible sources of error in the ellipsometry data were discussed in more detail in Chapter 3 with reference to the relevant literature.

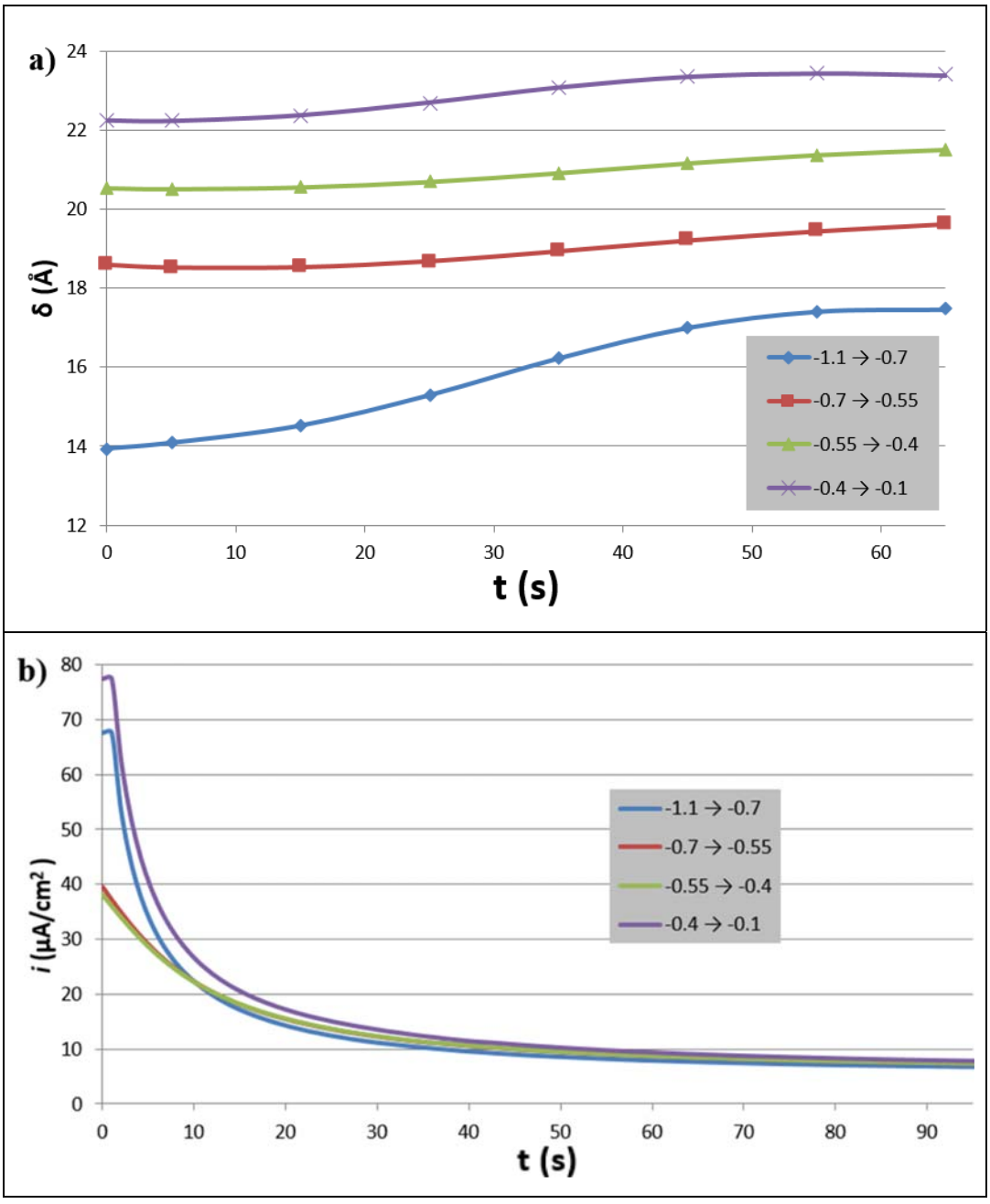

Figure 4.1 Changes in (a) barrier oxide thickness and (b) current density as a function of time, following successive positive potential steps in the range -1.1 to -0.1 V in 13 mM acetate buffer at pH = 6.

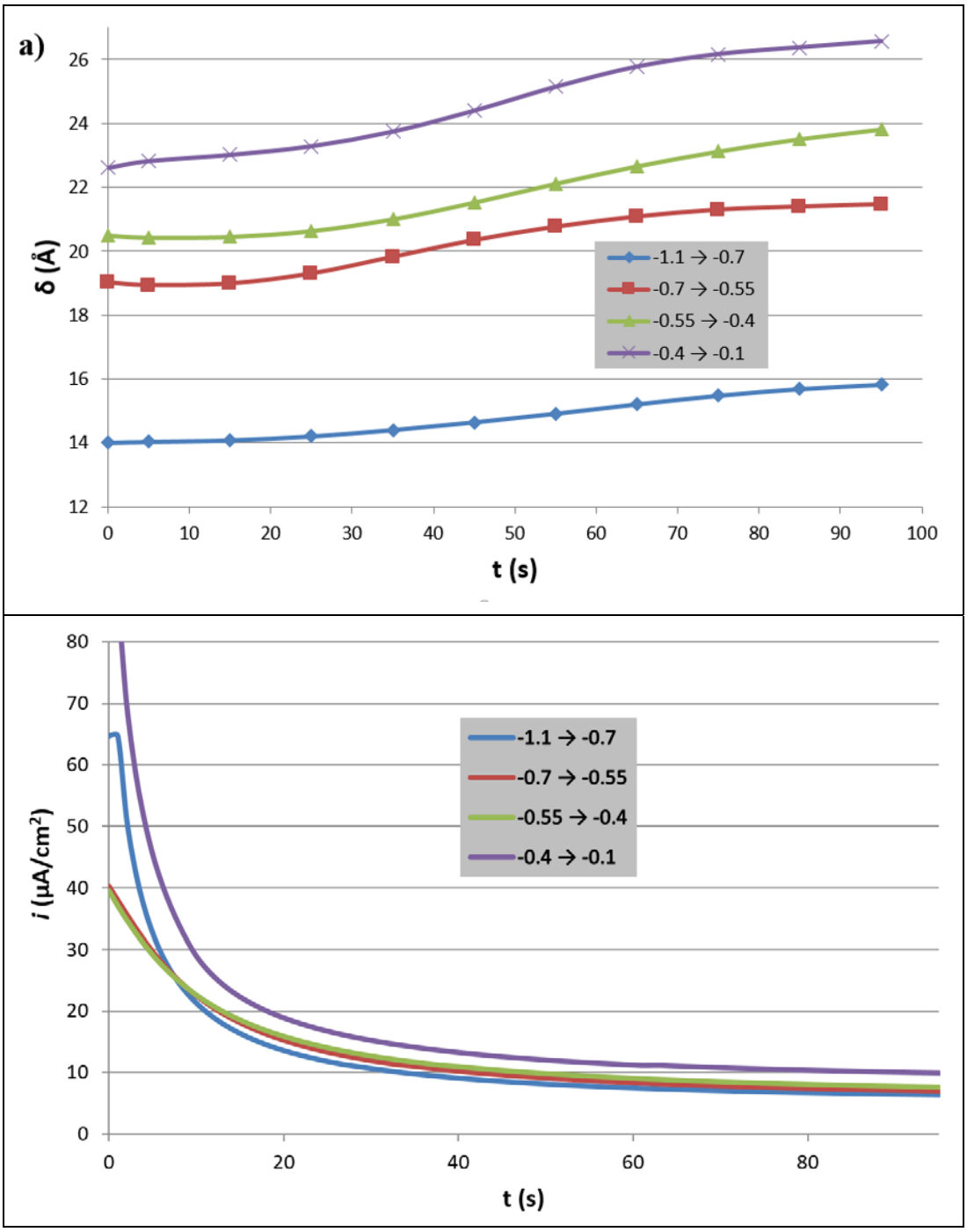

Figure 4.2 Changes in (a) barrier oxide thickness and (b) current density as a function of time, following successive positive potential steps in the range -1.1 to -0.1 V in 25 mM acetate buffer at pH = 6.

The current transients corresponding to the potential steps of the same magnitude exhibited similar trends with respect to one another, although the initial current densities were different, as can be seen in Fig 4.1b and Fig. 4.2b. Thus, the current densities corresponding to a potential step of +0.4 V decayed from initial values in the range 70-80 μA/cm^2 to values in the range 8-9 μA/cm^2 in about 1 min due to growth of the barrier layer. Current densities corresponding to a potential step of +0.15 V decayed from initial values of about 40 μA/cm^2 to the same level as above within the same period. By comparing the amount of charge passed, obtained by integrating the current density-time curves in Fig 4.1b and Fig. 4.2b (the first 80 seconds), and the actual change in the oxide thickness obtained by EIS in Chapter 3 (1.2 nm/V), the percentage of the current used to produce the barrier oxide was calculated to be about 20%, in agreement with the results of Gudic et al. obtained in the pH range 6.8 to 9.25 [16].

In order to determine the kinetics of barrier oxide growth, the ellipsometric data were analysed by use of the Cabrera-Mott inverse square logarithmic growth law as expressed in the form (see Section 2.1.2)

$$\frac{\delta_1}{\delta} = -\ln\frac{(t+\tau)}{\delta^2} - \ln(\delta_1 u) \qquad \textbf{(4-1)}$$

A plot of the inverse oxide thickness δ as a function of $\ln(\frac{t}{\delta^2})$ should give a straight line if the growth rate is consistent with Eq. (4-1). Fig. 4.3 and Fig. 4.4 show the inverse barrier oxide thickness in 13 and 25 mM HAc buffer solution, respectively, following positive potential steps, as a function of $\log\left(\frac{t}{\delta^2}\right)$. Since ellipsometry data provided only relative changes in the film thickness, the absolute initial δ values before each potential were based on the steady-state impedance measurements, as reported in Chapter 3, except for the thickness at -1.1 V. The steady-state thickness for this potential was calculated from the direct proportionality 1.2 nm/V between the thickness and applied potential. The correlations for all potential steps in Fig. 4.3 and Fig. 4.4 appear to be consistent with the inverse square logarithmic growth law with slopes in the range -0.0024 to -0.0077 Å^{-1}.

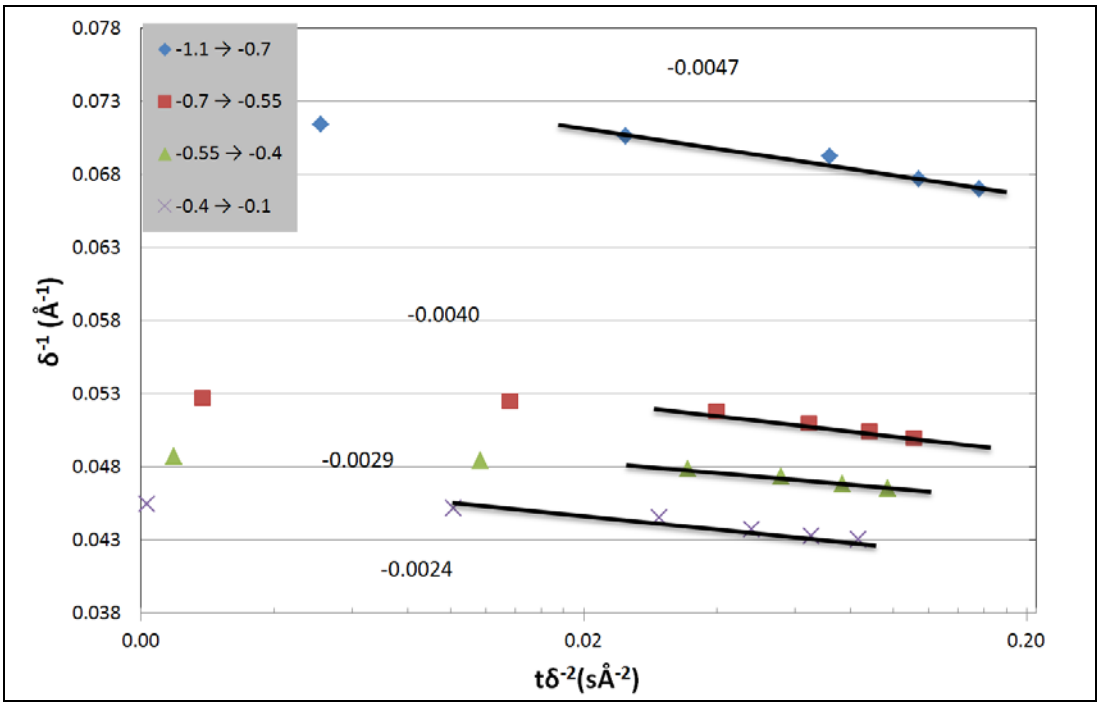

Figure 4.3 Inverse thickness, based on ellipsometry data, as a function of log (t/δ^2) for the successive potential steps indicated in the figure legend, in 13 mM acetic acid buffer solution at pH = 6. The slopes of the straight lines fitted to the data are indicated on the figure.

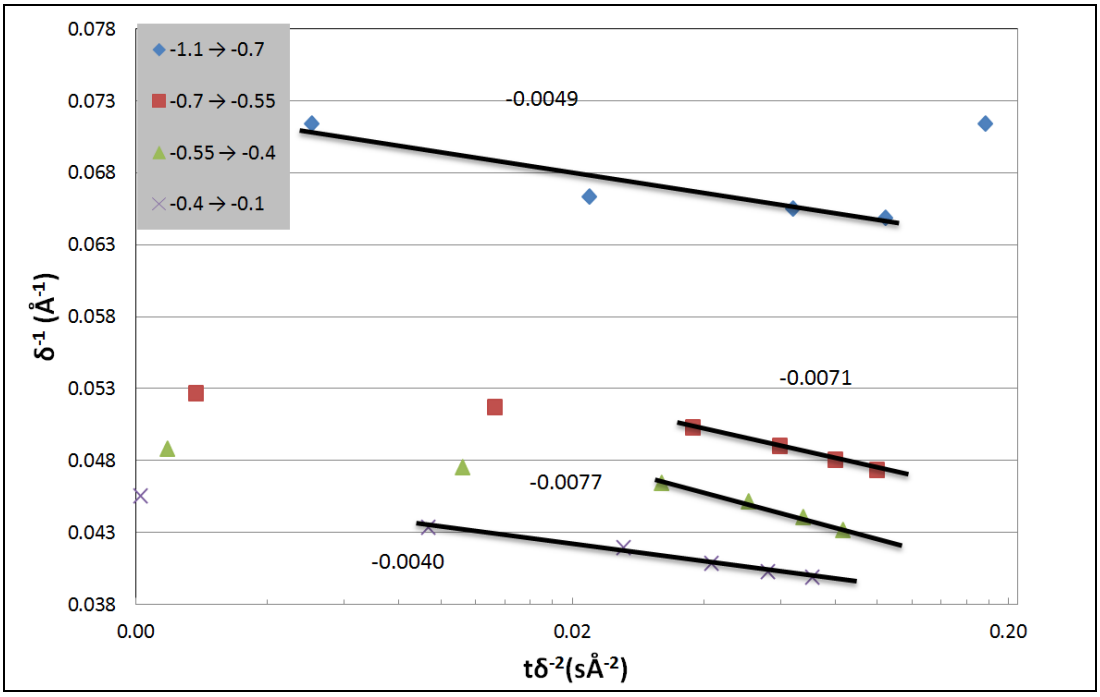

Figure 4.4 Inverse thickness, based on ellipsometry data, as a function of log (t/δ2) for the successive potential steps indicated in the figure legend, in 25 mM acetic acid buffer solution at pH = 6. The slopes of the straight lines fitted to the data are indicated on the figure.

An attempt was made to use the current density data to estimate film growth rates by use of the relationship (Faraday's law)

$$\Delta\delta(t) = \frac{M_n}{\rho z \mathrm{F}} \int_o^t (i(t) - i_{ss}) dt \qquad \textbf{(4-2)}$$

where t is the time elapsed after the potential step, $i(t)$ is the measured current as a function of time, M_n is the molecular weight of the barrier oxide (0.102 kg/mol), ρ is the density of the oxide ($3.25 \cdot 10^3$ kg/m^3), z is the number of electrons transferred during oxidation of aluminium (= 6 per mole of Al_2O_3 formed), and F is Faraday's constant. In performing the integration, the leakage current density i_{ss}, was assumed constant and equal to the quasi steady-state current density attained after 50 s at the applied potential, which is when the steady state barrier oxide thickness was assumed to be attained. Fig. 4.5 shows the correlation of the film thickness according to Eq. (4-1), calculated from the current measurement in response to the potential steps indicated in the legend in 13 mM acetate buffer at pH = 6. Fig. 4.6 and Fig. 4.7 show correlation of the film thickness according to Eq. (4-1), calculated from the current measurement in response to the potential steps indicated in the legend in 25 mM acetate buffer at pH = 6, for two replicate measurements. The initial thicknesses for each potential step was again obtained from the EIS data, as described above. Excess film thickening at larger times than 50 s, probably related to growth of the hydrated layer, prevented the use of the analysis techniques above, which are limited to barrier-layer growth by

virtue of the assumptions involved.

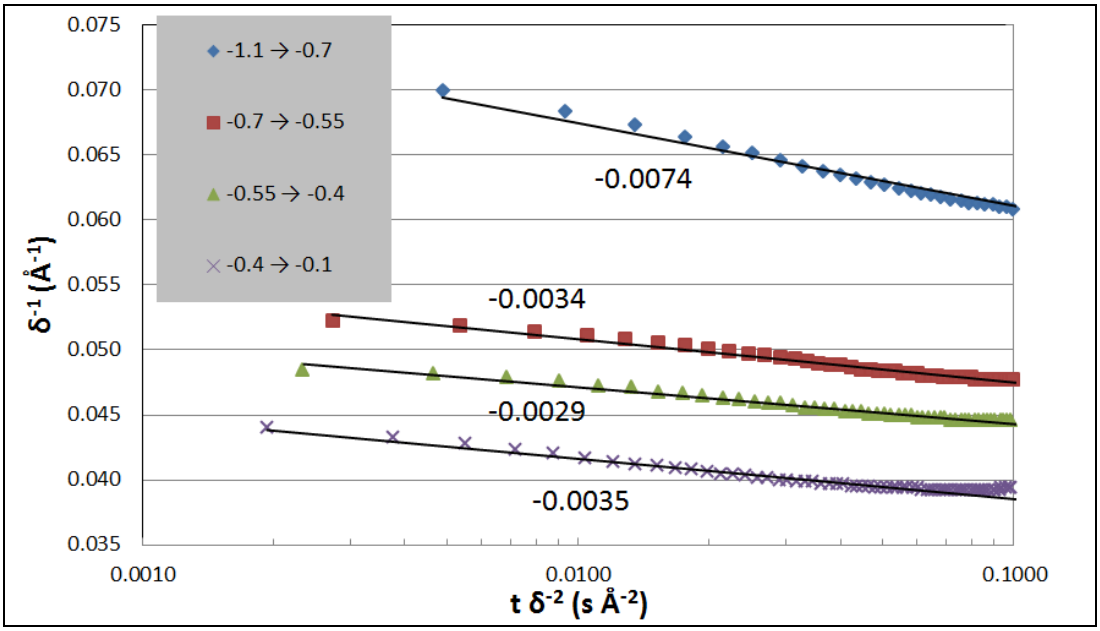

Figure 4.5 Inverse thickness, calculated from current transients, as a function of log (t/δ2) corresponding to successive positive potential steps specified in the legend, in 13 mM acetate buffer at pH = 6. The numbers indicate the slopes of the straight-line fits in $Å^{-1}$.

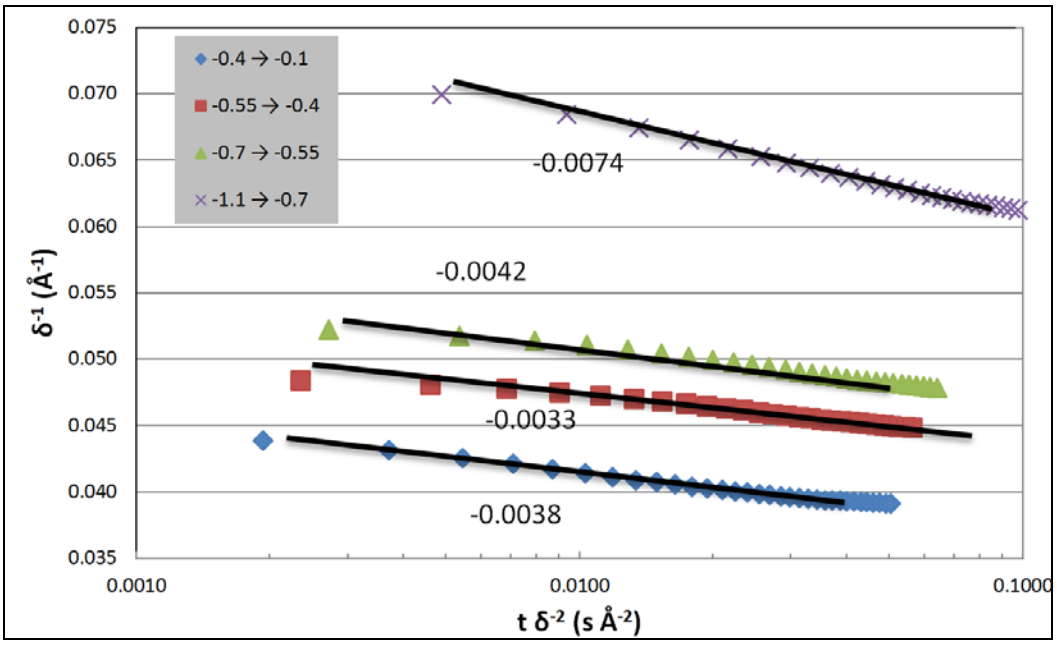

Figure 4.6 Inverse thickness, calculated from current transients, as a function of log (t/δ^2) corresponding to successive positive potential steps specified in the legend, in 25 mM acetate buffer at pH = 6. The numbers indicate the slopes of the straight-line fits in $Å^{-1}$.

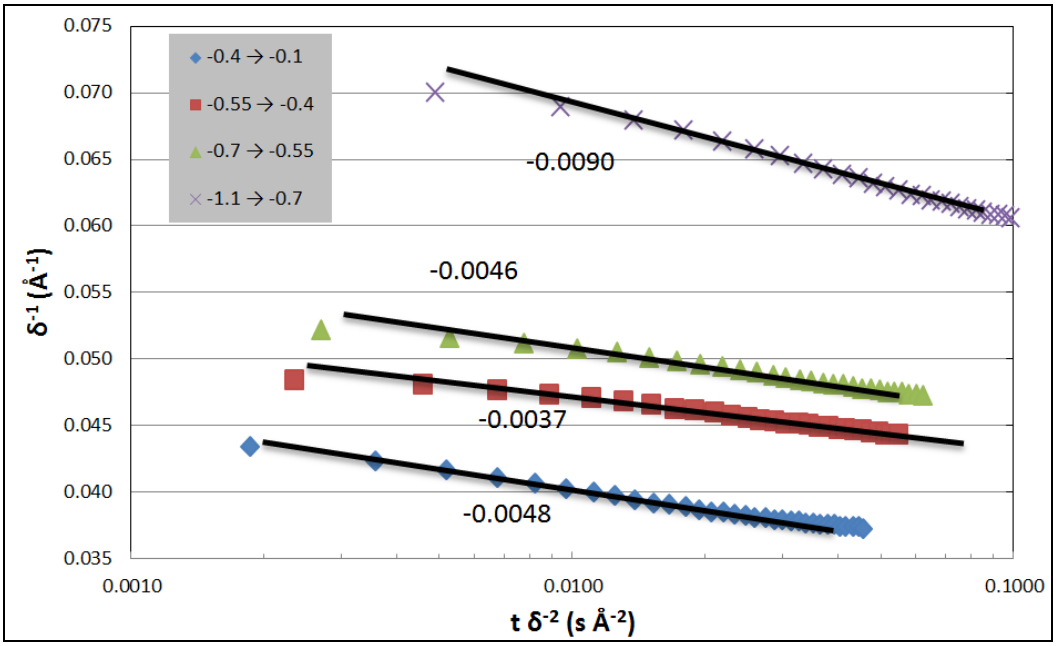

Figure 4.7 Inverse thickness, calculated from current transients, as a function of log (t/δ2) corresponding to successive potential steps specified in the legend, in 25 mM (same solution conditions as previous plot.) acetate buffer at pH = 6. The numbers indicate the slopes of the straight-line fits in $Å^{-1}$.

This type of analysis (chronoamperometry) also gives results in accordance with the Cabrera-Mott kinetics. It can be argued that the slopes obtained by fitting the two types of data (ellipsometry and chronoamperometry) to Eq. (4-1) are about the same order of magnitude for the corresponding set of experimental parameters (see also Table 4.2). The results of the replicate runs in 25 mM acetate buffer give an idea about the reproducibility of such data. In general, the slopes are somewhat larger for the larger acetic acid concentration, especially for the ellipsometry results.

Based on the obtained slope and intercept of the straight-line fits, the parameters δ_1 and u in Eq. (4-1) were calculated and given in Table 4.3. δ_1 values are considerably larger than the steady-state film thicknesses obtained from EIS, and the approximation used in obtaining Eq. (4-1) from the general form of the Cabrera-Mott equation (Eq. (2-12)) is therefore valid. Included in Table 4.3 is also the initial growth rate, γ, defined from Eq. (2.13) as

$$\gamma = \left[\frac{d\delta}{dt}\right]_{\delta_{in}} = u \exp\frac{\delta_1}{\delta_{in}} \qquad \textbf{(4-3)}$$

where δ_{in} is the steady state barrier thickness obtained by impedance spectroscopy immediately before the application of the potential step.

Using the obtained values for u, it is in addition possible to calculate the activation energy W for film growth by Eq. (4-4) derived from Eq. (2-12) and (2-13).

$$u = u_0 \exp\left(-\frac{W}{kT}\right) = N\Omega\upsilon\exp\left(-\frac{W}{kT}\right) \qquad \textbf{(4-4)}$$

where u_0 = 10^4 cm/s (or less) [17] at 22°C [17]. The results are included in Table 4.3. The chronoamperometric results give activation energies of about 1.2-1.7 eV while the ellipsometry measurement give activation energies of about 1.1-1.9 eV. These results agree well with the activation energy of about 1.3±0.15 eV reported in Ref. [18], based on a comparison of field strengths obtained from spectrophotometric and amperometric measurements. The δ_1 values in Table 4.3 are also in the same range, 10^2 to 10^3 Å, as reported previously in Ref. [17].

Table 4.2 Summary of results obtained by analysis of barrier-film growth data, based on ellipsometric and electrochemical measurements, by use of Cabrera-Mott inverse square logarithmic growth law.

Electrolyte properties		Potential Step (V)			
pH	[HAc](mM)	-1.1 → -0.7	-0.7 → -0.55	-0.55 → -0.4	-0.4 → -0.1
		Slope based on ellipsometry ($Å^{-1}$)			
6	25	-0.0049	-0.0071	-0.0077	-0.0040
6	13	-0.0047	-0.0040	-0.0029	-0.0024
		Slope based on current transient ($Å^{-1}$)			
6	25	-0.0074	-0.0042	-0.0033	-0.0038
6	25	-0.0090	-0.0046	-0.0037	-0.0048
6	13	-0.0074	-0.0034	-0.0029	-0.0035

Table 4.3 Parameters δ_1 , u, γ and W calculated from the data in Fig. 4.3 to Fig. 4.7.

Electrolyte		Potential Step (V)															
pH	[HAc] (mM)	-1.1 → -0.7				-0.7 → -0.55				-0.55 → -0.4				-0.4 → -0.1			
		δ_1 (Å)	u (Å/s)	γ (Å/s)	W (eV)	δ_1 (Å)	u (Å/s)	γ (Å/s)	W (eV)	δ_1 (Å)	u (Å/s)	W (eV)	γ (Å/s)	δ_1 (Å)	u (Å/s)	γ (Å/s)	W (eV)
Based on ellipsometry measurements																	
6	25	$4.7x10^{2}$	$1.5x10^{-15}$	$8.4x10^{-5}$	1.57	$3.2x10^{2}$	$6.6x10^{-9}$	$1.7x10^{-1}$	1.18	$3.0x10^{2}$	$9.5x10^{-8}$	1.11	$2.1x10^{-1}$	$5.8x10^{2}$	$2.5x10^{-12}$	$3.6x10^{-1}$	1.38
6	13	$4.9x10^{2}$	$6.6x10^{-17}$	$1.0x10^{-1}$	1.65	$5.8x10^{2}$	$5.0x10^{-15}$	$7.2x10^{-2}$	1.54	$7.9x10^{2}$	$1.1x10^{-18}$	1.76	$7.1x10^{-2}$	$9.6x10^{2}$	$1.3x10^{-20}$	$5.0x10^{-2}$	1.87
Based on current density measurements																	
6	25	$2.6x10^{2}$	$7.8x10^{-9}$	$6.8x10^{-1}$	1.18	$5.0x10^{2}$	$1.9x10^{-12}$	$5.3x10^{-1}$	1.39	$6.2x10^{2}$	$3.4x10^{-14}$	1.49	$5.2x10^{-1}$	$4.8x10^{2}$	$9.6x10^{-10}$	$1.9x10^{0}$	1.23
6	25	$3.1x10^{2}$	$1.9x10^{-10}$	$8.8x10^{-1}$	1.27	$5.5x10^{2}$	$1.2x10^{-13}$	$4.0x10^{-1}$	1.46	$7.0x10^{2}$	$6.6x10^{-16}$	1.59	$4.0x10^{-1}$	$6.1x10^{2}$	$2.1x10^{-12}$	$1.2x10^{-1}$	1.39
6	13	$3.1x10^{2}$	$2.1x10^{-10}$	$9.6x10^{-1}$	1.27	$6.8x10^{2}$	$1.7x10^{-16}$	$5.1x10^{-1}$	1.63	$7.9x10^{2}$	$6.6x10^{-18}$	1.71	$4.4x10^{-1}$	$6.6x10^{2}$	$2.0x10^{-13}$	$1.1x10^{-1}$	1.45

4.4.2 Transient behaviour during oxide thinning

Fig. 4.8 and Fig. 4.9 show the changes in the barrier oxide thickness and current density as a function of time following various negative potential steps in the potential range from -1.1 to -0.1 V for solution concentrations 13 and 25 mM HAc buffer, respectively. Thickness changes in the barrier layer, measured from the ellipsometric data (Fig. 4.8a and Fig. 4.9a), were about 1.2 nm/V, in accordance with the expected literature result. However, the time scale required for the change was much larger than that measured for film growth above.

The current transients (Fig. 4.8b and Fig. 4.9b) showed anomalous behaviour, which could not directly be related to barrier oxide dissolution. For example, the steady state current density just before the onset of the potential step at -0.1 V was 6.8 $\mu A/cm^2$ for the 19mM HAc run (Fig. 4.8b). After the step, it decreased toward a minimum during oxide dissolution. As the oxide thickness started attaining a steady-state value, the current density started increasing again toward its expected steady-state value of 6.4 $\mu A/cm^2$ at -0.4 V. The initial decrease in the current density is attributed to the reduction of the electric field due to lowering of the applied potential. As the barrier film became thinner with time, its resistance decreased, allowing an increase in the leakage current density as the steady-state barrier thickness was approached. Analogous behaviour was observed for the subsequent potential steps starting at -0.4 and -0.55 V. The final step from -0.7 to -1.1 V did not generate a significant current response. The low net current persisting during the period of the run is attributed to the contribution from onset of significant hydrogen evolution cancelling the positive leakage current. Similar results were obtained for experiments in 25 mM HAc solutions. In this case the effect of hydrogen evolution in the current response after the -0.7 to -1.1 V step is more evident. The differences observed in the current transients for the two buffer concentrations must be related to the buffer capacity. The low capacity of the 13mM solution probably could not prevent local pH changes at the surface. The surface was activated due to pH decrease from hydrolysis of Al^{3+} ions at the more positive potentials, and it became more passive by pH increase resulting from hydrogen evolution at the most negative potential. Further analysis of film dissolution data was therefore limited to the ellipsometry data alone.

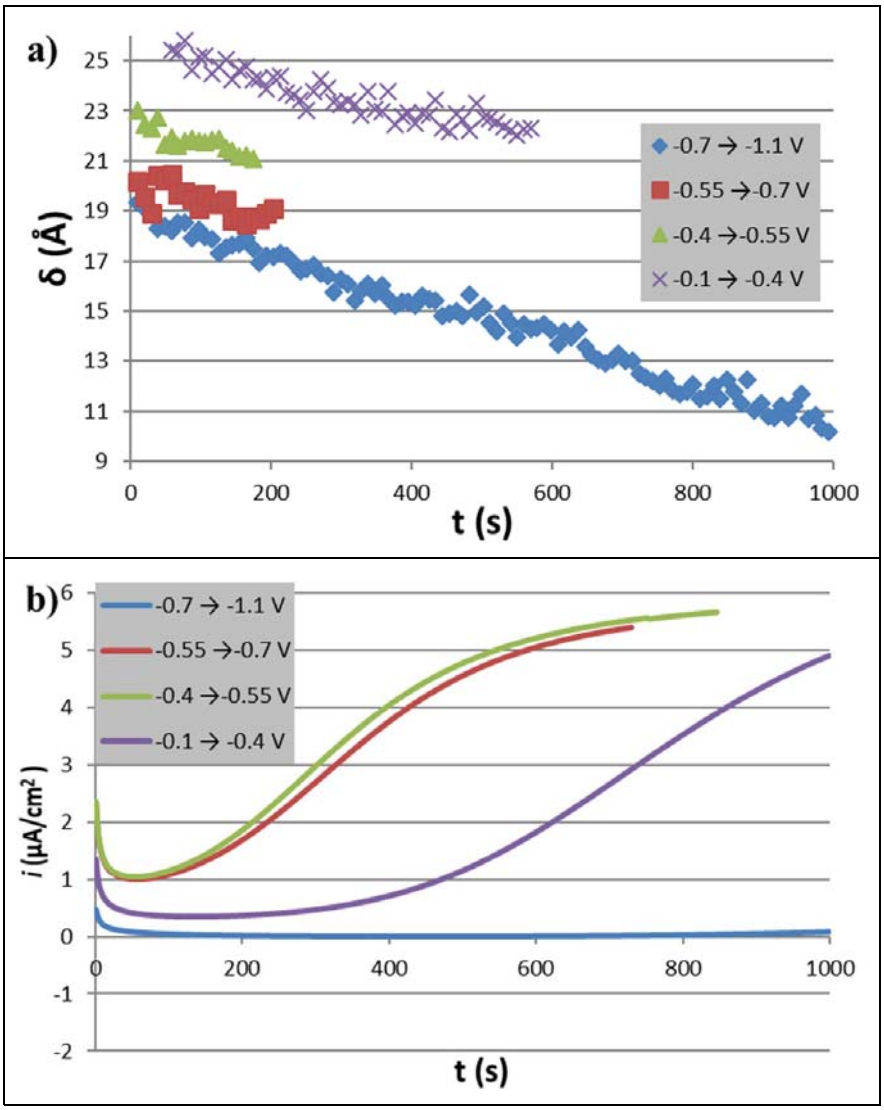

Figure 4.8 Changes in (a) the barrier oxide thickness and (b)current density as a function of time following successive negative potential steps in the range -1.1 to -0.1 V in 13 mM acetate buffer at pH = 6.

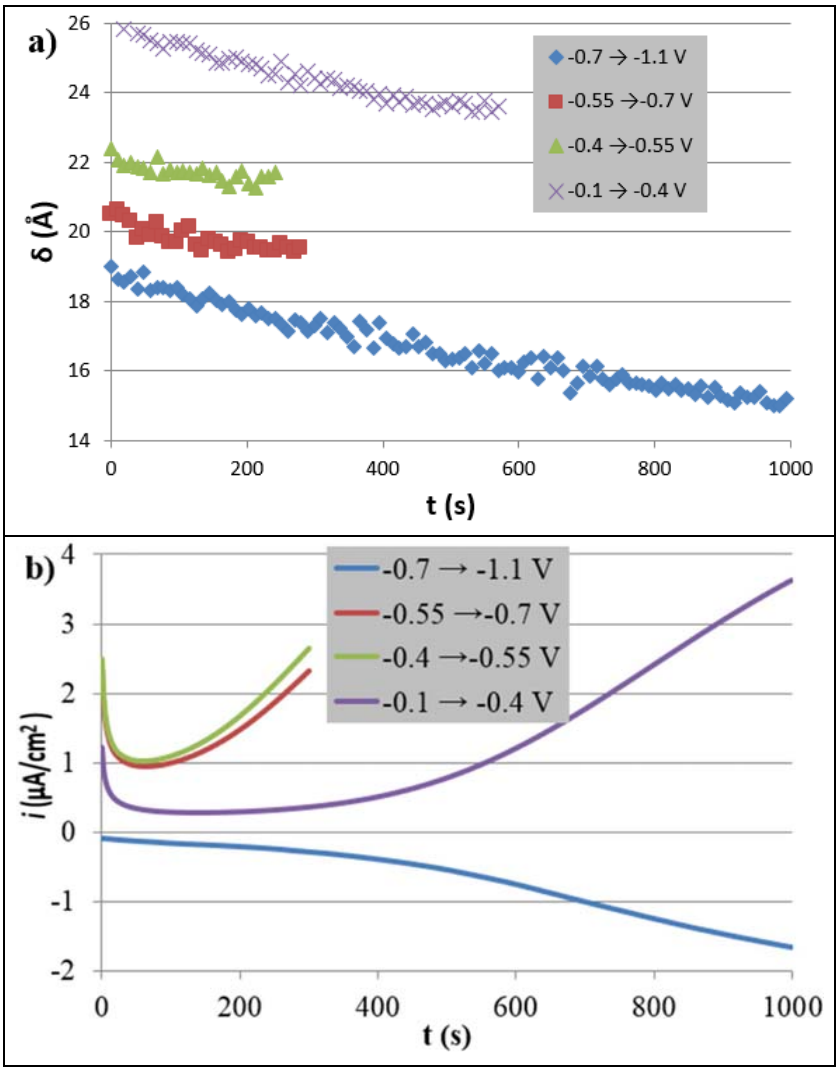

Figure 4.9 Changes in (a) the barrier oxide thickness and (b) current density as a function of time following successive negative potential steps in the range -1.1 to -0.1 V in 25 mM acetate buffer at pH = 6.

Film dissolution data were first analysed by use of the inverse square logarithmic law Eq. (4-1) in the same manner as the film-growth data (Fig. 4.3). The short-time part of the curves (first 100 seconds), shown in Fig. 4.10 and Fig. 4.11, appear to obey the law, exhibiting slopes of the order 10^{-3} $Å^{-1}$ on average, as shown in Table 4.4. This is somewhat smaller than the average slope for the oxide growth data. However, it is of the same order of magnitude, indicating that the first part of the dissolution period may be governed by similar high-field assisted kinetics as in oxide growth.

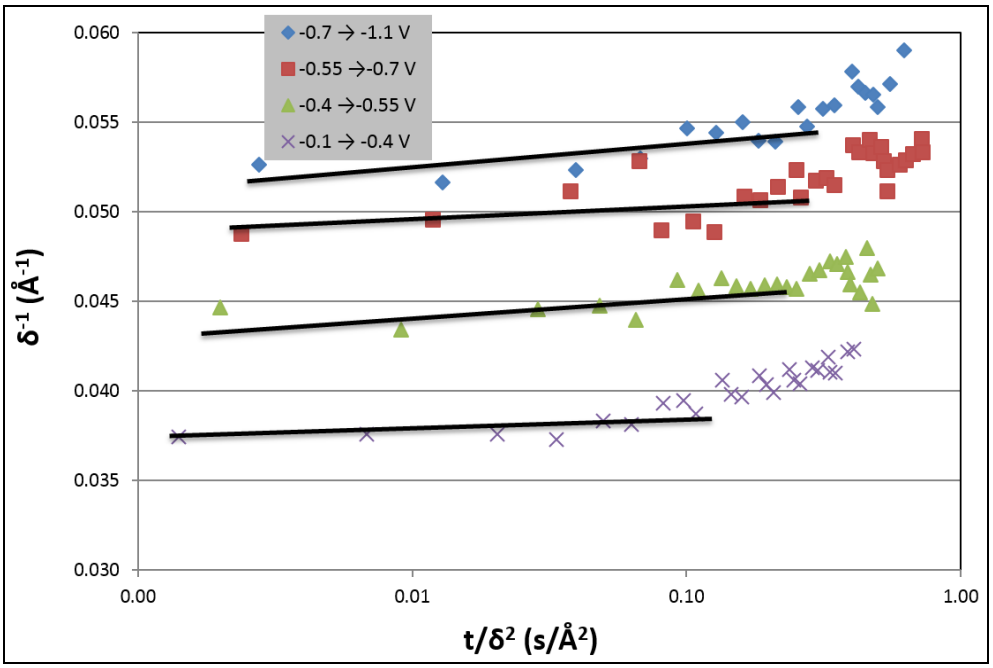

Figure 4.10 Correlation of the barrier layer thickness according to the Cabrera-Mott law, Eq. (4-1), for the negative potential steps specified in the legend, in 13 mM acetate buffer at pH = 6.

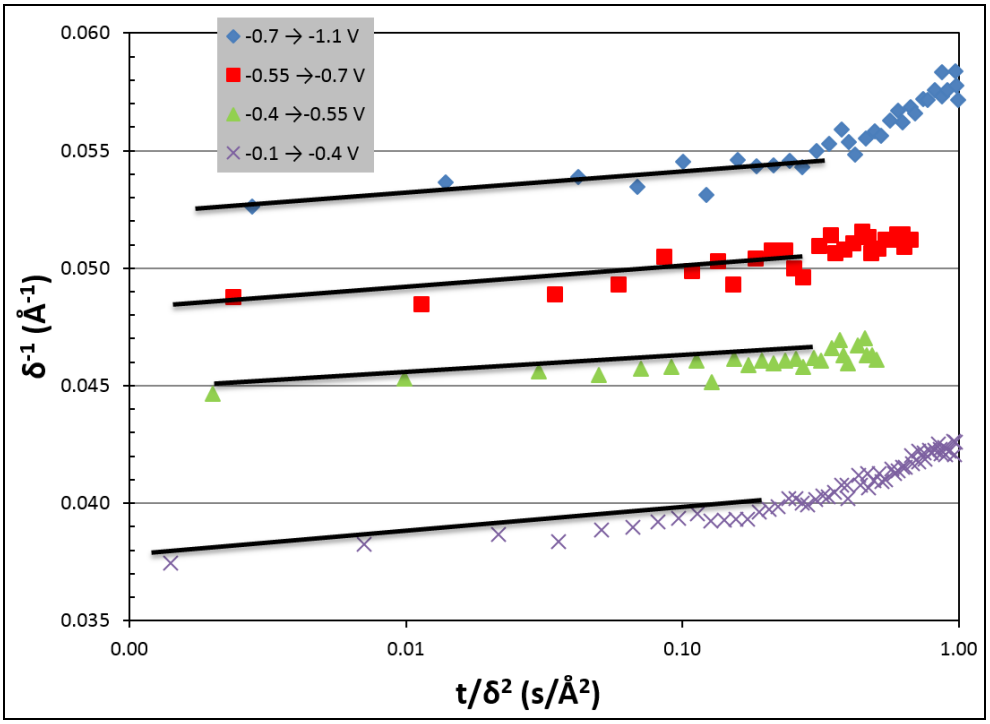

Figure 4.11 Correlation of the barrier layer thickness according to Cabrera-Mott law, Eq. (4-1), for the negative potential steps specified in the legend, in 25 mM acetate buffer at pH = 6.

Table 4.4 Summary of the slopes obtained by fitting the short-time barrier-film thinning data to the Cabrera-Mott inverse square logarithmic growth law.

Electrolyte properties		Potential Step (V)			
pH	[HAc](mM)	-0.7 → -1.1	-0.55 → -0.7	-0.4 → -0.55	-0.1 → -0.4
		Slope ($Å^{-1}$/divison)			
6	25	$8.1x10^{-4}$	$1.03x10^{-3}$	$1.05x10^{-3}$	$1.73x10^{-3}$
6	13	$1.43x10^{-3}$	$6.6x10^{-4}$	$1.01x10^{-3}$	$7.0x10^{-4}$

The ellipsometric data were next analysed by use of solutions to Fick's second law to see if film thinning was mass transfer controlled by diffusion of dissolved Al^{3+} ions from the barrier layer surface into the solution [9]. The film thickness change for a semi-infinite volume of electrolyte for a time interval Δt, is related to the diffusion coefficient D by [19]

$$\Delta\delta = c_0\left(\frac{D\Delta t}{\pi}\right)^{\frac{1}{2}}\frac{M_n}{\rho} \qquad \textbf{(4-5)}$$

where c_0 is the solubility of aluminium ions at the barrier surface, assumed constant for a given potential step, ρ is the oxide density and M_n is the molecular weight of the oxide. Eq. (4-5) shows that δ should vary in direct proportion to $(\Delta t)^{\frac{1}{2}}$ if film thinning is mass transfer controlled.

Fig. 4.12 and Fig. 4.13 show the barrier oxide thickness, obtained from ellipsometry measurements, as a function of the square root of time for various negative potentials steps. The obtained dissolution rates were similar for all the potential steps for a given buffer concentration. The higher noise level and dissolution rate observed for the data obtained in the low buffer capacity 13 mM acetate buffer are attributed to local pH fluctuations, e.g., due to metal ion hydrolysis or hydrogen evolution, which in turn affect the solubility of the barrier oxide and the diffusion coefficient of the diffusing species. The cause of sudden change in the slope of -0.7 to -1.1 V step (Fig. 4.12) is not known. It can be concluded that barrier-film dissolution in the present test solutions and applied potentials is mass transfer controlled.

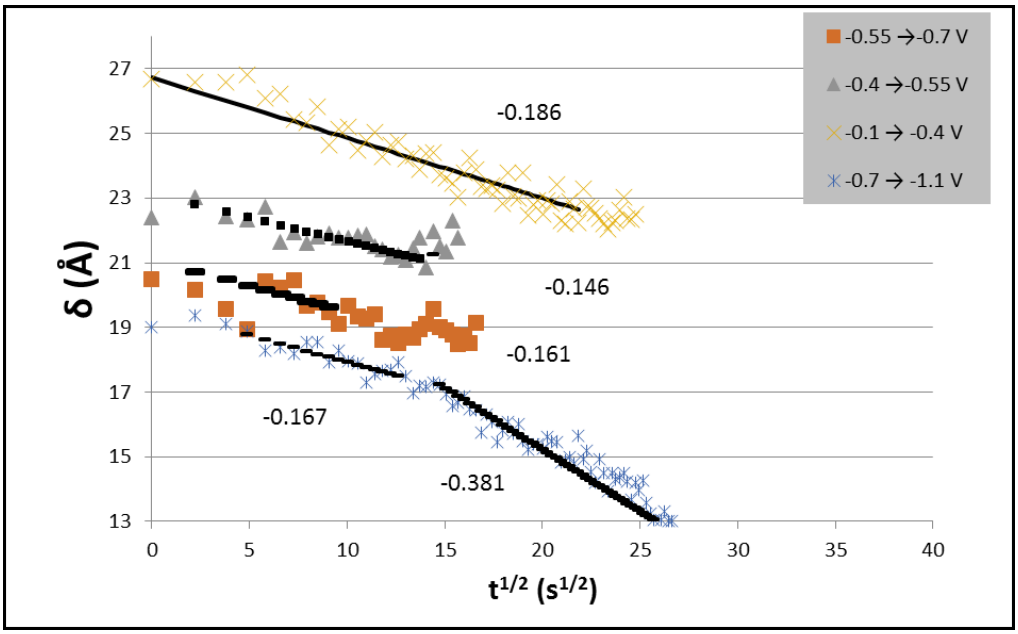

Figure 4.12 Barrier layer thickness plotted as a function of square root of time following negative potential steps in 13 mM sodium acetate buffer at pH = 6.

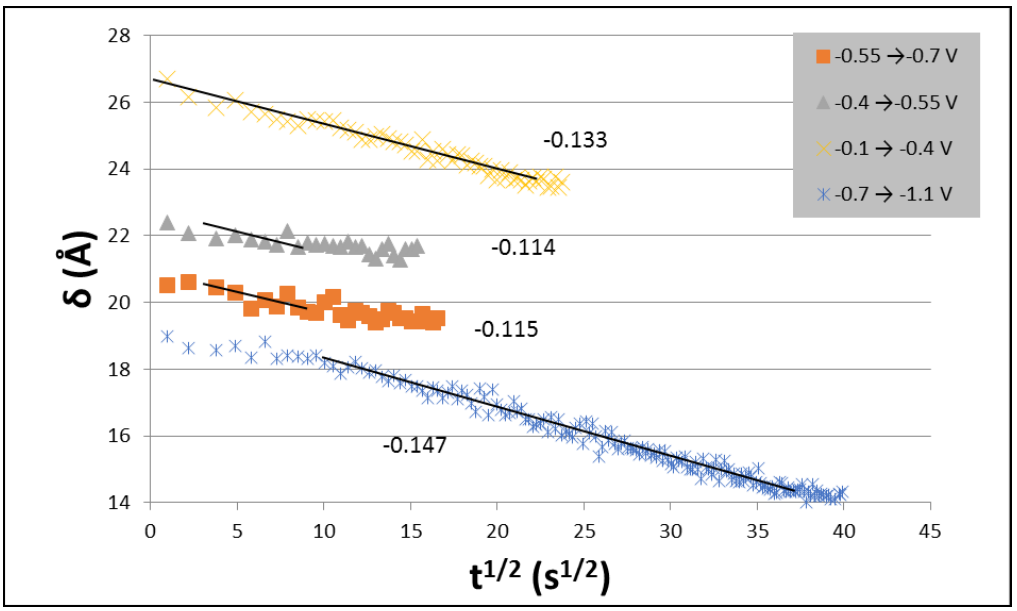

Figure 4.13 Barrier layer thickness plotted as a function of square root of time following negative potential steps in 25 mM sodium acetate buffer at pH = 6.

For further verification of mass transfer control, data available for the diffusion coefficient D of Al^{3+}, can be used to calculate the solubility of the oxide c_0 from the slope of the data in Fig.

4.12 and 4.13. The diffusion coefficient of Al^{3+} at infinite dilution is reported to be about $3.5 \cdot 10^{-6}$ cm^2/s at 18°C and $5.6 \cdot 10^{-6}$ cm^2/s at 25°C [20], based on calculations from equivalent conductivity data obtained from Ref. [21]. Based on these data, we assume a diffusion coefficient of $5 \cdot 10^{-6}$ cm^2/s to be valid for present test solution at 22°C (lab temperature).

Assuming that the barrier oxide is boehmite or bayerite, the oxide solubilities at pH = 6 should be about 10^{-6} M or 10^{-7} M, respectively [22]. By using the assumed diffusion coefficient and the data in Fig. 4.12 and 4.13, c_0 is calculated to lie in the range $3.3 \cdot 10^{-5}$ to $5.2 \cdot 10^{-5}$ mol/l (Table 4.5), i.e. one to two orders of magnitude higher.

Table 4.5 Solubility of Al^{3+} calculated by fitting the ellipsometry data for film thinning in response to decreasing potential steps in acetate buffer solutions. Diffusion coefficient of Al^{3+} was assumed to be $5 \cdot 10^{-6}$ cm^2/s.

Electrolyte properties		Potential Step (V)				Average
pH	[HAc] (mM)	-0.1 → -0.4	-0.4 → -0.55	-0.55 → -0.7	-0.7 → -1.1	
		Solubility (mol/l) $\cdot 10^{-5}$				
6	25	4.1	3.5	3.6	4.5	3.9
6	13	5.7	4.5	5.0	5.2	5.1

4.5 Discussion

The proposed methodology for assessing barrier-oxide growth and dissolution on pure aluminium is based on frequent steady-state thickness calibration between the subsequent potential steps and attempt to measure the thickness transients by two simultaneous *in situ* methods. The proposed combination of techniques decreases the chance of unforeseen errors and thereby increases the reliability of the approach. It became clear from the oxide growth measurements that the multi-wavelength ellipsometric technique is not fast enough to monitor film growth as accurately as expected. However, this drawback appears to be alleviated by the chronoamperometric measurements. The degree of agreement between the two methods in addition gives additional confidence regarding the accuracy of the thickness measurements. In contrast, the ellipsometric data is to be relied on in film-dissolution measurements. The current response data is complicated due to contributions from a number of factors discussed above and the fact that such data by definition cannot be used for a chemical process (film dissolution).

The ellipsometry data are not reliable for film growth measurements because about 10 s are required to obtain one data point, during which the film thickens by a few Å. However, speeding up the measurement process by returning to the conventional approach of single-wavelength measurement would help. The data-analysis routine can be simplified to a one-layer model, consisting of the barrier layer with variable thickness. The hydrated layer would then be treated as a part of the test solution near the surface with constant properties. The analysis of the ellipsometric growth data at least verifies that the change of properties of the hydrated layer can be ignored during the rapid growth period of the barrier layer, justifying this assumption.

One uncertainty about the chronoamperometric measurements for film growth is the determination of i_{ss} in Eq. (4-2), which corresponds to leakage current after the barrier film reaches steady-state thickness. This is difficult to determine from the current transients, which require a long time to attain a steady state. These transients are also determined by other factors than barrier-layer growth at large times. The selection of this value was therefore based on the ellipsometry data, which indicated that a quasi-steady-state thickness is achieved after about 50 seconds for all the investigated samples. This approach appears to give satisfactory results.

The film dissolution data had to be based purely on the ellipsometric data. Since the dissolution rate is by about two orders magnitude slower than the growth rate, the 10 s delay caused by ellipsometric measurement becomes less consequential. In addition, since the contribution from the dissolution of the hydrated layer to the ellipsometric results may become important due to the increased time of the measurement, the capability of the method for correcting for this by the multi-wavelength, multilayer analysis capability becomes an advantage. In view of the foregoing, the suggested methodology emphasizes the preference of the chronoamperometric approach for film growth and the ellipsometric measurements for film dissolution for aluminium.

With the foregoing approach, the present data show that the growth of the barrier oxide layer on pure aluminium in buffered aqueous solution occurs according to the Cabrera-Mott inverse square logarithmic law. As discussed in Chapter 2 [4,5,8], this law is a special case of the classical high-field growth law (Eq. (2-5)), shown to apply to film growth on Al in aqueous solution [17]. However, as long as the underlying assumptions are obeyed (thin film without space charge [23]), the parameters u and δ_1 obtainable from the growth data by use of the integrated form (Ghez) of the Cabrera-Mott law contributes significantly in quantifying the properties of the barrier layer. It is of present interest to study how these properties change by alloying, thermo mechanical and chemical processing of aluminium alloys, as will be discussed in the next chapters. This is expected to be an important contribution since the surface characterization of Al alloys have so far been limited by and large to characterization of the metal surface and the metal-oxide interface. Study of the film properties *per se* and their effect on the electrochemical and corrosion properties is very limited in connection with the development and characterization of commercial alloys.

Dissolution of the barrier oxide in response to a negative potential step also appears to obey the Cabrera-Mott inverse square logarithmic law immediately after the potential step. However, the dissolution rate quickly converts to a mass-transfer controlled kinetics according to Fick's second law, suggesting that the rate of barrier film dissolution on aluminium is largely a chemical process in aqueous solution. This result is in agreement with the earlier work on corrosion of Al alloys in flowing seawater [9,24]. In that work, uniform corrosion rates measured under open circuit conditions was correlated with values calculated theoretically from convective mass transfer considerations for flow past flat plates and cross-flow around cylindrical specimens. The calculations were based on the assumption of equilibrium at the oxide surface to calculate the solubility of oxide film and a value of 10^{-5} cm^2/s for the diffusion coefficient of the dissolving aluminate as in the present study. Application of a cathodic potential did not affect the corrosion rate, *i.e.*, cathodic protection was not possible to reduce the uniform corrosion rate, although it was effective in eliminating pitting. It was concluded, therefore, that the corrosion rate was determined by mass-transfer controlled chemical dissolution of the oxide.

Calculations of aluminium ion concentration (solubility) at the barrier surface were based on a constant diffusion coefficient obtained from the literature [20], which was calculated from equivalent conductivity data at infinite dilution, obtained from Landolt-Börnstein tables [21]. This is based on the assumption that the dilute solution approximations are valid for the solutions used. However, the diffusion coefficient can vary with the solution concentration, especially if the

transport of species occurs through the hydrated and porous hydrated outer oxide layer, which may have a quite different chemistry in relation to the bulk solution. The exact chemical nature of the Al species diffusing in this environment is not known. The presence of an electric field can also assist the outward transport of Al^{3+} ions, giving an order of magnitude increase to an effective diffusion coefficient. Calculation of the oxide solubility with the assumption that the diffusion coefficient of Al^{3+} is about 10^{-5} cm^2/s would give an oxide solubility closer to the equilibrium value.

In addition to the foregoing, the assumption of equilibrium at the oxide-solution interface for estimating c_o may not be entirely correct in view of the fact that the current density never becomes zero at the surface. The source of this current may be direct migration of Al^{3+} ions through the barrier oxide (leakage current) and/or metal oxidation at the metal-oxide interface to compensate for chemical oxide dissolution at the oxide-solution interface to maintain the electric field constant in the barrier layer. The field may also change during the transient measurements due to change in the oxide thickness and properties. These factors may affect the boundary condition for the oxide surface (constant solubility assumption), suggesting time dependent variations in the factors controlling the transport phenomena. Another possible factor is the effect of the geometry of the diffusion path, which may depend on the morphology of the hydrated layer. Also due to relatively low buffer capacities, it is expected that the local pH, due to the reaction between ejected Al^{3+} ions and water, may become smaller than the pH in the bulk solution, resulting in an increased solubility [22], which contributes to explaining that the measured solubilities are larger than their thermodynamic values [22]. This is supported by the higher obtained solubilities for the lowest buffer capacity in Table 4.5. The applied potential may also increase the solubility of the oxide [11,12]. Dissolution of the barrier oxide depends further on the formation of hydrides, which is shown to be potential dependent [25]. In any event, the proposed method of analysing the film-dissolution data allows the measurement of another parameter, i.e., the film solubility if the diffusion coefficient of Al^{3+} is known. This may be a useful parameter in investigating the passivity of the oxide as a function of environmental factors under irreversible conditions.

Despite these complicating factors, the results presented in Fig. 4.12 and Fig. 4.13 are considered as convincing evidence for mass transfer controlled oxide dissolution and validity of the assumptions involved in the present data analysis. However, several studies, related to anodizing of aluminium in highly acidic solutions and high applied potentials, have concluded that barrier oxide dissolution is an electrochemical process based on the observation that the dissolution rate is affected by the applied potential [11,26]. As discussed above, the oxide solubility is dependent on the applied potential, thereby affecting the initial condition to the solution of Fick's 2nd law and the magnitude of the driving force for diffusion. The possible effect of migration is also discussed. However, this effect must be more important in studies involving high applied potentials in dissolution of the barrier layer between the metal surface and the porous oxide layer, which is the subject often discussed in the available literature. The present results are restricted to low applied potentials in slightly acidic or neutral solutions.

The main arguments are an observed increase in reduction in overall dissolution rate with an increase in end-potential of a negative potential step [11] and an increase in the dissolution rate with applied negative potential step. However, as reviewed earlier in this chapter, the potential step-size was decreased by the same amount as the increase in end-potential. A similar reduction in dissolution rate with potential step size is reported in Ref. [12], which again was considered to be caused by field assisted barrier oxide dissolution. These results can also be interpreted in terms of a mass-transfer controlled dissolution, in accordance with this chapter, as a larger step-size will result in a lower time-averaged dissolution rate, due to the reduction in dissolution rate as a function of time observed clearly in Fig. 4.12 and Fig. 4.13.

4.6 Conclusions

- Growth of barrier oxide on pure aluminium in aqueous acetate buffer solution was consistent with the Cabrera-Mott inverse square logarithmic growth law.
- The Cabrera-Mott parameters, which can be obtained from data analysis, provide an *in situ* quantitative basis for studying oxide growth kinetics in aqueous solution.
- The activation energy calculated from the Cabrera-Mott formulation for barrier-oxide formation in acetate buffer was similar to the values reported in the literature, obtained by use of different techniques.
- Oxide dissolution is a mass transfer controlled process, involving chemical dissolution of the oxide and egress of dissolved aluminium species by diffusion.
- Potential dependence of the dissolution rate is attributed to potential dependent non-equilibrium solubility of the oxide. Migration in the solution can play a role.
- It is possible to obtain the non-equilibrium oxide solubility *in situ* under well-defined electrochemical conditions in aqueous solution by use of the present methodology.
- The classical chronoamperometric approach is shown to be well-suited for high-field oxide growth in aqueous solution, whereas the ellipsometric approach needs further study for improving the rate of data acquisition.
- The multi-wavelength visual light ellipsometry is well suited to study the slower rate barrier oxide dissolution in a composite (multilayer) system.
- Electrochemical impedance spectroscopy is a reliable calibration method for measuring the oxide thickness during quasi-steady state intervals between the potential steps of the chronoamperometric approach.
- Combination of ellipsometry and electrochemical techniques thus provides a complementary and reliable methodology for *in situ* investigation of barrier-oxide film growth and dissolution on aluminium, probably applicable also to other metals.

4.7 References

[1] Guntherschulze, A. and Betz, H. *Z. Phys.* **92**, 367 (1934).

[2] Diggle, J. W., Downie, T. C., and Goulding, C. W. *Chem. Rev.* **69**, 365 (1969).

[3] Johansen, H. A., Adams, G. B., and Rysselberghe, P. *J. Electrochem. Soc.* **104**(6), 339-346 (1957).

[4] Gudic, S., Radosevic, J., Krpan-Lisica, D., and Kliskic, M. *Electrochim. Acta* **46**(16), 2515 - 2526 (2001).

[5] Hasenay, D. and Seruga, M. *J. Appl. Electrochem.* **37**(9), 1001-1008 (2007).

[6] Lukac, C., Lumsden, J. B., Smialowska, S., and Staehle, R. W. *J. Electrochem. Soc.* **122**(12), 1571-1579 (1975).

[7] Greef, B. and Norman, C. *J. Electrochem. Soc.* **132**, 2362 (1985).

[8] Gnoinski, J., Grundwell, F., and Orchard, S. *Mater. Sci. Forum* **185-188**, 667-676 (1995).

[9] Nisancioglu, K. Corrosion behaviour and protection of copper and aluminium alloys in seawater, p.145, European Federation of Corrosion Publications No. 50. Woodhead Publishing, Cambridge, UK, (2007).

[10] Stein, N., Rommelfangen, M., Hody, V., Johann, L., and Lecuire, J. *Electrochim. Acta* **47**, 1811-1817 (2002).

[11] O'Sullivan, J. P. and Wood, G. C. *Proc. R. Soc. London, Ser. A* **317**, 511-543 (1970).

[12] Diggle, J. W., Downie, T. C., and Goulding, C. W. *J. Electrochem. Soc.* **116**, 737 (1969).

[13] Deryagin, B. V. and Friedland, R. M. *Z. tech. Phys. U.S.S.R* **18**, 1443 (1948).

[14] Thompson, G. E. *Thin Solid Films* **297**, 192 (1997).

[15] Hass, G. *J. Opt. Soc. Amer.* **39**, 532 (1949).

[16] Gudic, S., Radosevic, S., and Kliskic, M. *J. Appl. electrochem.* **26**, 1027-1035 (1996).

[17] Cabrera, N. and Mott, N. F. *Rep. Prog. Phys.* **12**, 163 (1948-1949).

[18] Harkness, A. C. and Young, L. *Can. J. Chem.* **44**, 2409 (1966).

[19] Crank, J. *The mathematics of diffusion*, 32. Oxford University Press, Ely House, London (1975).

[20] Yuan-Hui, L. and Gregory, S. *Geochim. Cosmochim. Acta* **38**(5), 703-714 (1974).

[21] Landolt-Bornstein. Zahlenwerte und Punktionen aus Physik, Chemie, Astronomie, Beophysik, Technik, Part. 7, (1960);. Springer, (1960).

[22] Pourbaix, M. *Atlas of Electrochemical Equilibria in Aqueous Solutions*. National Association of Corrosion Engineers, Houston, USA (1974).

[23] Fromhold, A. T. *Theory of Metal Oxidation Volume 1 - Fundamentals*. North Holland Publising Company, Amsterdam, Netherlands (1976).

[24] Nisancioglu, K. and Wenn, T. In 12th Scandinavian Corrosion Congress and EUROCORR 92, Espo, Finland (1992).

[25] Perrault, G. G. *J. Electrochem. Soc.* **126**, 199-204 (1979).

[26] Kim, Y.-S., Pyun, S.-I., Moon, S.-M., and Kim, J.-D. *Corros. Sci.* **38**, 329-336 (1996).

5 Effect of small amount of alloyed lead on barrier oxide properties of aluminium in acetate buffer

Abstract

Lead is present as a trace element (ppm level) in nearly all commercial aluminium alloys. It segregates to the surface as a result of heat treatment, the rate increasing with temperature in the range 300-600°C, significantly above 500°C. This causes passivity breakdown at potentials significantly more negative than that expected for pure Al in chloride solution. Although the effect of Pb on the electrochemical behaviour and corrosion of Al alloys has been studied extensively, the effect of Pb segregation specifically on the barrier oxide properties on aluminium is not known. The objective of this work is to investigate the effect of a small amount (20 ppm) of alloyed Pb and heat treatment on the properties of the barrier oxide on aluminium in chloride free acetate buffer in the potential range -1.1 V to -0.1 V vs. saturated Hg/Hg_2SO_4 by use of electrochemical impedance spectroscopy (EIS) and chronoamperometry. The steady state data obtained by EIS showed decreasing oxide resistivity with increasing temperature in the range (300-600°C) investigated. The film growth data obtained by chronoamperometry was analysed by use of Cabrera-Mott inverse square logarithmic law. The activation energy for film growth, obtained from this analysis, decreased with increasing heat treatment time and temperature, along with deleterious changes in the electrochemical properties of the oxide, indicating reduced passivity. These changes correlated well with reduced passivity caused by increased segregation of Pb at the aluminium substrate-film interface.

5.1 Introduction

Lead is present as a trace element at the ppm level in most commercial aluminium alloys, due to its existence in the bauxite ore. The element has been shown to be highly unstable in aluminium because of significant mismatch of the atomic sizes of the two elements, and it segregates by heat treatment first to the grain boundaries and then to the surface by heat treatment [1,2]. The rate of segregation increases with increase in the heat treatment temperature, especially at temperatures exceeding its melting point (328°C). Direct segregation from the surface grains to the surface also occurs. Pb segregates both as a nanofilm and nanosized particles along the oxide-Al metal boundary [3]. Formation of the nanofilm is exacerbated by the formation and inward growth of γAl_2O_3 crystals above 500°C [4,5].

The segregated Pb film contributes to a significant anodic activation of the surface in the presence of chloride in an aqueous environment, as indicated by an appreciable shift in the anodic breakdown potential of the surface in relation of that observed on aluminium with Pb-free surface (not heat treated) [5,6]. The particulate segregations do not have a significant effect because they do not wet the aluminium surface [7]. Activation of the surface occurs as a result of undermining of the oxide along the path of the film, as demonstrated on samples heat treated at 600°C by high-resolution FE-STEM [3]. It has been difficult to detect film segregation on samples heat treated at lower temperatures or in oxygen free environment attained by wrapping the samples in aluminium foil as an effective oxygen filter [3,7]. However, electrochemical characterization indicated activation to a smaller degree with decreasing heat treatment temperature, becoming undetectable below 300°C. The activation mechanism in the presence of chloride is not fully clarified. It is thought to occur in a manner similar to the known activation effect of liquid metals Hg and Ga [8], which occur in the absence of Cl^- in the solution [9,10]. Activation by higher melting point metals,

such as Pb, (and also In, Sn and Bi) apparently require the added presence of aggressive Cl^- in relation to passivity breakdown [8]. Previous studies of anodic activation of aluminium by these low-melting point elements have not been investigated to the extent to which the passivating properties of the barrier oxide per se are affected by segregation of the elements to the aluminium surface.

The objective of this chapter is to investigate the utility of the electrochemical methodology of the previous chapters in investigating the modification of the Al metal-barrier oxide-solution interface by external factors, in particular whether the oxide (or oxide-metal interface) properties are significantly affected by the segregation of Pb. For this purpose, a chloride-free acetate buffer solution was used to eliminate the synergistic effect of Cl^-. Ellipsometry could not be used since heat-treatment reduced the specularity of the sample surfaces.

A possible problem envisaged, related to the present methodology, is the change of film properties, relative to the air-formed film at room temperature, by heat treatment. Previous studies have shown that the amorphous air-formed film is quite stable during heat treatment in air up to 450°C. A slight thickening is observed up to 500°C with evidence of γAl_2O_3 formation locally. Above 500°C, significant oxidation of aluminium occurs by inward growth of γAl_2O_3 crystals by direct oxidation of the Al substrate, eventually covering the entire surface. Certain porosity remains between the γAl_2O_3 crystals at the grain boundaries [4]. These pores are filled with amorphous Al oxide, believed to be the remnants of the film formed at lower temperatures. Similar oxide growth kinetics is observed on the AlPb binary alloys [6]. However, segregating Pb particles at 600°C egress to the oxide surface through the pores [5].

A possible way of preventing, at least partially, the formation of γAl_2O_3 film is by filtering the oxygen in the furnace. Wrapping the sample in aluminium foil as the oxygen filter in pure Ar atmosphere has given partial success by maintaining the amorphous structure of the film with formation of a few γAl_2O_3 clusters locally [7]. The amorphous layer thickens slightly by a few nm. However, significant particulate Pb segregation still occurs on aluminium containing trace amounts of Pb in the bulk. Interfacial film segregation of Pb has not been reported under these conditions [3,7]. Presence of Pb in the alloy does not appear to affect film thickness relative to pure Al significantly, according to TEM investigation of film cross sections.

5.2 Experimental

Binary aluminium samples, containing about 20 ppm as-weighed Pb (referred to in the remainder of this paper as AlPb20), were cast from pure (99.99%) components [3,11] into 2 cm thick slabs and cold rolled down to 2.2 mm thickness. The samples could not be homogenised, since Pb, even at such low levels used here, has in practice no solubility in Al [2,12]. The samples were metallographically polished through 1 μm diamond paste, and then rinsed in ethanol and dried. They were then heat-treated at 300°C, 450°C and 600°C, from 15 up to 60 minutes. The samples prepared at 600°C were wrapped in aluminium foil and heat-treated at a nearly O_2-free environment, produced by purging the furnace with argon gas, to avoid formation of a 50 nm thick thermal barrier oxide of gamma alumina [3,5].

The experimental apparatus used for EIS and chronoamperometry was identical to the setup presented in the previous chapters. The test electrolyte was a solution of acetic acid and sodium acetate (Na-acetate buffer), 68 g/L NaAc and 7.16 g/l HAc [120 mM], which provided a fixed pH of 5.6. The same solution was used for all samples. The experiments were performed at room temperature (22 ± 1°C). The solution was exposed to ambient air. The potentials are reported with respect to the saturated Hg/Hg_2SO_4, K_2SO_4 reference electrode (MSE).

For chronoamperometry, the potential was stepped according to the sequence -1.1, -0.7, -0.55, -0.4. and -0.1 V for a given specimen, as in the previous chapters, but only the data obtained by potential stepping in the positive direction for film growth was considered here. The problems associated with the use of negative potential data are discussed in Chapter 4. The current response of the specimen for each step was recorded until a quasi-steady state was observed indicating attainment of a steady-state thickness for the barrier layer corresponding to the applied potential. The current transients were analysed by use of the Cabrera-Mott inverse square logarithmic growth law as described in Chapter 4. The EIS results, obtained at each steady state between the potential steps were fitted to the impedance model developed in Chapter 3 to obtain the equivalent circuit parameters.

Choice of Pb composition was based on the amount of earlier data available on the surface properties of this alloy in the range 5 to 50 ppm and heat-treatment temperatures in the range 300°C to 600°C [3,7]. These results show that the heat treatment temperature and the time for heat treatment were more important than the Pb concentration in determining the electrochemical and corrosion properties of the surface. This is due to the fact that the segregated nanofilm, rather than the segregated Pb particles determined these properties.

5.3 Results

5.3.1 Growth kinetics

Fig. 5.1 shows the measured current density as a function of time after several successive potential steps as discussed in the previous section and shown in the legend. The main difference between the large and small potential steps is the attained maximum value in current density soon after the step. The peaks increase with increasing potential step, thereby affecting the film-growth rate significantly. The part of the curves immediately following the maxima was used to obtain the oxide growth kinetics, as will be shown further below. The decrease of current density becomes monotonic and similar for all potential steps, after 20-30 s, as the barrier oxide reaches its steady-state thickness and the current transient is governed by factors other than field assisted growth of the barrier layer.

Fig. 5.2 to 5.5 show the effect of heat treatment conditions for the selected potential steps. The results are compared to those for pure aluminium. The current trends for all the transients in these figures are similar. The curves are almost parallel to one another. The current levels for the AlPb alloys are larger than that for pure Al. The current level in the transients increase a bit from 300 to 450°C. The level of current transients for the samples heat treated at 600°C are significantly smaller than those for the lower heat-treatment temperatures, becoming quite close to the transients for pure Al, especially for the smaller potential steps (Fig. 5.3 and 5.4).

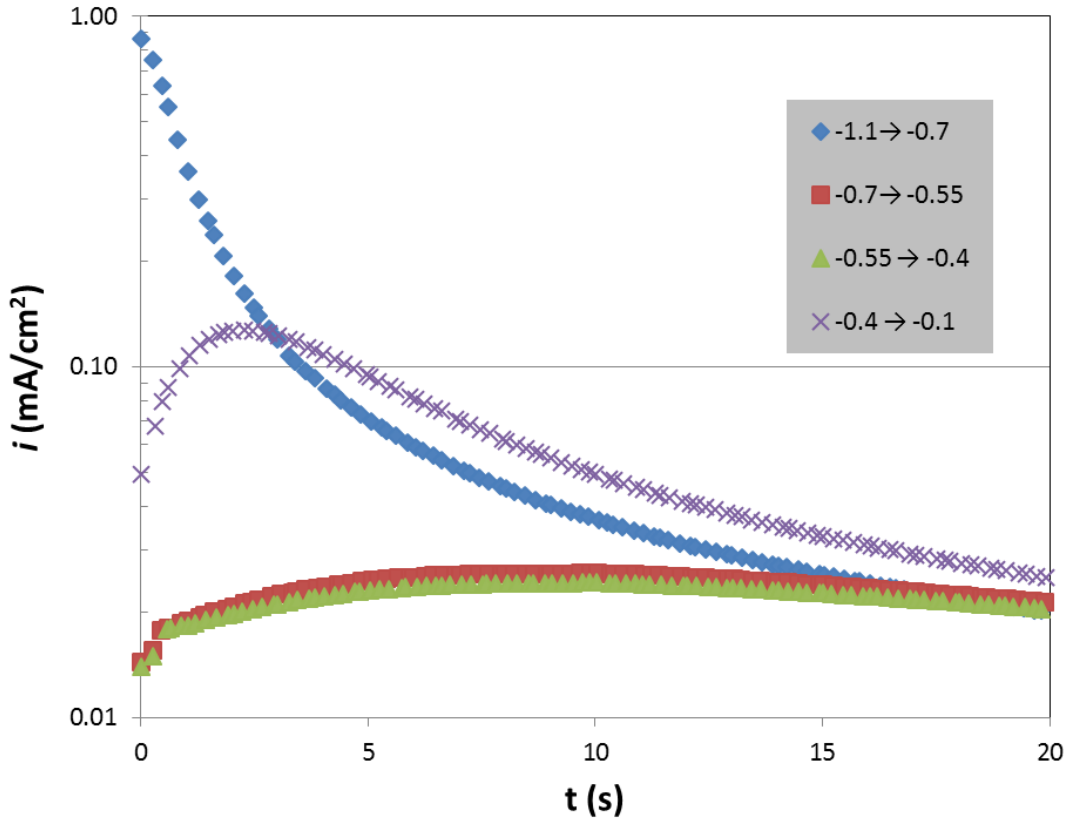

Figure 5.1 Current density vs. time for an AlPb20 sample heat-treated at 450°C for 40 minutes.

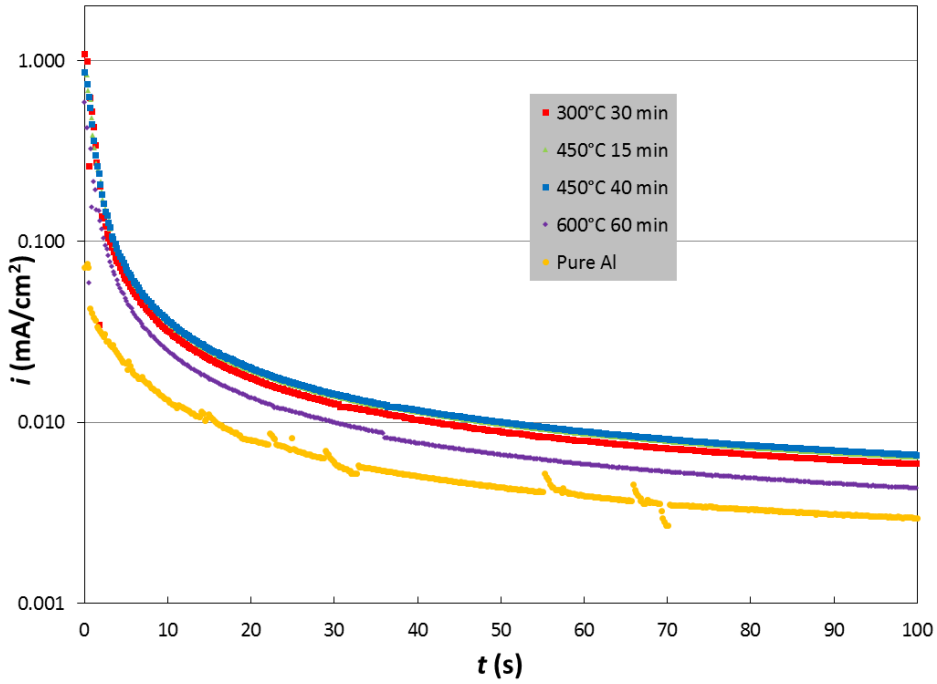

Figure 5.2 Current density vs. time after a positive potential step from -1100 mV to -700 mV for different heat treatment temperatures and periods.

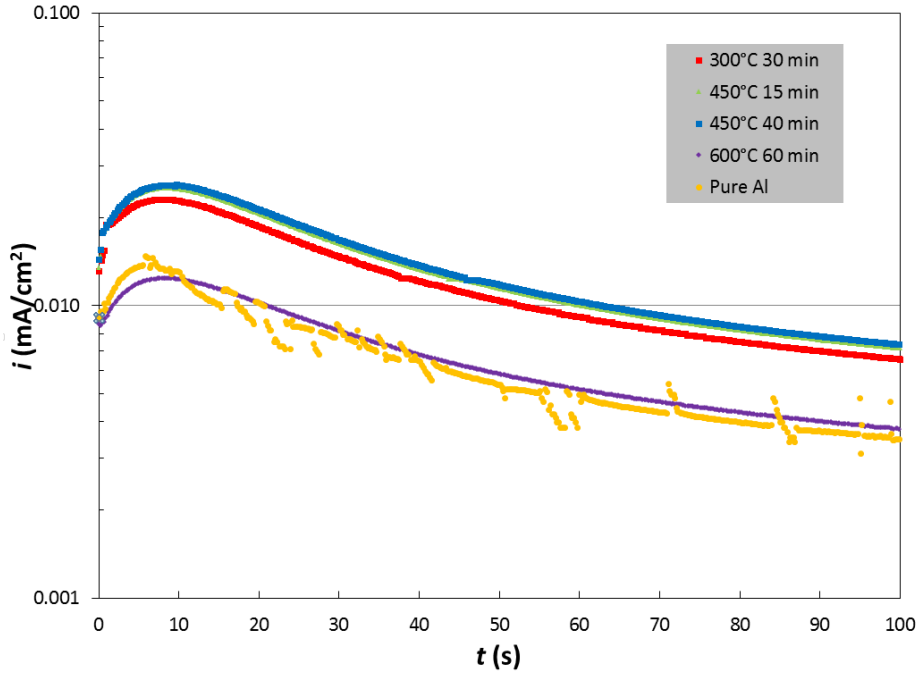

Figure 5.3 Current density vs. time after a positive potential step from -700 mV to -550 mV for different heat treatment temperatures and periods.

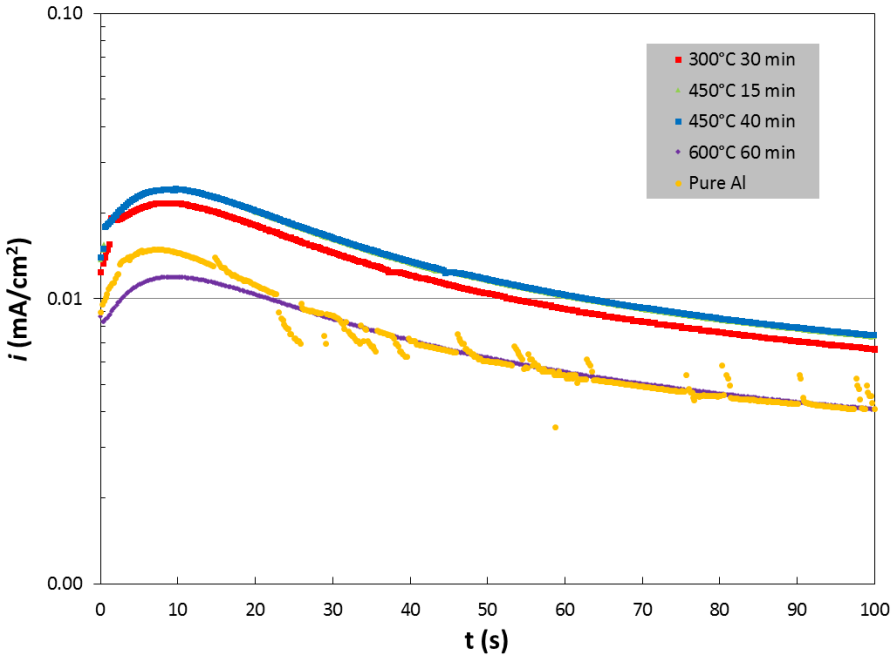

Figure 5.4 Current density vs. time after a positive potential step from -550 mV to -400 mV for different heat treatment temperatures and periods.

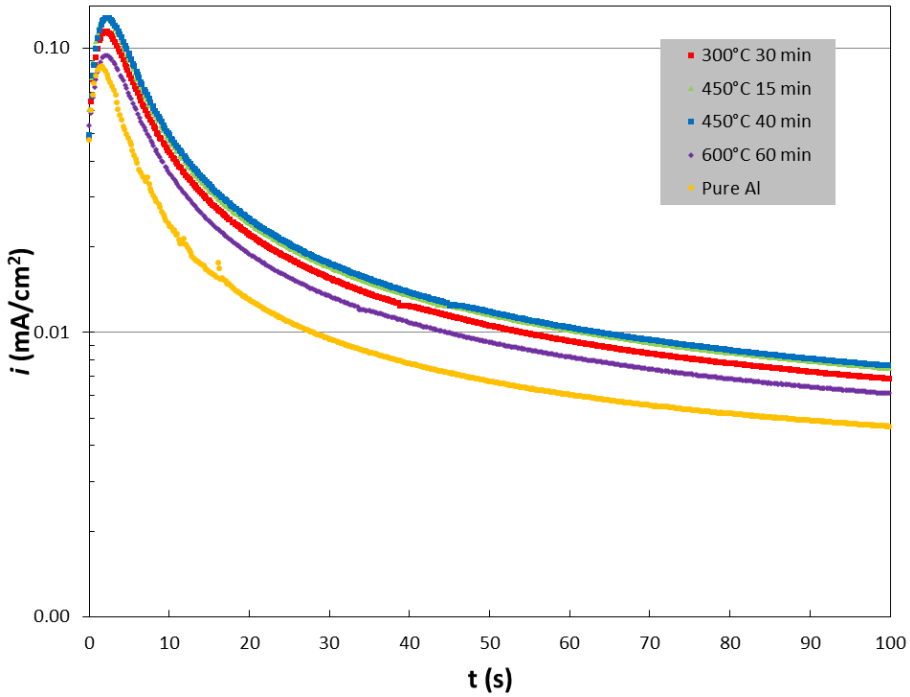

Figure 5.5 Current density vs. time after a positive potential step from -400 mV to -100 mV for different heat treatment temperatures and periods.

Fig. 5.6 to 5.10 show the inverse barrier thickness as a function of t/δ^2, as calculated from the chronoamperometric measurement shown in Fig. 5.1 to 5.5 by using the equation

$$\left(\frac{\delta_1}{\delta}\right) = \ln\left(\frac{t+\tau}{\delta^2}\right) - \ln(\delta_1 u) \qquad \textbf{(5-1)}$$

as explained in Chapter 4. The results show reasonable straight-line fits in accordance with the Cabrera-Mott inverse square logarithmic oxide growth law, with the possible exception of the data for the potential step -1.1 to -0.7 V. The time ranges within which the data were fitted are shown in the figure. For the large potential step the inverse-logarithmic region (straight line fits in the figures) occurs a few seconds after the potential step, while for smaller potential steps the inverse-logarithmic regions start after about 10 seconds, in accordance with the current transients in Fig. 5.2-5.5.

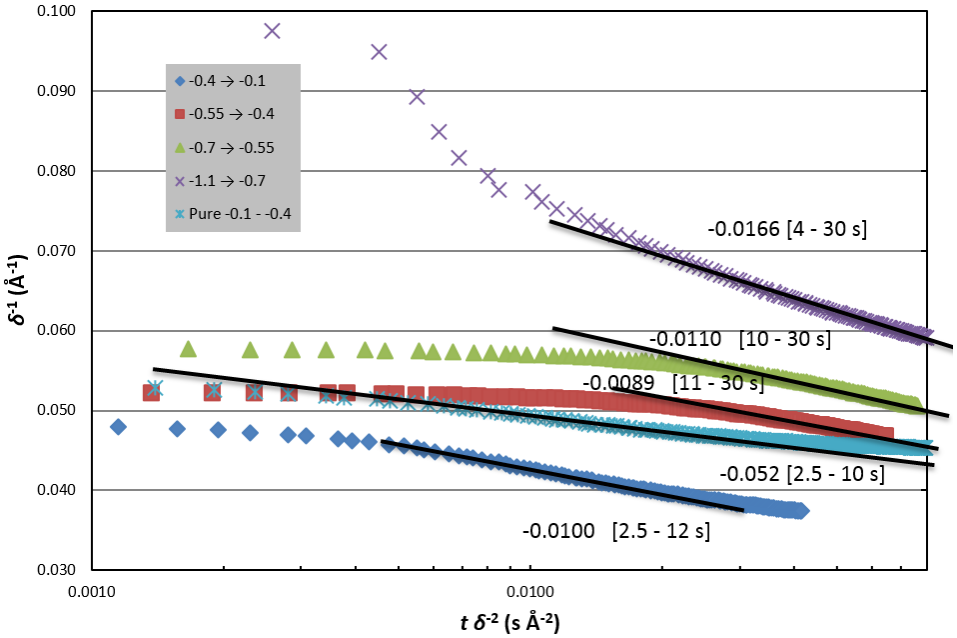

Figure 5.6 Inverse thickness, calculated from current transients, as a function of t/δ^2 corresponding to successive potential steps specified in the legend. The samples were heat treated at 300°C for 30 minutes. The slopes of the straight-line fits in Å^{-1} and the time ranges of data used for the straight-line fits are included.

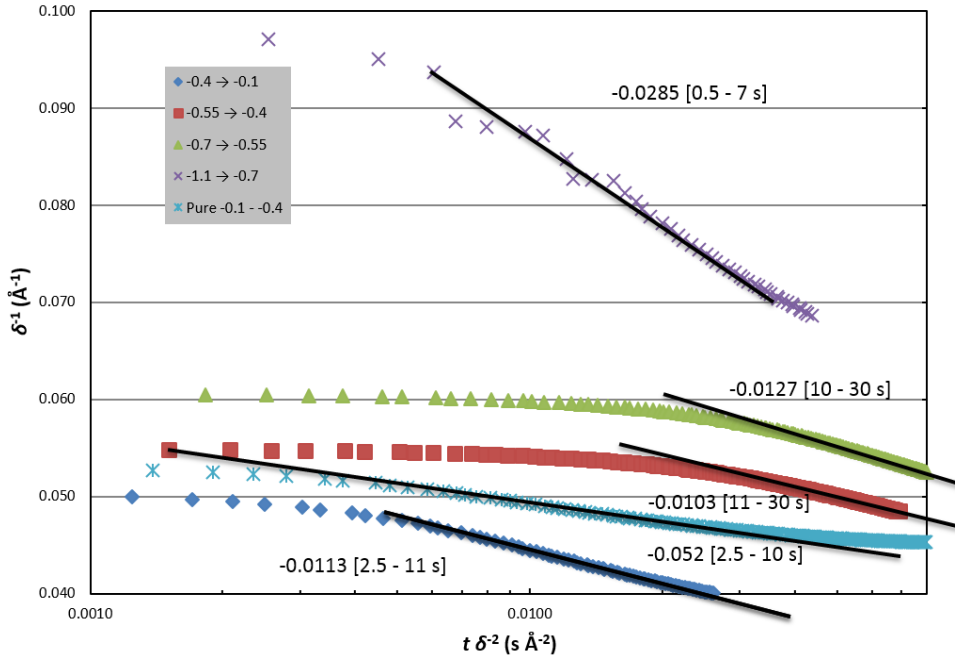

Figure 5.7 Inverse thickness, calculated from current transients, as a function of t/δ^2 corresponding to successive potential steps specified in the legend. The sample was heat treated at 300°C for 60 minutes. The slopes of the straight-line fits in $Å^{-1}$ and the time ranges of data used for the straight-line fits are included.

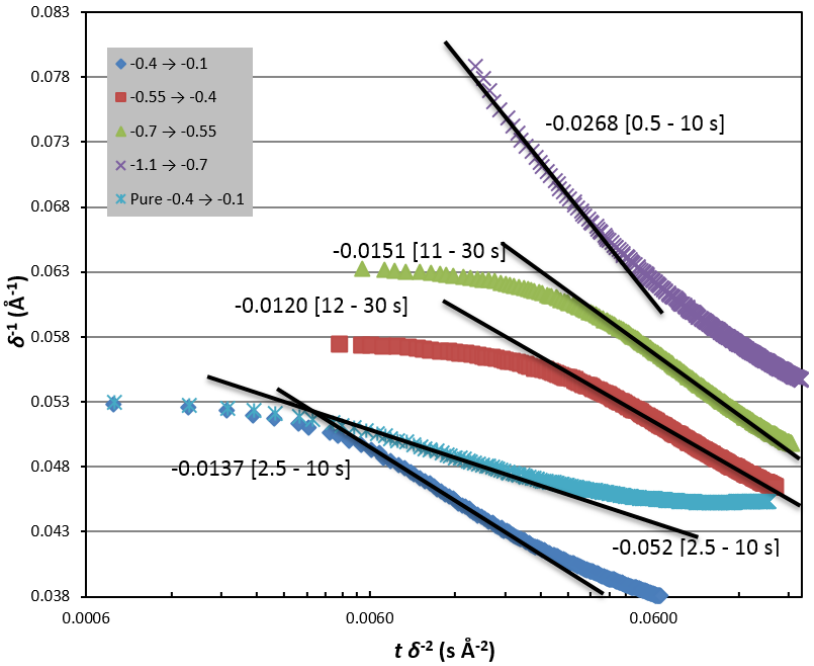

Figure 5.8 Inverse thickness, calculated from current transients, as a function of t/δ^2 corresponding to successive potential steps specified in the legend. The sample was heat treated at 450°C for 15 minutes. The slopes of the straight-line fits in $Å^{-1}$ and the time ranges of data used for the straight-line fits are included.

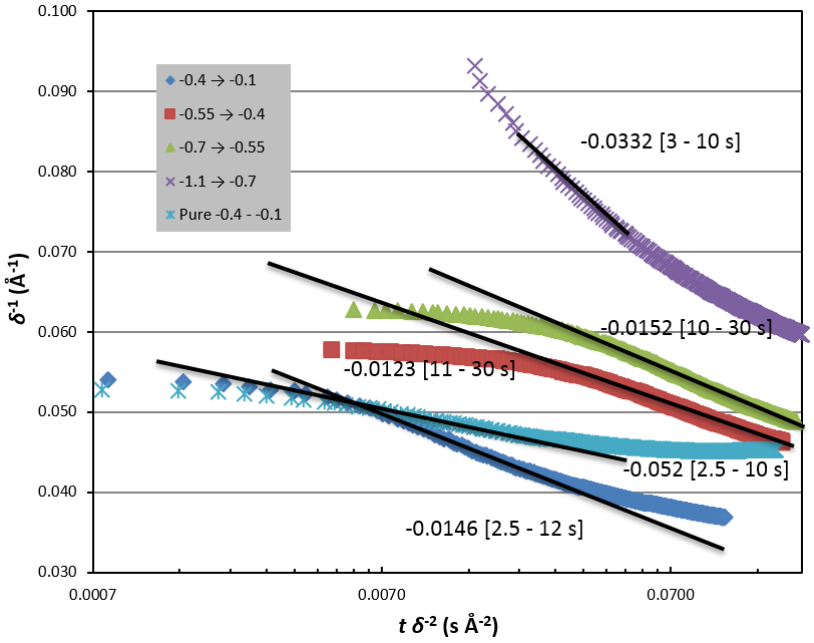

Figure 5.9 Inverse thickness, calculated from the current transients, as a function of t/δ^2 corresponding to successive potential steps specified in the legend. The sample was heat treated at 450°C for 40 minutes. The slopes of the straight-line fits in $Å^{-1}$ and the time ranges of data used for the straight-line fits are included.

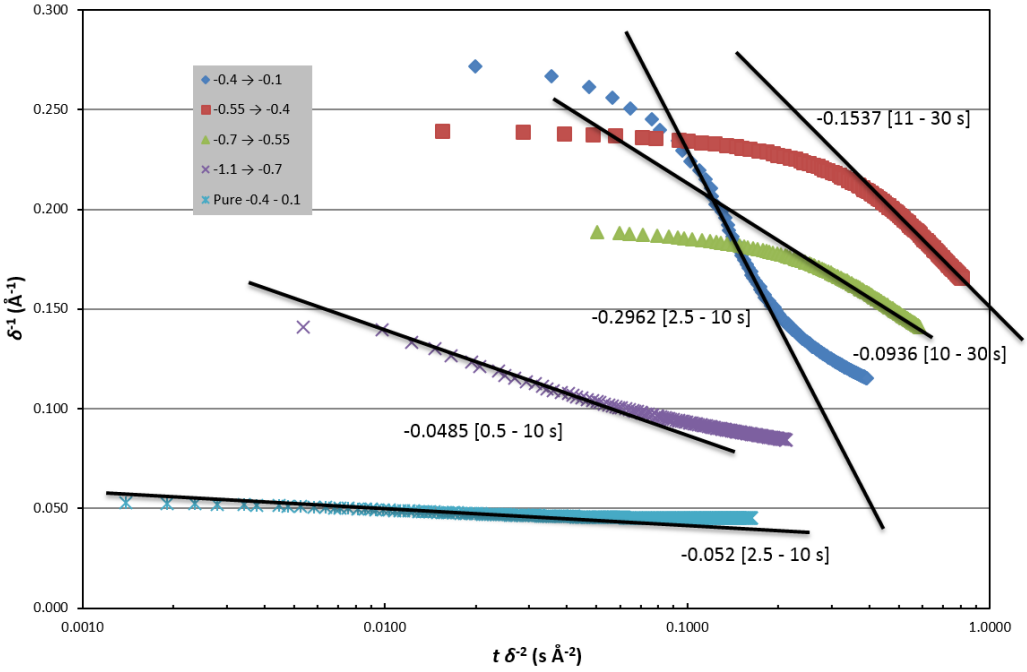

Figure 5.10 Inverse thickness, calculated from the current transients, as a function of t/δ^2 corresponding to successive potential steps specified in the legend. The sample was heat treated at 600°C for 60 minutes. The slopes of the straight-line fits (in $Å^{-1}$) and the time ranges of data used for the straight-line fits are included.

Table 5.1 shows the slopes obtained by analysis of the chronoamperometric data for all sample conditions and applied potential steps. Table 5.2 summarises the Cabrera-Mott parameters obtained by the slopes in Table 5.1. The parameters δ_1, u and W are defined and discussed in Chapter 4. The parameter δ_1 is consistent with the expected range of 100-1000 Å according to Cabrera-Mott [13]. Based on u in Table 5.2, the activation energy W for film growth was calculated from

$$u = u_0 \exp\left(-\frac{W}{kT}\right) = N\Omega\upsilon \exp\left(-\frac{W}{kT}\right) \quad \textbf{(5-2)}$$

derived from Eq. (2-12) and (2-13) in Chapter 2, by setting $u_0 = N\Omega\nu \approx 10^4$ cm/s valid at 22°C [13].

Table 5.1 Summary of slopes obtained by analysis of chronoamperometric growth data, by use of Cabrera-Mott inverse square logarithmic growth law.

		Potential Step (V)			
Heat treatment temperature (°C)	Heat treatment time (min)	-1.1 → -0.7	-0.7 → -0.55	-0.55→-0.4	-0.4 → -0.1
		Slope based on current transient ($Å^{-1}$)			
Pure Al		-0.0144	-0.003	-0.0034	-0.0052
300	30	-0.0167	-0.011	-0.0089	-0.01
300	60	-0.0285	-0.0127	-0.0103	-0.0113
450	15	-0.0268	-0.0151	-0.012	-0.0137
450	40	-0.0332	-0.0152	-0.0123	-0.0146
600	60	-0.0485	-0.0936	-0.1537	-0.2962

Table 5.2 Summary of results obtained by analysis of the chronoamperometric data by use of Cabrera-Mott inverse square logarithmic growth law, expressed in terms of the Cabrera-Mott parameters δ_1 , *u and W*.

		Potential Step (V)											
Heat treatment temperature (°C)	Heat treatment time (min)	-1.1 → -0.7			-0.7 → -0.55			-0.55 → -0.4			-0.4 → -0.1		
		δ_1 (Å)	u (Å/s)	W (eV)	δ_1 (Å)	u (Å/s)	W (eV)	δ_1 (Å)	u (Å/s)	W (eV)	δ_1 (Å)	u (Å/s)	W (eV)
Pure Al		160	1.34×10^{-9}	1.22	768	5.56×10^{-21}	1.89	677	4.34×10^{-17}	1.66	443	6.23×10^{-10}	1.24
300	30	139	2.51×10^{-5}	0.97	209	1.57×10^{-6}	1.04	259	3.30×10^{-7}	1.08	230	2.38×10^{-5}	0.97
300	60	81	1.14×10^{-3}	0.88	181	4.94×10^{-6}	1.01	224	1.25×10^{-6}	1.05	204	5.65×10^{-5}	0.95
450	15	86	1.03×10^{-3}	0.88	153	1.88×10^{-5}	0.98	192	4.38×10^{-6}	1.02	168	2.28×10^{-4}	0.92
450	40	63	2.00×10^{-3}	0.86	152	2.21×10^{-5}	0.98	187	5.43×10^{-6}	1.01	158	3.48×10^{-4}	0.91
600	60	47	3.13×10^{-3}	0.85	25	2.13×10^{-3}	0.86	15	6.91×10^{-3}	0.83	8	2.13×10^{-1}	0.74

The slopes given in Table 5.1 show clear differences between pure Al (least negative) and the AlPb alloys. The slope appears to increase in the negative direction with increasing annealing temperature and time of the AlPb alloys. A significant negative increase is observed for increase in the annealing temperature from 450°C to 600°C, although the O_2-free condition was used for the higher temperature (Section 5.2). The slope goes through a maximum value with increasing applied potential for the step from -0.55 to -0.4 V for the AlPb alloys annealed at 300°C and 450°C. These results affect the Cabrera-Mott parameters (Table 5.2) in the following way:

The δ_1 value, which is the inverse slope, is largest for pure Al. It is significantly smaller for the AlPb alloys, decreasing further with increasing heat treatment temperature and time. The u value, which is related to inverse exponential of the activation energy, W, and therefore can be considered as a rate constant, is smallest for pure Al, with the same exception as above. It is many orders of magnitude higher for the AlPb alloys, increasing with increasing heat treatment temperature and time.

The calculated activation energies are plotted in Fig. 5.11. The activation energy for film formation is largest for pure Al. It is about 50% smaller for the AlPb alloys, decreasing slightly with increasing heat treatment temperature and time. For pure Al, W shows a clear dependence on the applied potential, except for the potential step from -1.1 to -0.7 V. A similar, but reduced, dependence is evident for the AlPb alloy heat-treated at 600°C. The activation energy is similar for the alloys treated at 300 and 450°C. It does not show a strong dependence on the applied potential in this temperature range for heat treatment. The deviation of the -1.1 to -0.7 V step data from the potential dependency described above is not clear and will be discussed further in the Discussion section.

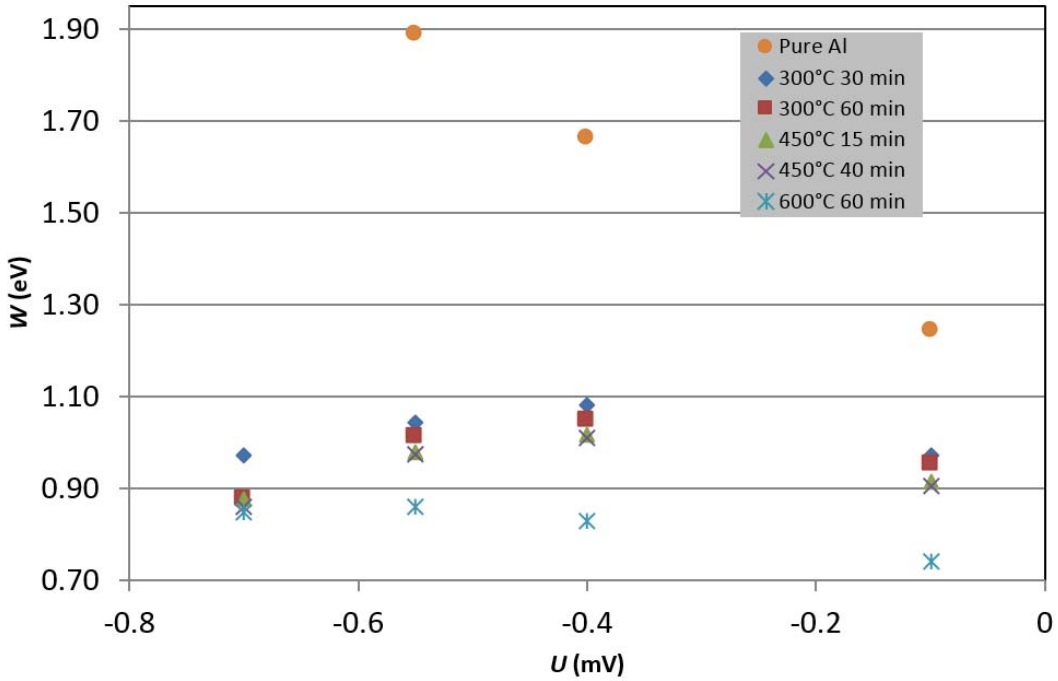

Figure 5.11 Activation energy as a function of applied potential for various heat treatment times and temperatures. Results for pure aluminium obtained by the same methodology in Chapter 4 are included for comparison.

5.3.2 Steady state results

A detailed coverage of the steady-state results, obtained between successive potential steps, are included since they appear to give valuable information about the effect of heat treatment temperature and time. In Fig. 5.12, the quasi-steady-state current densities, obtained one hour after the potential step, are plotted as a function of applied potential for various values of the heat treatment temperature and heat treatment time. These values are significantly larger for the AlPb alloy than for pure Al. The steady state current density of AlPb sample heat treated at 600°C is lower than those for the AlPb samples heat-treated at lower temperatures. The difference in the quasi-steady-state current densities of the samples treated at the lower temperatures (300-450°C) is not too significant. There is a small increase in the current density level with increasing heat-treatment temperature (and time) up to 450°C. A small increase in the current density is observed for each curve as a function of increasing potential. The curves, which show direct proportionality between the steady-state current density and potential, have nearly the same slope. The curve for 600°C deviates from this proportionality at the most negative potentials.

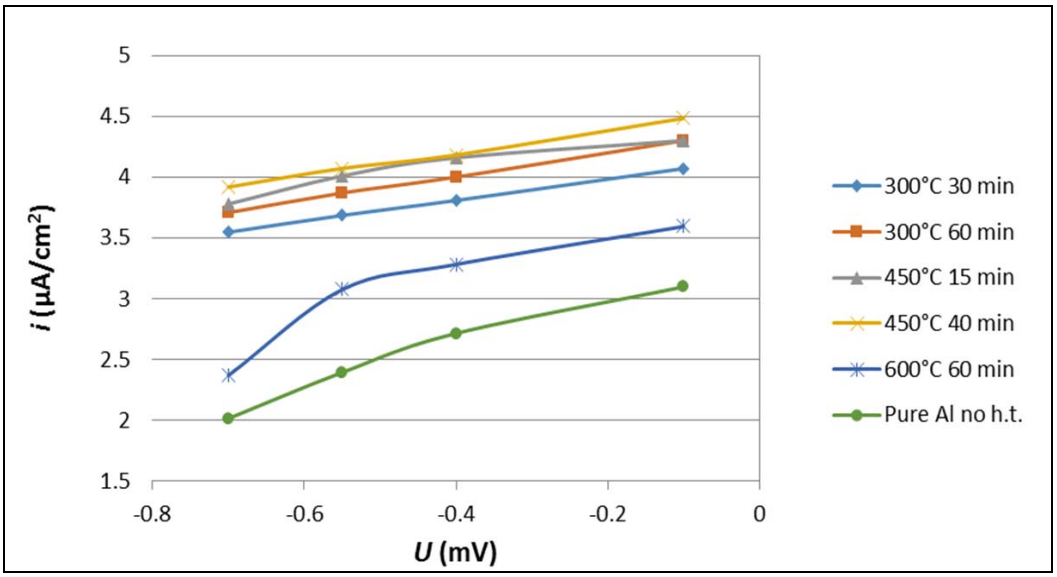

Figure 5.12 Quasi-steady-state current density vs. applied potential for AlPb20 samples heat treated at various temperatures for various periods. (pH 5.3 and acetic acid concentration 120 mM).

EIS results were analysed by assuming that the equivalent circuit model shown to apply to the oxide formed on pure aluminium in acetate buffer in Chapter 3, as reproduced in Fig. 5.13, is applicable. The thickness of the oxide layer is given by ([14,15])

$$\delta = \varepsilon_0 \varepsilon_b \frac{A}{C_b} \qquad \textbf{(5-3)}$$

where ε_0 is the dielectric constant in vacuum, ε_b is the dielectric constant of the barrier oxide layer, A is the surface area, and C_b is the capacitance of the oxide. For the barrier layer on aluminium, ε_b is about 10 [16,17].

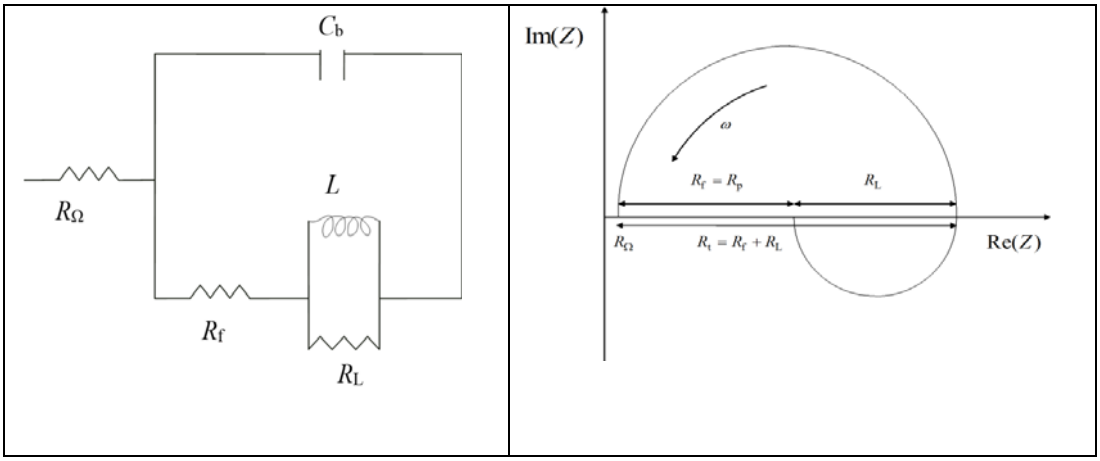

Figure 5.13 Equivalent circuit model for pure aluminium covered by its barrier oxide in aqueous solution and the corresponding Nyquist diagram, as presented in Chapter 3.

Fig. 5.14 shows Nyquist plots for AlPb for various heat treatment conditions. The result for as-received (not heat treated) pure aluminium obtained in the same solution (Chapter 3) is shown for comparison. The spectra, with the exception of the AlPb sample heat treated at 600°C, show nearly ideal semicircular plots, as required by the above model, while the plot for the 600° sample shows frequency dispersion [18], giving maximum impedance at a lower frequency than for the other samples. This indicates that the proposed model may not be valid for the AlPb sample heat treated at 600°C.

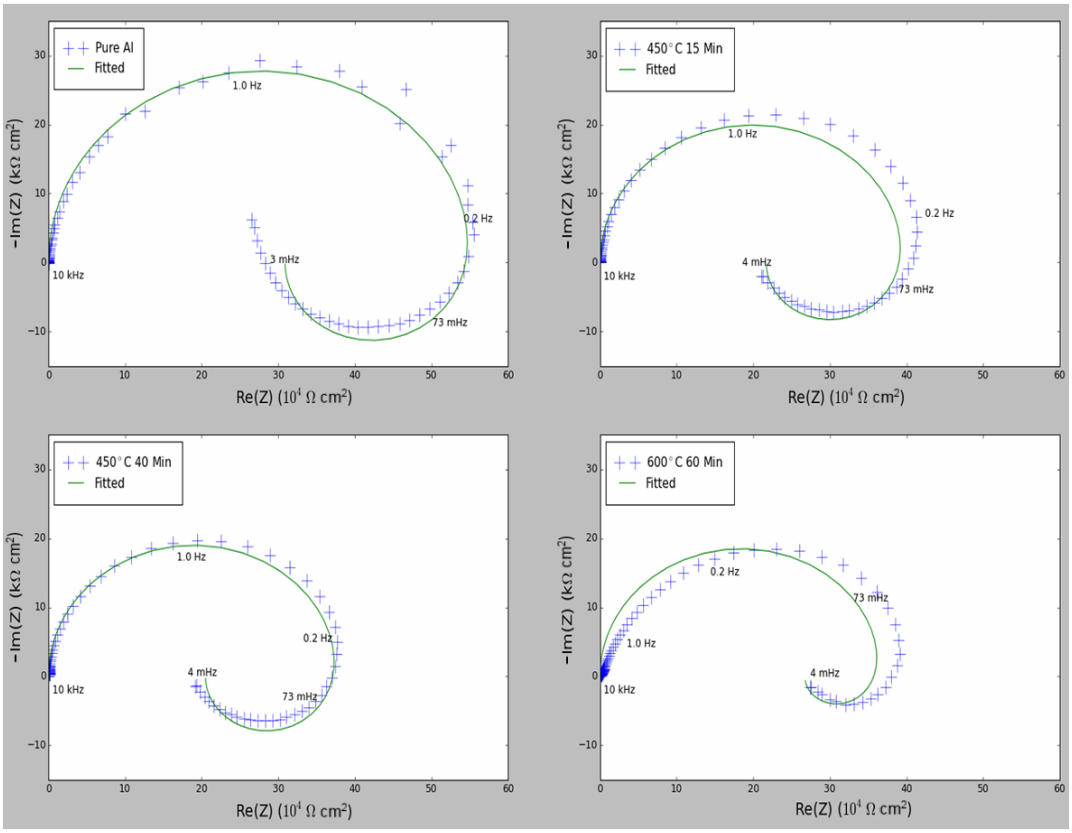

Figure 5.14 Measured EIS spectra (Nyquist plot) for various heat treatment conditions specified in the legend. Measurements were performed at an applied potential of -0.1 V.

Fig. 5.15 and 5.16 show the calculated film capacitance and barrier film thickness, respectively, as a function of applied potential and heat treatment conditions. In all cases, except for the AlPb alloy heat treated at 600°C, the capacitance decreases, and conversely, the film thickness increases with increasing applied potential. The data for AlPb sample annealed for 15 min at 300°C are quite similar to that of pure Al. The capacitance increases, and conversely the film thickness decreases with further increase in the heat treatment time and temperature. The curves in the two figures are nearly parallel to one another. The average slope of film thickness-potential plots (Fig. 5.16) is 1.16 nm/V, indicating that the data are related to barrier film growth. The samples annealed at 600°C show anomalous behaviour in relation to the foregoing generalized trends, and this will be discussed further in the Discussion section.

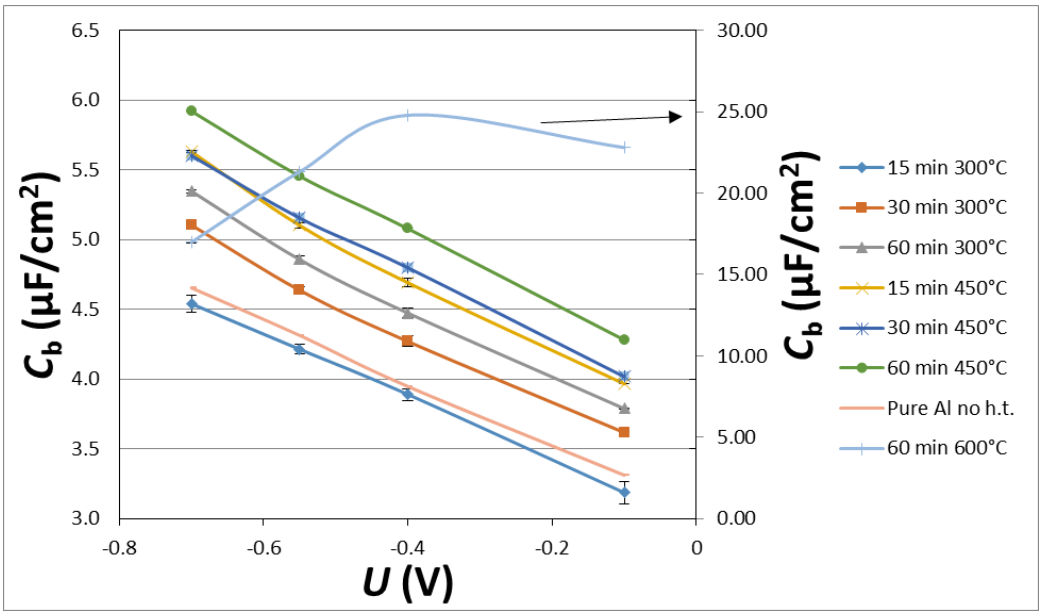

Figure 5.15 Calculated capacitance vs. applied potential for heat-treated aluminium samples containing 20 ppm Pb in 120 mM acetic acid concentration (pH 5.3). The capacitance scale for the sample heat-treated at 600°C for 60 minutes is shown on the right axis.

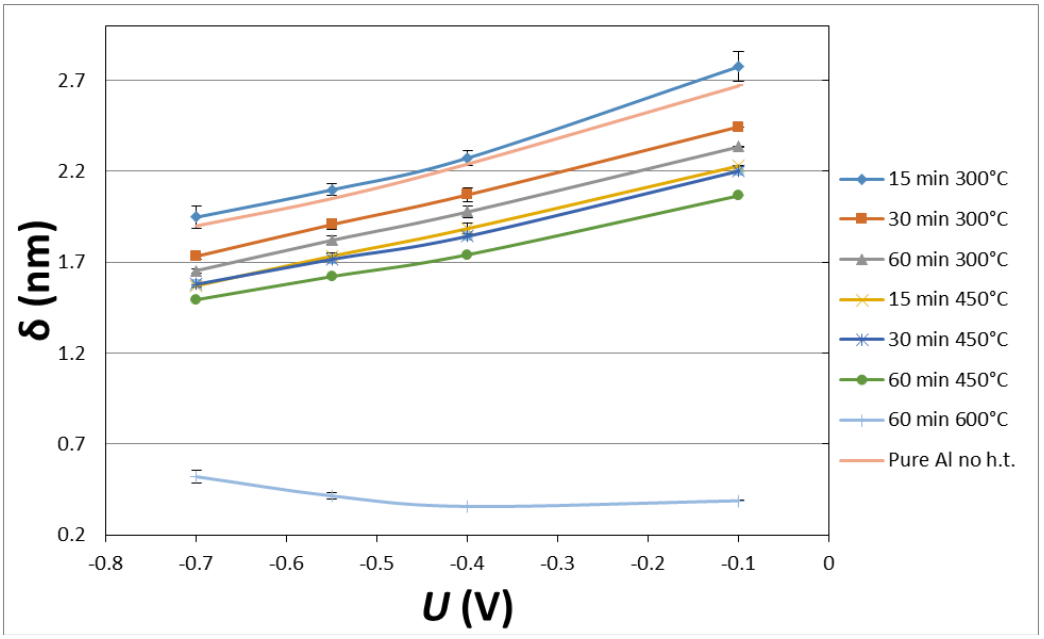

Figure 5.16 Calculated thickness vs. applied potential for heat-treated aluminium samples containing 20 ppm Pb in 120 mM acetic acid concentration (pH 5.3).

Fig. 5.17 shows the effect of applied potential and heat-treatment parameters on the film resistance R_f. This parameter is smaller for all AlPb20 specimens than that for pure Al. It decreases with increasing heat-treatment temperature and duration with the exception of the samples treated at 450 and 600°C. In the case of 450°C sample, increasing the heat-treatment time from 30 to 60 min seems to give a slight increase in R_f. With the exception of the 600°C sample, the effect of applied potential on R_f is very small. There is a tendency for a slight decrease to a minimum from -0.7 to -0.55 V, with a slight increase again with further increase in the potential, similar to the more appreciable similar changes for pure aluminium. The R_f for the 600°C sample is the smallest of all cases at -0.7 V. Despite larger scatter in the data for this case, R_f increases significantly with increase in the potential almost reaching the resistance of the untreated pure Al.

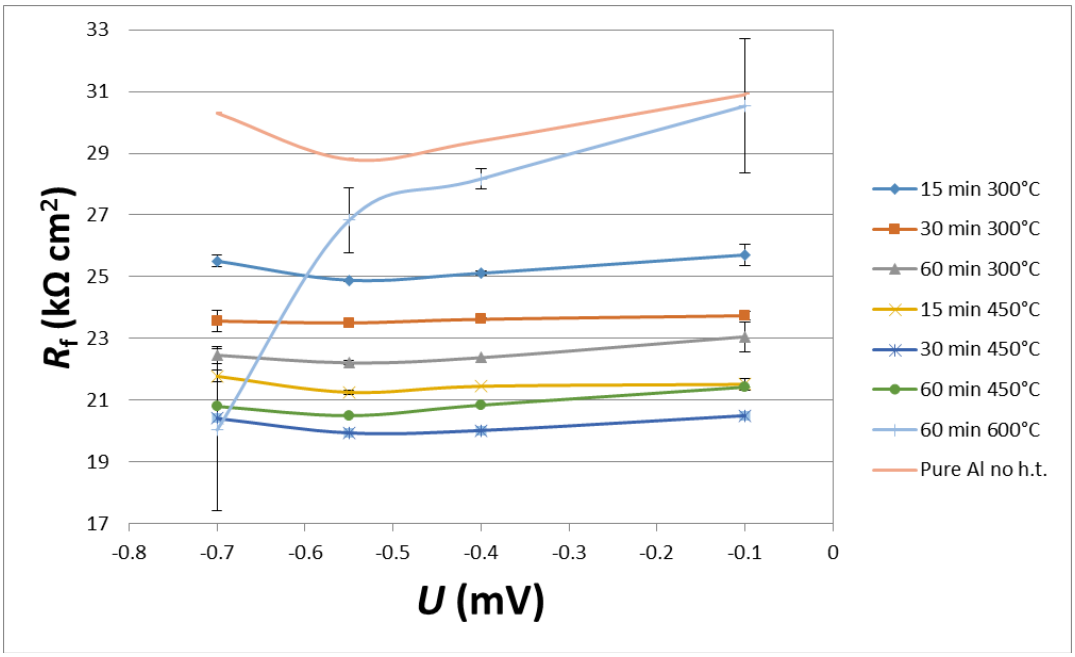

Figure 5.17 Oxide resistance vs. applied potential for heat-treated aluminium samples containing 20 ppm Pb. (pH 5.3 and acetic acid concentration 120 mM).

5.4 Discussion

It should be recalled from Section 5.2 that heat treatment of samples at 300 and 450°C was performed in air, while it was performed in oxygen-free environment at 600°C by use of a method, shown to be quite effective in filtering the trace oxygen from the pure argon gas atmosphere used during the heat treatment. Moderate growth of the oxide by heat treatment in air is expected in the temperature range 300-450°C, based on earlier work on impure Al containing Pb as a trace element [**7**,19]. In the absence of O_2 during heat treatment, such thickening of the film does not occur. Although the filtering method may not give a 100% O_2-free gas in the heat-treatment chamber, the purity from O_2 is significantly better than that obtained by use of pure Ar (99.999%), based on earlier experience [7]. Therefore, film thinning is likely related to film dissolution when the samples are immersed in the test solution after heat treatment during stabilisation of the surface at the initial potential before the start of the potential steps of the chronoamperometric measurement. The

decrease in the film thickness with increasing heat-treatment temperature and time goes in line with the corresponding increase in the leakage current and decreasing polarisation resistance.

The conclusions reached above based on the steady-state EIS data are considered reliable, although the lack of *in situ* ellipsometry data can be considered as a drawback against a definitive conclusion in this respect. The observed behaviour can be attributed to reduced passivity of the oxide with increasing heat treatment temperature and time in O_2-free environment. The reduced passivity can in turn be attributed to increasing contamination of the barrier oxide with segregating Pb, which is expected to increase with increasing heat-treatment parameters [1,2].

In addition to the foregoing, the transient results indicate a significant increase in the negative slope of the straight-line fits of data to Eq. (5-1) and a corresponding significant decrease in the Cabrera-Mott parameters δ_1 and W for the AlPb alloy relative to pure aluminium. These parameters further change more moderately, but in the same direction with increasing annealing temperature and time. W is about 50% smaller for the AlPb alloys, decreasing slightly with increasing heat treatment temperature and time. These results can be regarded as additional evidence to the conclusion that the passivity of the barrier film decreases as a result of increasing contamination with Pb with increasing heat-treatment temperature and time.

In addition to the applicability of the Cabrera-Mott kinetics, the potential dependence of the relative film thickness (1.2 nm/V) for given heat treatment conditions (except treatment at 600°C) is indicative of barrier oxide film growth as on pure aluminium, independent of Pb segregation. This is attributed to the fact that Pb segregation is essentially related to the heat-treatment, not on metal oxidation and thickness changes as a result of the potential applied in the specified range in the test solution after heat treatment. In other words, the level of Pb contamination affects the absolute thickness relative to that of pure Al. However, the relative thickness change, with respect to the applied potential, remains at the same value (1.2 nm/V) as that for pure Al. This may be related to the likelihood that the oxide formed is still pure Al oxide with the same composition and structure as on pure Al at molecular scale, while the apparent conductivity of the contaminated oxide is reduced. This is possible if the segregated Pb is in particulate form, not chemically interacting with the Al oxide. The cause of this observation is not well understood.

Segregated Pb was not visible by SEM or TEM for samples annealed at temperatures smaller than 600°C in earlier work. However, it was detectable by GD-OES depth profiling and potentiodynamic polarization in chloride solution in the temperature range above 300°C [5,19]. Pb particles as large as 100 nm in diameter, which segregated to the oxide surface during heat treatment at 600°C, became readily observable by SEM and TEM. TEM investigation of samples heat treated in air at 600°C also revealed formation of a nearly continuous Pb-rich film of a few nanometer thickness between the metal surface and the γ-Al_2O_3 crystals growing into the metal from the surface. In O_2-free environment, Pb segregation in the form of particles, migrating through the unaffected air-formed oxide film to the surface, was also readily visible via SEM analysis of AlPb samples annealed at 600°C. The film thickness kinetics measurements, which depend on calibration of the chronoamperometric data with the steady-state capacitance measurements by EIS, may be in error if a significant change occurs in the dielectric constant ε_b as a result of contamination by segregating Pb.

The activation energy for film growth, W, in the original Cabrera-Mott formulation, does not include the effect of an applied potential, as it should in the present case for film growth in an aqueous solution. Despite this important difference in relation to the classical derivation, the present results, especially for pure Al (Chapter 4), show high-field assisted barrier-film growth in aqueous solution. The same conclusion is also applicable to Mg, as shown earlier by Nordlien [20] (in Chapter 5). For these cases, the effect of applied potential is expected to be incorporated into the

activation energy. Thus, W shows clear dependence on applied potential (Fig. 5.11 and Chapter 4). It decreases with increasing potential for pure Al, indicating reduced energy needed (or increasing energetically favourable conditions) for the growth of the barrier layer (anodizing) with increasing applied potential, as expected. For the AlPb alloys, however, the effect of applied potential on W is of reduced significance relative to pure aluminium. The film resistance R_f is analogously independent of applied potential for AlPb alloys (with the exception of 600°C-annealed sample) relative to pure Al (Fig. 5.17). These results can be due to an effect, which counteracts the expected decrease of W, and analogously expected increase of R_f with increasing potential for the AlPb alloys. The cause of the observed effect is unclear, other than the likelihood that it is related to Pb segregation. Increasing segregation of Pb into the film and/or at the metal-film interface is expected to cause such an effect.

The chronoamperometric data for the potential step -1.1 to -0.7 V do not quite follow the foregoing discussion about the effect of applied potential. It is questionable whether the Cabrera-Mott law is applicable for the measured current transients for this potential step. A possible cause is hydrogen evolution, probably localised to the Pb segregations, which will affect the current transient, although the actual film growth may satisfy the Cabrera-Mott law, as was shown to be the case for pure Al in Chapter 4. Another possibility is the oxidation of the Pb particles in this potential range to form soluble Pb^{2+} or a Pb-oxide [21]. The oxide may moreover exhibit considerably lower electrical conductivity than metallic Pb [22]. Thus, the effect of secondary reactions and/or change in the electrokinetic properties of the Pb segregations could contribute to the observed anomaly.

The anomalous behaviour of the 600°C-annealed AlPb sample in relation to the other alloys discussed above needs separate evaluation. It is again based on the possible effects of Pb segregation along with film thickening and crystallization, which occur only locally [5]. Film thickening and local crystallization may cause reduced leakage current relative to the AlPb samples annealed at lower temperatures. This is still higher than the leakage current for pure aluminium, which is not heat treated, but is under otherwise identical conditions (Fig. 5.12). The observed effect may be attributed partly to Pb segregation.

Many of the segregated particles on samples annealed at 600°C under O_2-free conditions are large enough to grow through the oxide on top of the oxide film during heat treatment, while they are still in metallic contact with the aluminium alloy substrate [7]. These nearly spherical Pb-metal sites, although contributing to a small increase in the surface area, are still expected to cause detectable increase in the measured capacitance. Their capacitance (per area) is significantly higher than the film capacitance. In addition, nonuniformity of charge distribution at the surface caused by the metallic Pb particles exposed on a surface covered by a relatively insulating oxide will contribute to the frequency dispersion of the measured impedance. These factors are expected to give significantly increased values to the measured (effective) capacitance and resistance of the electrochemical impedance in relation to the true values. As a result, the results reported for the samples annealed at 600°C can become erroneous.

Kramers-Kroenig transform analysis (not shown) indicate reasonable consistency of the EIS data within the frequencies of interest for the calculation of the capacitance and film resistance with the possible exception of samples heat-treated at 600°C. Time dependent phenomena during impedance measurement may thus be indicated in addition to nonuniformity of charge distribution.

Change of the electrochemical properties of this alloy with increasing potential in the results shown in Fig. 5.15 and 5.17 can also be interpreted as changes occurring with increasing time of immersion in the test solution. Moreover, passivation of the exposed Pb particles above the reversible potential of Pb oxidation is possibly reflected in the increase exhibited by R_f with

increasing potential, approaching the R_f value of pure alloy asymptotically with increasing applied potential (Fig. 5.17). Meanwhile, the measured capacitance (Fig. 5.15) and calculated film thickness (Fig. 5.16) remain relatively unaffected above -0.4 V, as would be expected, in agreement with the hypothesis of Pb passivation.

The inability to use the ellipsometry analysis simultaneously with the chronoamperometric measurements was an important drawback of the present study because a simultaneous, direct *in situ* measurement of the film thickness would eliminate some of the uncertainties in the interpretation of some of the results, as discussed above. The mechanisms, which affect the reported changes in the electrochemical properties of the surface, could not be fully clarified. In particular, it is not possible to identify the exact causes of the observed property changes, whether these can be attributed to the barrier film properties *per se* or modifications occurring at the metal-film interface, such as segregation of a Pb film by heat treatment and chronoamperometric polarization. In Chapter 4 the time intervals used for fitting the chronoamperometric data on pure Al to Cabrera-Mott is based on evaluation of the ellipsometry data. In this chapter, we lacked this possibility. The results show, however, significant differences in the electrochemical properties of pure Al, AlPb alloy heat-treated at temperatures below 600°C, and the properties of alloy treated at 600°C. While the formation kinetics of the barrier oxide on pure aluminium in the aqueous buffer solution appears convincingly to be governed by the Cabrera-Mott high field growth mechanism, analysis of the data for the AlPb alloy appears to become increasingly difficult with increasing Pb segregation to the metal surface, into the barrier film and to the film surface, especially in the case of samples annealed at 600°C. In this case, the nature of Pb segregation was documented by SEM in earlier work. For specimens annealed in air, the available GD-OES and potential-controlled electrochemical data suggest segregation at the metal-oxide interface [5,19]. The present results complement the earlier evidence of Pb segregation at the surface (in the film and/or film-metal interface), which can be summarized as a slight deterioration of the passivity in general for the samples annealed at temperatures smaller than 600°C, relative to that for pure aluminium.

5.5 Conclusions

- Analysis of chronoamperometric data by using the Cabrera-Mott inverse-logarithmic growth law indicates faster growth of the Pb-contaminated barrier layer on aluminium in relation to that on pure aluminium. However, the passivating properties of the Pb-contaminated oxide are poorer than the oxide grown on pure Al. These two results are not contradictory to one another in view of a higher dissolution rate expected on the poorer oxide.
- Increasing Pb contamination of the barrier-layer, as a result of heat treatment, causes reduction of oxide thickness in the test solution in relation to the film thickness on pure Al and commensurate with increasing heat-treatment temperature (below 600°C) and time.
- Pb segregation, with the exception of significant particulate segregation by annealing at 600°C, did not affect the expected 1.2 nm/V thickness-potential relationship of the barrier oxide on aluminium.
- Deterioration of passivity relative to pure Al, by Pb segregation for AlPb samples annealed at temperatures as low as 300°C is in agreement with earlier electrochemical polarization data. These results are in agreement also by earlier GD-OES depth profile data, showing Pb segregation at the oxide- metal interface at such low annealing temperature.
- Reduced deterioration of passivity for the sample heat treated at 600°C in O_2-free atmosphere, despite significant Pb segregation, especially at potentials exceeding the thermodynamic reduction potential of metallic Pb, is attributed to oxidation of Pb.
- The use of indirect chronoamperometric data alone for estimation of film growth rate, due to difficulty in obtaining reliable, simultaneous ellipsometric data in the present study, was a

significant drawback in situations where film growth was affected by complicating factors, such as contamination of oxide film and film-metal interface by Pb and resulting nonuniformity of current distribution, as in the case of samples annealed at 600°C. This factor affected also the reliability of the "steady-state" EIS data, necessary for the calibration of the chronoamperometric data.

5.6 References

[1] Gundersen, J. T. B., Aytac, A., Nordlien, J. H., and Nisancioglu, K. *Corros. Sci* **46**, 697 (2004).

[2] Gabrisch, H., Dahmen, U., and Johnson, E. *Microsc. Microanal.* **4**, 286 (1998).

[3] Anawati, Graver, B., Nordmark, H., Zhao, Z., Frankel, G., Walmsley, J., and Nisancioglu, K. *J. Electrochem. Soc.* **157**, C313-C320 (2010).

[4] Shimizu, K., Furneaux, R. C., Thompson, G. E., Wood, G. C., Gotoh, A., and Kobayashi, K. *Oxid. Met.* **35**, 427 (1991).

[5] Sævik, Ø., Yu, Y., Nordlien, J., and Nisancioglu, K. *J. Electrochem. Soc.* **152**, B334-B341 (2005).

[6] Sævik, Ø., Yu, Y., Nordlien, J., and Nisancioglu, K. *J. Electrochem. Soc.* **152**, B327-B333 (2005).

[7] Sævik, Ø. *Effect of Trace Element Lead on the Electrochemistry and Corrosion of Aluminium Alloys*. PhD thesis, Norwegian University of Science and Technology, Trondheim, Norway (2005).

[8] Walmsley, J. C., Sævik, Ø., Graver, B., Mathiesen, R. H., and Nisancioglu, K. *J. Electrochem. Soc.* **154**, C28-C35 (2007).

[9] Flamini, D. O., Saidman, S. B., and Bessone, J. B. *Corros. Sci* **48**, 1413 (2006).

[10] Carroll, W. and Breslin, C. *Corros. Sci.* **33**, 1161-1177 (1992).

[11] Graver, B., v. Helvoort, A., and Nisancioglu, K. *Corros. Sci.* **52**, 3774-3781 (2010).

[12] Masaki, T., editor. *Binary Alloy Phase Diagrams*. ASM International, Materials Park, Oh, USA (1990).

[13] Cabrera, N. and Mott, N. F. *Rep. Prog. Phys.* **12**, 163 (1948-1949).

[14] Vetter, K. J. *Electrochim. Acta* **16**, 1923 (1971).

[15] Bessone, J., Mayer, C., Jüttner, K., and Lorenz, W. J. *Electrochim. Acta* **28**, 171-175 (1983).

[16] de Wit, J. and Lenderink, H. *Electrochim. Acta* **41**, 1111-1119 (1996).

[17] Young, L. *Anodic Oxide Films*. Academic Press, New York, USA (1961).

[18] Jorcin, J.-B., Orazem, M. E., Pébère, N., and Tribollet, B. *Electrochim. Acta* **51**, 1473-1479 (2006).

[19] Senel, E. *Anodic Activation of Aluminium by Trace Element Gallium*. PhD thesis, Norwegian University of Science and Technology, Trondheim, Norway (2013).

[20] Nordlien, J. H. *Naturally formed oxide film on magnesium and magnesium alloys*. PhD thesis, Norwegian Institute of technology, Trondheim, Norway (1995).

[21] Wikipedia. http://en.wikipedia.org/wiki/Standard_electrode_potential_(data_page).

[22] Darwish, A., El-Zaidia, E., El-Naass, M., Hanafy, T., and Al-Zubaidi, A. *J. Alloys Compd.* **589**, 393 (2014).

6 Discussion

This chapter is intended to take an overall look at the results obtained in chapters 3 to 5 and discuss the general significance of these with respect to the original objectives, in contributing to development of methodology to study oxide growth and dissolution on pure aluminium, understanding the mechanism of these processes, including the electrochemical properties of the formed oxide, and how the presence of trace element Pb influences the viability of the methodology developed for pure aluminium.

6.1 Oxide growth kinetics for pure Al

In Chapter 4 we showed that the growth of barrier oxide on Al in aqueous solution is governed by the Cabrera-Mott law, as expressed by Eq. (4-1). This result thus verifies the earlier literature [1] that, the law originally developed for oxide growth on metals in oxygen containing gaseous environments, is also applicable to barrier oxide growth in aqueous solution. In earlier work, the law has been shown to apply for barrier oxide growth under anodizing conditions, involving application of a significant anodic potential by an external source, in which the high field required for oxide growth is provided by the applied potential. The present work shows the applicability of the growth law also for small applied potentials giving growth of oxide films as thin as a few monolayers. The required high field for maintaining films of such thickness is expected to exist at such low potentials due to the small thickness of the film. The steady-state thickness can accurately be controlled by the applied potential at 1.2 nm/V, a value that was established earlier in anodization studies, relying mostly on *ex situ* thickness measurements [2-4]. Earlier *ex situ* data was not able to verify this correlation for thin films because of significant changes presumed to occur during exposure to ambient environment, as reviewed in Chapter 2. The present growth data did not obey the Cabrera-Mott kinetics satisfactorily for very negative potentials, such as -1.1 $V_{Hg_2SO_4}$, probably because of onset of secondary processes, such as H^+ reduction.

In view of the foregoing and the original objectives of the present work, the study of oxide growth kinetics was limited to the validation of the Cabrera-Mott law for pure Al in acetate buffer, and the study of hydrated layer was limited to that reported in Chapter 3. The Cabrera-Mott parameters δ_1, u and W, could readily be obtained [1]. However, a detailed analysis of the significance of these parameters under a wider matrix of experimental conditions had to be left outside the scope of the present work. The variation of these parameters, especially the activation energy W, appeared to be of the correct order of magnitude and vary in an intuitively acceptable manner by variation of an experimental parameter, such as the applied potential.

6.2 Oxide dissolution kinetics for pure Al

Chronoamperometric measurements during film dissolution were shown to be a non-faradaic process. Therefore, the current transients in response to negative potential steps could not be used. However, the ellipsometric measurements gave reliable *in situ* data, showing unambiguously that film dissolution is mass transfer controlled, in agreement with earlier suggestions to that effect [5]. The dissolution data could satisfactorily be correlated with respect to Fick's 2nd law, assuming constant oxide solubility during the dissolution process. The results suggested that the oxide solubility was determined by the applied potential, which would suggest existence of equilibrium condition at the barrier surface. However, this could not be verified with

respect to the conventional Pourbaix diagram for aluminium [6]. The conventional data do not include all the relevant reactions possible to occur under the given conditions for the present study, such as hydride formation.

It is also possible that migration plays a role in addition to diffusion. As Al^{3+} is produced at the barrier surface, acetate ions have to migrate to the surface to maintain local electroneutrality. It can be shown that Fick's law would still apply in such a situation, but the effective diffusion coefficient, would be larger than that expected for pure diffusion [7].

In any event, the results suggest that the applied potential fixes the solubility of the oxide, which, together with the diffusion coefficient of the dissolving species, probably Al^{3+} under the present conditions, and the hydrodynamic conditions in the solution adjacent to the barrier layer, in turn determine the dissolution rate. Since mass transfer occurs through the porous hydrated layer, the hydrodynamic condition is probably nearly stagnant. Knowledge of one of the governing parameters, the diffusion coefficient or solubility of Al^{3+} would then allow the determination of the other.

6.3 Methodology

The present work for pure Al showed that the simultaneous use of VISSE and chronoamperometry, with the use of EIS for absolute thickness calibration under steady-state conditions for the barrier oxide, was a successful combination of methods for tracking of thin film growth. Since VISSE and chronoamperometry are supposed to give the same growth rate in principle, the use of both methods simultaneously provided an effective control of the reliability of the measured data. In this manner, the drawbacks of the methodology were identified, such as the slowness of the multi-wavelength ellipsometric technique relative to the fast rate of barrier-layer growth. This was not a problem with chronoamperometry with fast current measurement, which can be performed effectively by an oscilloscope, if necessary. For tracking film dissolution, chronoamperometry proved to be impossible because of the chemical (as opposed to electrochemical) nature of the process. However, ellipsometry proved to be effective and reliable method in this case because the mass transfer controlled dissolution occurred at a significantly slower rate than growth. In this respect, the two methods were quite supplementary in producing the desired data.

A possible way of speeding up ellipsometric data acquisition is to restrict the measurements to a single wavelength. In this way, the analysis will be simplified to the determination of only one unknown. This will restrict the measurement to tracking of single layer growth. The approach would have been possible with the present set-up, assuming that the physical properties, especially the thickness of the hydrated layer did not change during the growth of the barrier layer. However, the approach becomes dependent on the EIS calibration at the end of each potential step, as was practised in the present work. Such calibration for each potential step by itself can be considered as a drawback. It is in turn based on the assumption that the physical properties of the barrier film, especially the dielectric constant, do not change during measurement. Such a restriction would not be necessary with the multi-wavelength approach, which would allow tracking of variation in the physical properties. However, as discussed in more detail in Chapter 3 and Ref. [8] this is not always possible, especially if the dielectric properties of the barrier and hydrated cannot be distinguished from one another. In any event, the foregoing assumptions appeared to be satisfied for barrier-film growth and dissolution for pure aluminium, and the use of a single wavelength approach would have been a better choice to obtain the higher tracking speed needed.

The present work showed the necessity of *in situ* measurement in tracking the growth and dissolution of thin barrier films. The use of *ex situ* TEM analysis to determine the barrier layer

thickness as a function of applied potential gave erroneous results in Chapter 3, probably because of interaction of the surface with ambient air in transferring the specimen from the solution to a TEM for thickness measurement. The high vacuum in the specimen chamber for TEM may also have contributed to changes in the thickness of the barrier layer.

In the presence of a second component and phase in aluminium, as demonstrated by heat treatment in the presence of Pb as a trace element, new challenges arise in acquisition and interpretation of both ellipsometric and electrochemical data. First of all, the specularity of the surface was reduced, hindering the use of ellipsometry, which requires a specular surface to obtain reflected signal with sufficient intensity from the sample. The causes of this observation are not clear beyond the discussion given in Chapter 5. This drawback alone may put a significant restriction to the applicability of the present approach to idealised systems by disqualifying the use of ellipsometry, which is the only direct *in situ* method in the proposed methodology. The applicability of the method without the use of ellipsometry, *i.e.*, by use of the electrochemical methods chronoamperometry and EIS, cannot be regarded as a direct *in situ* method. However, the approach is quite sensitive as long as the underlying assumptions are obeyed. The present work showed the approach to be at least as reliable as the direct ellipsometry in determining film growth on pure aluminium.

The presence of trace element Pb, which segregated as a second metallic phase at the surface by heat treatment, caused additional challenges in the interpretation of the electrochemical EIS approach, as applied here in the calibration of the steady-state film thickness. This was explained in Chapter 5 in terms of possible changes in the physical and electrochemical properties of the oxide, such as dielectric constant and conductivity as a function of temperature and time of heat treatment. However, these properties did not appear to change significantly as a function of applied potential for a given thermal condition, and the film thickness maintained its direct proportionality to the applied potential at about 1.2 nm/V, except for samples heat treated at the highest temperature (600°C) used. The validity of the method in determining the absolute thickness could be questioned related to local changes occurring in the oxide properties during heat treatment because of locally segregating Pb-rich particles. This violates the assumption in the EIS model about the spatial uniformity of the properties of the electrochemical interface. However, these effects were argued to be small in view of the reasonable results obtained as a function of heat treatment conditions. These indicated in summary that increasing heat treatment temperature and time prior to the chronoamperometric measurements in the test solution resulted in decreasing film thickness at a given potential in the test solution. This was related to the simultaneous decrease in the polarization resistance and increasing leakage current, all indicating reduced passivity as a result of increased segregation of Pb in the film and film-metal interface.

A possible improvement of the EIS calibration is to develop the equivalent circuit model to incorporate variable properties, depending on the size and location of the Pb-rich segregations. This can be determined by *ex situ* microscopy before immersion of samples in the test solution. Using a rigorous approach as Armstrong-Edmonton, the model can be modified to incorporate local nonuniformities in the electrochemical behaviour. However, the surface properties of the segregations can become modified, *e.g.*, by oxidation, during measurement. A more empirical approach by use of the constant phase element approach can be tried [9]. This type of development was outside the scope of this work. However, determination of the absolute average thickness by a non-electrochemical method, such as ellipsometry, would have been very useful. Multi-wavelength ellipsometry would possibly also be able to track changes occurring in the dielectric constant of the barrier oxide, if any, as indicated in Chapter 3. It is not possible to discuss further how important and tractable these modifications would be based on the available and obtainable results.

6.4 Suggestions for further work

The main weakness with the ellipsometry measurement was the low measurement frequency. A higher measurement frequency is expected to result in better correlation to chronoamperometry measurement and more accurate Cabrera-Mott analysis. Due to the difficulties in measuring more than one film and the expected large difference in growth speed between the barrier and hydrated oxide layer it is considered likely that the use of a faster single wavelength ellipsometer can bring results with the needed accuracy at higher measurement frequency. The study should include a more comprehensive analysis of the extent to which ellipsometry is applicable to surfaces with reduced specularity.

However, it may be worth to follow up the original idea of multi-wavelength ellipsometry to the dissolution of the composite barrier and hydrated oxide. Firstly, the applicability of the available optical models in distinguishing the between the properties of the layers, including the changes that may occur during film thinning, is worth investigating. It is not immediately clear how the ellipsometry data obtained under such conditions could be validated by another independent *in situ* method. *In situ* TEM, which is under development at present [10], appears promising. However, it may not be possible to work with cross-sectional samples needed for this purpose.

Improvement of the EIS model for steady-state thickness calibration would be more feasible, in view of the apparent validity of the 1.2 nm/V proportionality for film thickness in solution, also for impure Al. However, the absolute thickness value has to be determined in the beginning of a chronoamperometric film-growth run if ellipsometry is not applicable for this purpose. *Ex situ* determination at the outset is not applicable as discussed above. The as heat-treated properties of the film are expected to change after the sample is immersed in the test solution and stabilized at the potential applied initially. Deviation of the ideal impedance behaviour of the electrical impedance can be treated semi-empirically by use of the constant-phase element concept discussed in Chapter 5. Frequency dispersion of the measured impedance can also be handled by improving the mathematical models available by incorporating the geometrical size and distribution of conducting metallic and intermetallic particles segregating into the oxide by heat treatment.

The pure aluminium samples studied were in the as-received (cast and rolled) condition. A study of the effect of heat treatment on the optical and electrochemical properties is unfortunately lacking in this work. It is needed as reference to the study in Chapter 5 of the effect of heat treatment on the oxide properties of the AlPb alloy. Heat treatment in the absence of oxygen is not expected to give an increase in the barrier-layer thickness, unless trace O_2 was present. Thickness increase or decrease due to reduced hydration, change in microstructure, reduction of the oxide can be presumed to occur, and these should be quantified before samples are immersed in the test solution. It is of interest also to investigate the modifications which would be expected to occur to such surfaces during exposure to the test solution under controlled (constant pH and applied potential) conditions. The results would clarify questions raised, amongst others, the thickness changes reported for the AlPb alloys in solution, to what extent these could be attributed to heat treatment prior to immersion and modifications in solution due to segregated Pb.

The results suggest the possibility of fundamental studies of barrier oxide dissolution, which is mass transfer controlled, determined by Fick's 2^{nd} law. Since the calculated film solubility does not agree with the conventional Pourbaix diagram, it is determined either by a nonequlibrium process, involving migration and local pH change, or the effect of hydride formation that has to be taken into consideration [11]. The methodology can thus be used to investigate the importance of these processes in oxide dissolution for a better understanding of this little investigated process

6.5 References

[1] Cabrera, N. and Mott, N. F. *Rep. Prog. Phys.* **12**, 163 (1948-1949).

[2] Thompson, G. E. *Thin Solid Films* **297**, 192 (1997).

[3] Hass, G. *J. Opt. Soc. Amer.* **39**, 532 (1949).

[4] Deryagin, B. V. and Friedland, R. M. *Z. tech. Phys. U.S.S.R* **18**, 1443 (1948).

[5] Nisancioglu, K., Davanger, K. Y., and Strandmyr, Ø. *J. Electrochem. Soc. 1981 volume 128, issue 7, 1523-1526* **128**, 1523-1526 (1981).

[6] Pourbaix, M. *Atlas of Electrochemical Equilibria in Aqueous Solutions*. National Association of Corrosion Engineers, Houston, USA (1974).

[7] Newman, J. and Thomas-Alyea, K. E. *Electrochemical Systems 3rd ed.* Wiley-Interscience, New York, USA (2004).

[8] Gils, S. V., Melendres, C., Terryn, H., and Stijns, E. *Thin Solid Films* **455-456**, 742-746 (2004).

[9] Orazem, M. and Tribollet, B. *Electrochemical Impedance Spectroscopy*. John Wiley & Sons, New York, USA (2008).

[10] Malladi, S. R. K., Xu, Q., Tichelaar, F. D., Zandbergen, H. W., Hannour, F., Mol, J. M. C., and Terryn, H. *Surf. Interface Anal.* **45**, 1619 (2013).

[11] Perrault, G. G. *J. Electrochem. Soc.* **126**, 199-204 (1979).

7 Conclusions

- Growth of barrier oxide on pure aluminium in aqueous solution is verified unambiguously to be consistent with Cabrera-Mott law of growth kinetics by use of chronoamperometry and ellipsometry.
- Analysis of dissolution rate by ellipsometry verified mass-transfer controlled barrier oxide dissolution on pure Al according to Fick's second law, suggesting that the rate of barrier film dissolution is largely a chemical process. Applied potential determines the oxide solubility.
- *Ex situ* methods for determination of the thickness of the barrier layer, such as TEM analysis of film cross sections, give erroneous results during growth of thin films, for which an *in situ* approach is necessary because exposure of samples to ambient air in transfer affects film thickness. *Ex situ* methods may be applicable for determining the thickness of thick anodized films, which are more stable in transfer.
- Simultaneous use of ellipsometry and chronoamperometry for oxide growth, combined with electrochemical impedance spectroscopy (EIS) for steady-state thickness calibration is a viable method for *in situ* analysis of barrier oxide growth kinetics. These methods are complementary to one another, and their simultaneous use increases the reliability of results.
- Fast tracking of thickness is necessary for evaluation of barrier oxide growth kinetics, suitable for single wavelength ellipsometry and chronoamperometry. Multi-wavelength ellipsometry is too slow to track fast barrier oxide growth.
- Multi-wavelength ellipsometry is suitable for tracking oxide dissolution, as the dissolution rate is considerably slower than oxide growth. Use of chronoamperometry is not suitable for oxide dissolution as it is a non-electrochemical process.
- Segregation of trace element Pb to the oxide-metal interface and into the oxide film by heat treatment reduces the passive properties of the barrier layer, quantified in terms of increased capacitance, reduced film thickness, reduced polarisation resistance and increased leakage (passive) current.
- Ellipsometry fails for heat-treated non-ideal aluminium surface contaminated with segregated trace-element Pb particles because the surface loses specularity for applicability of ellipsometry. Thickness tracking by chronoamperometry is still possible during growth. The Armstrong-Edmonson model used for thickness calibration by EIS may have to be improved for cases where segregation of Pb may violate the assumption of uniform accessibility of the surface.